

CALIFORNIA STATE UNIVERSITY, NORTHRIDGE

EBSD AND MICROSTRUCTURAL ANALYSIS OF QUARTZ-FELDSPATHIC  
ROCKS FROM THE SOUTH MOUNTAINS, ARIZONA: AN EVALUATION OF  
FLOW LAWS AND CRUSTAL RHEOLOGY

A thesis submitted in partial fulfillment of the requirements

For the degree of Master of Science in Geology

By

David Charles Annis

May 2012

The thesis of David Charles Annis is approved:

---

J. Douglas Yule, Ph.D.

---

Date

---

Richard Heermance, Ph.D.

---

Date

---

Elena A. Miranda, Ph.D., Chair

---

Date

California State University, Northridge

## ACKNOWLEDGMENTS

There are numerous people that I would like to show my appreciation and whom without I would not have been able to complete this thesis. First, I thank my great advisor Elena Miranda for all of the help, snacks, motivation, and patience.

I would like to thank John Wakabayashi, California State University-Fresno Professor, for his continued support. I would also like to thank the USN and USFS for the endless flexibility and financial support towards living expenses and tuition. Thanks to Dr. Mary Leech and Dr. Clive Hayzelden at California State University-San Francisco for the use of their EBSD-equipped FE-SEM and for their invaluable insight and troubleshooting assistance, and the CSUN Department of Geological Science for funding my EBSD acquisition. I would also like to thank my committee members Dick Heermance and Doug Yule for their invaluable insights and support.

## TABLE OF CONTENTS

Signature page.....	ii
Acknowledgments.....	iii
LIST OF TABLES.....	vi
LIST OF FIGURES.....	vii
ABSTRACT.....	ix
Chapter 1 : INTRODUCTION.....	1
The Strength of Continental Crust.....	1
Why Study the South Mountains Metamorphic Core Complex.....	5
Objectives.....	6
Flow Laws.....	6
Deformation Mechanisms.....	8
Chapter 2 : GEOLOGY OF THE SOUTH MOUNTAINS.....	12
Geologic Units.....	12
Tertiary Structural Geology.....	14
Mylonitization.....	15
Chapter 3 : METHODS.....	18
Sample Collection.....	18
Sample Selection and Preparation.....	18
Microstructural Analysis.....	19
EBSD Analysis.....	19
Grain Size Measurements.....	21
Chapter 4 : RESULTS.....	23
Microstructures.....	23
Type I.....	23
Type II.....	26
EBSD Data from Type I Fabrics.....	27
EBSD Data from Type II Fabrics.....	31
Constraints on Deformation Conditions.....	48
Grain Size.....	48

Differential Stress .....	51
Strain Rate .....	53
Chapter 5 : DISCUSSION .....	55
Slip Systems and Temperature Interpretations.....	57
Quartz Slip Systems.....	57
Feldspar Slip Systems.....	60
Dominant Deformation Mechanisms .....	60
Comparison of Natural and Predicted Conditions.....	62
Chapter 6 : IMPLICATIONS FOR STRAIN LOCALIZATION.....	74
CONCLUSIONS.....	75
REFERENCES .....	76
APPENDIX A : THIN SECTION AND POLISHING PROCEDURES .....	80
APPENDIX B : EBSD PROCESSING AND RE-INDEXING PROCEDURES.....	82
APPENDIX C : EBSD BEAM MAPS AND POLE FIGURES .....	86
APPENDIX D : EDS CHEMISTRY FIGURES .....	104

## LIST OF TABLES

Table 4.1 Primary modal mineralogy of rock samples .....	48
Table 4.2 Summary of quartz grain size and differential stress for the South Mountains mylonites .....	52
Table 5.1 Interpreted slip systems and deformation temperatures .....	59

## LIST OF FIGURES

Figure 1.1 Geographic distribution of metamorphic core complexes in the Western United States.....	5
Figure 1.2 Dynamic recrystallization regimes .....	10
Figure 2.1 Geologic map of the South Mountains and geologic cross section of Ahwatukee Ridge, South Mountains .....	13
Figure 2.2 Chronology of geologic events in the South Mountains .....	16
Figure 2.3 Interpreted evolution of low-angle normal shear zones or low-angle detachment faults .....	17
Figure 3.1 Cross section along sample collection transect .....	18
Figure 4.1 Cross polarized photomicrographs of quartz and feldspar microstructures ....	26
Figure 4.2 EBSD beam map and EBSD results for sample SM-07-05-02, study region A .....	31
Figure 4.3 EBSD beam map and EBSD results for sample SM-07-05-02, study region B.. ..	34
Figure 4.4 EBSD beam map and EBSD results for sample SM-07-07, study region A... 38	
Figure 4.5 EBSD beam map and EBSD results for sample SM-07-07, study region B <sub>1</sub> .. 42	
Figure 4.6 Orthoclase pole figures for sample SM-07-07, study region B <sub>1</sub> .....	43
Figure 4.7 EBSD beam map and EBSD results for sample SM-07-07, study region B <sub>2</sub> .. 47	
Figure 4.8 Orthoclase pole figures for sample SM-07-07, study region B <sub>2</sub> .....	47
Figure 4.9 Line intercept measurements for quartz and feldspar grains in South Mountains samples .....	51
Figure 4.10 Recrystallized quartz grain size piezometer of Stipp and Tullis (2003) .....	53
Figure 5.1 Quartz slip directions and slip systems schematic .....	58
Figure 5.2 Interpreted temperatures for various active slip systems and correlating South Mountain samples.....	59
Figure 5.3 Mohr construction for our estimated maximum and minimum brittle-plastic transition in the South Mountains of ~120 and 60 MPa.....	65
Figure 5.4 Deformation mechanism maps for wet quartz at 500°C .....	67

Figure 5.5 Deformation mechanism maps for wet quartz at 600°C ..... 68

Figure 5.6 Differential stress-temperature curves for quartzite flow laws at strain estimates calculated for the South Mountains ( $10^{-12}$  to  $10^{-13}$  s<sup>-1</sup>) ..... 70

Figure 5.7 Log stress-log strain rate curves for dislocation creep for quartzite and albite flow laws at 500°C and 600°C ..... 73

## ABSTRACT

# EBSD AND MICROSTRUCTURAL ANALYSIS OF QUARTZOFELDSPATHIC ROCKS FROM THE SOUTH MOUNTAINS, ARIZONA: AN EVALUATION OF FLOW LAWS AND CRUSTAL RHEOLOGY

By

David Annis

Master of Science in Geology

The strength of the middle and lower continental crust is approximated by experimentally-derived flow laws that describe plastic flow of single mineral phase or polyphase aggregates, but there is little consensus about which aggregate compositions may best characterize this part of the crust. In this thesis, I use microstructural and electron backscatter diffraction (EBSD) analyses to evaluate the strength of naturally-deformed quartzofeldspathic middle crust exposed in the South Mountains metamorphic core complex, Arizona. These results are compared to published quartz and feldspar experimental flow law data to evaluate the applicability of these flow laws for assessing the strength of middle continental crust.

Microstructural analysis of the constituent minerals in the South Mountains granodiorite shows that strain is accommodated by crystal plastic deformation and dynamic recrystallization in quartz, limited crystal plasticity in orthoclase feldspar, and brittle microfaulting in plagioclase feldspar. The microstructures suggest that quartz is the weakest phase in the rock, and the crystal plastic deformation of the abundant quartz dominates the strain localization process during mid-crustal shearing. EBSD analyses reveal that dynamically recrystallized quartz grains exhibit lattice preferred orientation

(LPO) indicative of basal and rhomb slip, and that orthoclase and plagioclase feldspar exhibit limited evidence for LPO and an absence of LPO, respectively. Together, the microstructural and EBSD data suggest that the operative deformation mechanism in the interconnected network of abundant quartz is dislocation creep, whereas the dominant deformation mechanism in the feldspars is brittle fracturing.

I use the 'wet' quartz flow laws of Hirth et al. (2001) and Rutter and Brodie (2004) to create deformation mechanism maps in which I compare the predicted strength of quartz aggregates to the observed strength of the granodiorite mylonites of the South Mountains metamorphic core complex. Given the deformation conditions of the South Mountains mylonites, the strength of these rocks are best fit by the quartzite flow law of Hirth et al. (2001) at temperatures  $\sim 500^{\circ}\text{C}$ , and the quartzite flow law of Rutter and Brodie (2004) at temperatures of  $\sim 600^{\circ}\text{C}$ . The results suggest that the strength of quartz may be a proxy for the bulk strength of the rock during ductile deformation, and that quartz flow laws may provide the best estimate of the strength of deforming continental crust where quartz is abundant, interconnected, and deforming by dislocation creep.

## CHAPTER 1 : INTRODUCTION

### **The Strength of Continental Crust**

The brittle-plastic transition (BPT) represents the maximum strength of continental crust, and therefore acts as a ‘stress guide’ during continental deformation (Sibson, 1983). The deformation above the BPT is brittle and localized along discrete seismogenic faults, and the deformation below the BPT is more ductile in nature and distributed across shear zones. It is important to quantify the strength of the crust at the BPT because (1) episodic earthquake events in the brittle upper crust are influenced by and linked to the flow of ductile rocks immediately beneath the BPT; (2) the “relaxation” of the crust after a seismic event is accommodated by ductile flow, and the speed and effectiveness of this flow is related to the strength of ductile rocks at the BPT, and (3) different rheological parameters (e.g. composition, differential stress, strain rate, temperature, grain size, and fluid content) affect the strength of the crust, which controls the depth of the BPT. Weaker and stronger rocks lead to a shallower and deeper BPT, respectively. A deeper BPT means that earthquakes can occur deeper within the crust, so it expands the region of the crust that is prone to seismic failure. The strength of the upper crust is pressure-sensitive, and increases linearly with depth according to Byerlee’s Law (Brace and Kohlstedt, 1980; Burgmann and Dresen, 2008; Byerlee, 1978; Sibson, 1983).

In contrast, the strength of middle and lower crustal rocks below the BPT decreases with depth because these rocks deform by plastic deformation mechanisms that are temperature-sensitive (Burgmann and Dresen, 2008). The strength of these ductile rocks is estimated by flow laws, or equations that describe steady-state plastic flow

during deformation, that are experimentally determined in the laboratory for single phase or polyphase aggregates designed to imitate the composition of continental crust.

However, it remains a subject of debate whether or not flow laws accurately describe the behavior of naturally-deformed continental crust because these mid- to lower crustal rocks are not exposed at the surface during active deformation (Brace and Kohlstedt, 1980; Ji and Zhao, 2003; Kohlstedt et al., 1995; Stipp and Kunze, 2008).

It has been argued that flow laws may not accurately describe the flow of crustal rocks below the BPT because single-phase quartz or plagioclase flow laws oversimplify the composition of heterogeneous continental crust, and because relatively old mid- to lower continental crustal rocks that have been multiply deformed may be weaker than predicted by initially undeformed laboratory samples, leading to a shallower BPT (Burgmann and Dresen, 2008; Ji et al., 2003; Tullis, 2002). Oversimplification of the composition of crustal rocks will affect the predicted strength of the crust by either over or underestimating rock strength, which affects the predicted depth of the BPT.

Evaluating whether or not flow laws accurately predict the strength of naturally-deformed continental crust below the BPT requires a combination of field observations, experimental work and theoretical modeling in extensional, compressional, and transform settings (Tullis, 2002).

Quartz is identified in many published studies as being the weakest phase in a quartzofeldspathic rock deforming under crustal conditions and therefore has a dominant effect on the bulk rheology (Behr and Platt, 2011; Dell'Angelo and Tullis, 1989; Hacker et al., 1992; Stipp and Kunze, 2008). Crystal plastic deformation is preferentially accommodated in quartzofeldspathic rocks by quartz at low and moderate temperatures,

due in part to the larger burgers vector and more limited slip systems for feldspar (Dell'Angelo and Tullis, 1996). Rock strength analyses of both quartzites and quartzofeldspathic rocks in the Whipple Mountains suggest that quartzofeldspathic rocks with >60 modal percent feldspar are up to five times stronger than quartzites (Hacker, 1992). Therefore the modal percentage of feldspar in continental crustal rocks likely plays a major role in affecting crustal strength when feldspar is an abundant phase, particularly at low temperatures and high strain rates (Tullis, 2002; Burgmann and Dresen, 2008).

Extensional environments are ideal locations for field investigation of mid- to lower crustal strength and rheology because normal faults with large slip expose middle to lower continental crustal rocks from beneath the BPT (Hacker, 1992). Rocks that are tectonically transported from beneath the BPT to shallower crustal levels undergo progressively more brittle deformation as they near the BPT, resulting in strain localization into progressively narrower shear zones. Strain localization is strongly influenced by the rheological properties of individual mineral phases in the ductilely-deforming polyphase continental crust. The rheological properties (differential stress, strain rate, temperature, grain size, and fluid content) of minerals in rocks that undergo strain localization at the BPT can therefore be used to interpret the strength of crust immediately below the BPT (Burgmann and Dresen, 2008). Rheological properties of rocks are measured and used with flow laws to compare predicted and natural deformation conditions. If predicted conditions are representative of natural conditions, then the flow laws accurately represent the strength of ductile rocks at the BPT.

Metamorphic core complexes are ideal places to study the rheology of continental crust during and/or after deformation because (1) core complexes are prevalent within the North American Cordillera (Figure 1.1), (2) quartzofeldspathic rocks are the dominant rock type of mylonitic shear zones in many metamorphic core complexes, (3) kinematic models for the development of mylonitic shear zones are well developed for rocks with a high modal abundance of quartz, thus enabling the application of quartz microstructures to the understanding of cooling and depressurization history of the rocks, and (4) the ages of the rocks, detachment faulting, mylonitization, and cooling histories are well constrained in some Cordilleran core complexes (i.e. the Whipple Mountains, South Mountains, and Ruby Mountains) (Hacker et al., 1990; Hacker, 1992).

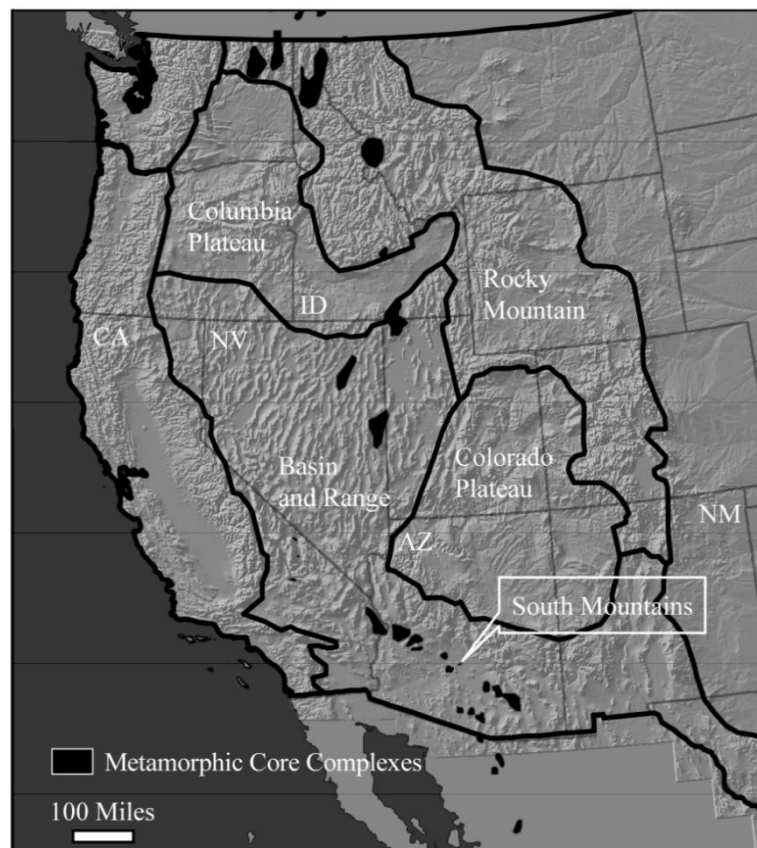


**Figure 1.1** Geographic distribution of metamorphic core complexes and geologic provinces of the Western United States. The South Mountains study area is located in the southern Cordillera.

### **Why Study the South Mountains Metamorphic Core Complex**

The purpose of this study is to evaluate the strength and rheology of naturally deformed quartzofeldspathic mylonites from the middle crust during extension in the South Mountains metamorphic core complex, Arizona, and compare these results to published quartz and feldspar flow laws to evaluate the applicability of these flow laws for assessing the strength of middle continental crust. The South Mountains metamorphic core complex is an ideal location to evaluate crustal rheology because (1) low-angle fault structures have exposed mid-crustal quartzofeldspathic rocks that were intruded immediately before mylonitization and therefore lack multiple deformation events; (2) the relative speed of development of the metamorphic core complex not only accommodated 2-5 km of tectonic transport (Reynolds, 1985), but exhumed continental crustal rocks quickly, at a rate of extension of  $\sim 0.3 \text{ cm yr}^{-1}$  (Fitzgerald et al., 1993), which minimized retrograde metamorphism or annealing; and (3) the deformation conditions (e.g. temperature, strain rate) are well constrained by thermochronological, microstructural, and structural observations (Reynolds, 1985; Reynolds et al., 1986; Davis et al., 1986; Smith et al., 1991; Fitzgerald et al., 1993; Livaccari et al., 1995). The South Mountains have a simplistic tectonic/structural history because they are located east of the Sevier fold-and-thrust belt, which is critical since Sevier structures (thrust faults) and mid-Tertiary low-angle normal faults (South Mountains metamorphic core complex) are kinematically different, but geometrically similar in that they are both low-angle fault surfaces. In contrast, the South Mountains are located within the geographical extent of the Laramide orogeny, but Laramide-age reverse faults and mid-Tertiary low-

angle normal faults can be distinguished by kinematic shear sense indicators and by the high- and low-angle of fault dip, respectively.

## **Objectives**

The primary objectives of this study are to evaluate the strength of the granodiorite mylonites that are structurally below the only detachment fault exposure in the South Mountains, and to compare the observed strength of the naturally-deformed mylonites with the strength predicted by flow laws to evaluate whether single-phase flow laws are accurate estimates of continental crust strength at the BPT within extensional environments. To evaluate the strength of the mylonites, I use microstructural and EBSD analyses to: (1) estimate modal percentages of constituent minerals and identify the mineral phase or phases in which strain is localized, (2) identify the dominant deformation mechanisms that accommodate strain localization, and (3) estimate temperature, grain size, differential stress, fluid content, and strain rate during mylonitization and incipient strain localization near the BPT. To compare the observed strength of the naturally-deformed mylonites with that predicted by single-phase flow laws, I use deformation mechanism maps to compare the predicted strain rates of quartz with the calculated strain rates of granodiorite mylonites at the temperature, grain size, differential stress, and fluid content determined for the mylonites by microstructural and EBSD analyses.

## **Flow Laws**

The rheology of plastically-deforming minerals and rocks is described by flow laws. Flow laws are stress-temperature-strain rate constitutive relations that are derived from laboratory experiments and extrapolated to geological conditions. Flow laws can be

used to evaluate the strength of naturally-deformed rocks when natural deformation occurs at steady-state conditions and by the same mechanisms used during experiments. Under these conditions flow laws can be used to quantify one of the variables, temperature, stress, strain rate, if the other two variables are known (Hacker et al., 1990).

Most flow laws describe the deformation of a single phase due to the infinite combination of relative phases, phase proportions, and distinct microstructures for each rock composite (Ji et al., 2003). Multiphase rocks (e.g. granitic rocks) generally have nonlinear temperature, strain rate, and grain size dependent rheologies. Therefore, the extrapolation of monophasic flow laws to evaluate multiphase naturally-deformed rocks assumes that the bulk rock strength is equal to the strength of the dominant phase and that strain and strain rates are homogenous within crustal rocks (Bons and Urai, 1994; Burgmann and Dresen, 2008). The applicability of single phase flow laws to evaluate the bulk rock strength is dependent on the rheological properties of the constituent mineral phases (e.g. quartz and feldspar) and their volume proportions (Handy, 1994).

The rheology of multiphase rocks is tied to the volume proportion and geometric arrangement of its modally abundant constituent mineral phases (Handy, 1994). Handy (1994) classified two types of structural frameworks to define volume proportions and geometric arrangements for both experimentally deformed aggregates and naturally-deformed rocks (1) a load-bearing framework of a strong phase that contains isolated pockets of a weaker phase (porphyroblasts), and (2) an interconnected matrix or layers of a weak phase separating porphyroclasts or boudins of the stronger phase. Handy (1994) suggests that stress and strain rate is higher in the weaker phase in an interconnected weak framework. Handy (1994) interprets the higher stresses and strain rates as evidence

that strain is preferentially localizing in the weaker phase in multiphase rocks, for weak phase fractions greater than ~20% (Handy, 1990; Handy, 1994). Owing to the influence of the interconnected weak framework mineral phase on the bulk rock rheology most microstructural and rheological studies utilize single phase flow laws (e.g. quartz or feldspar) to evaluate and constrain the rheology of naturally-deformed rocks.

### **Deformation Mechanisms**

Grain scale mechanisms by which minerals and rocks deform are called deformation mechanisms, and they are broadly divided into brittle and ductile categories (Passchier and Trouw, 1998). Brittle deformation or deformation by fracture and frictional processes is called cataclastic flow (cataclasis) (Passchier and Trouw, 1998). In contrast, ductile deformation by intracrystalline plastic flow is called crystal plastic deformation, which is commonly accommodated by either dislocation or diffusion creep deformation mechanisms (Passchier and Trouw, 1998).

Dislocation creep, or grain size insensitive creep, is accommodated by glide and climb of dislocations (lattice defects) and the rate of dislocation creep is controlled by the rate at which dislocations can climb out of the lattice (Hirth et al., 2001; Ji et al., 2003). The rate at which dislocations climb is increased with trace amounts of water (Hirth and Tullis, 1992; Tullis, 2002). Strain during dislocation creep is accommodated by grain rotation towards orientations that promote slip or glide along the easiest and dominant slip systems for the material (Mehl and Hirth, 2008). Dislocation creep is commonly accompanied by dynamic recrystallization and is associated with the generation of a lattice preferred orientation (LPO) (Mehl and Hirth, 2008; Burgmann and Dresen, 2008; Gleason and Tullis, 1993).

The significance of dynamic recrystallization is that it can accommodate steady state flow or lead to strain localization and rheological weakening. Increasing strain at a constant temperature and flow parameter will theoretically strengthen an LPO pattern, which is indicative of dislocation creep or dynamic recrystallization (De Bresser et al., 2001). However a transition from grain size insensitive creep to grain size sensitive creep or a relative reduction in grain size will lead to rheological weakening and strain localization within cm to km-scale shear zones (De Bresser et al., 2001).

Hirth and Tullis (1992) identified three dynamic recrystallization regimes in experimentally deformed quartzites that operate at different temperatures and strain rates, and are characterized by three distinct recrystallization mechanisms and associated microstructures (Post and Tullis, 1999). In order of increasing deformation temperature, the three regimes of dynamic recrystallization include: Regime I bulging recrystallization (BLG), Regime II subgrain rotation recrystallization (SGR), and Regime III high-temperature grain boundary migration recrystallization (GBM) (Figure 1.2) (Hirth and Tullis, 1992; Passchier and Trouw, 1998).

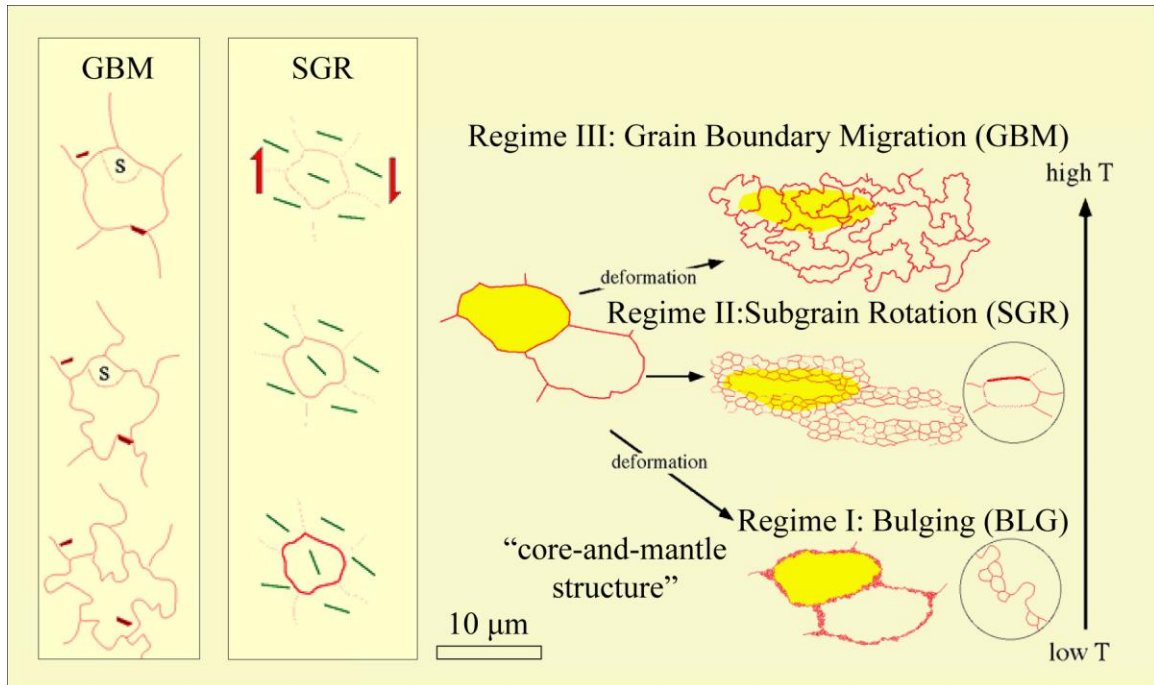


**Figure 1.2** Diagram illustrating the three mechanisms of dynamic recrystallization on the grain scale after Hirth and Tullis (1992). During Regime I bulging recrystallization (BLG), the grain boundaries migrate in the direction of the grain with a higher dislocation density, producing bulging grain boundaries that result in the enclosure of a new grain called a “neoblasts”. In Regime II subgrain rotation recrystallization (SGR), a new grain is formed by progressive rotation of a subgrain away from its ‘host’ grain. During Regime III grain boundary migration, elevated temperatures promote easy movement of grain boundaries through entire crystals to remove dislocation defects, resulting in irregular and lobate grain boundary textures. The diagram shows how the types of microstructures associated with each regime change with increasing temperatures of deformation. Modified from Passchier and Trouw (1998).

Diffusion creep, or grain size sensitive creep, is accommodated by the migration of vacancies (lattice defects) from areas of low to high compressive stress. Diffusion creep occurs at low strain rates or at very high temperatures. Diffusion creep is grain size sensitive and favors small grain sizes (<10 μm), since small grain sizes have shorter diffusion paths for vacancies to travel. Diffusion creep is dominantly accommodated by grain boundary sliding, which results in phase proportions and a randomized LPO (Mehl and Hirth, 2008; Burgmann and Dresen, 2008; Gleason and Tullis, 1993).

Many naturally-deformed rock studies involving various rock compositions from various tectonometamorphic settings have correlated natural conditions to experimental conditions (Hirth and Tullis, 1992; Stipp et al., 2002; Stipp and Kunze, 2008; Stockhert et al., 1999). Rheological parameters for quartz were confirmed to be relatively robust features in natural fault zones because the microstructures are extremely sensitive to deformation conditions (e.g. differential stress, pressure, temperature, water content, and strain rate) (Stockhert et al., 1999). However, rheological parameters should only be interpreted from experimental conditions, when natural deformation conditions are consistent with experimental conditions (Stockhert et al., 1999).

Some of the implications for this type of study on the field of rheology and microstructures include: (1) “calibration” of experimentally derived flow laws using naturally deformed continental crustal rocks, (2) determining deformation conditions for natural rocks using experimental data, and (3) evaluating strain localization processes in crustal scale shear zones where strain localized quickly to form through-going brittle fault systems.

## **CHAPTER 2 : GEOLOGY OF THE SOUTH MOUNTAINS**

### **Geologic Units**

The South Mountains are composed of two fundamentally different geologic sections, a western section composed of multiply deformed Precambrian rocks (1.6-1.7 Ga (Reynolds, 1985)) and an eastern section composed of a middle Tertiary composite pluton (25-22 Ma (Reynolds, 1985; Reynolds et al., 1986)) that is synkinematic with respect to core complex development (Figure 2.1). The composite pluton consists of three intrusive phases, which are listed in interpreted order of intrusion: the South Mountains Granodiorite, Telegraph Pass Granite, and Dobbins Alaskite (Figure 2.1; Reynolds, 1985; Reynolds et al., 1986). This study only deals with the South Mountains Granodiorite because it is the most abundant rock type in the footwall of the low-angle detachment fault. Both the Precambrian rocks and the composite Tertiary pluton have been intruded by numerous, north-northwest-trending middle Tertiary dikes (Reynolds, 1985).

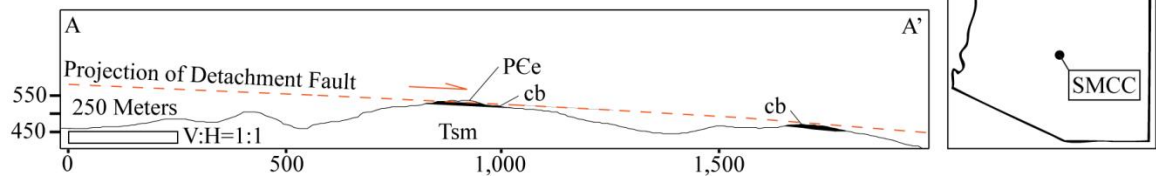
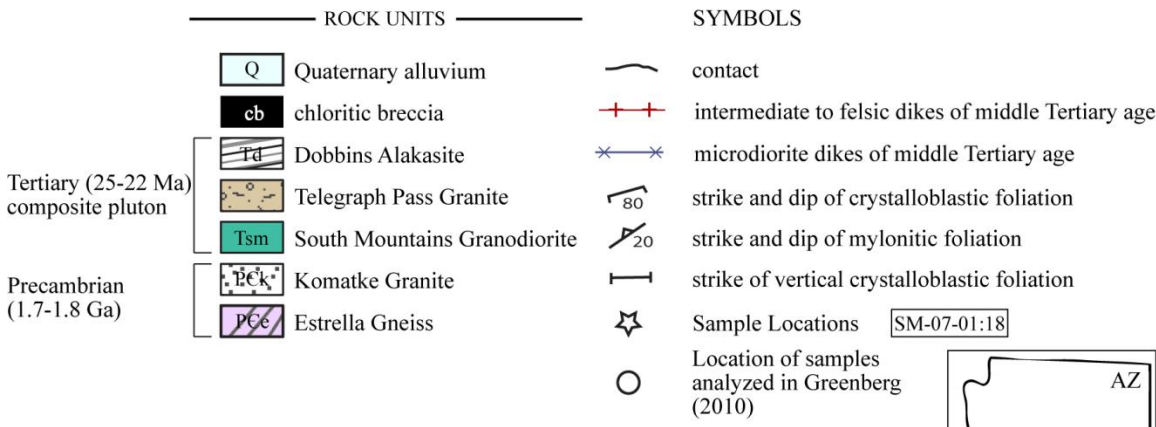
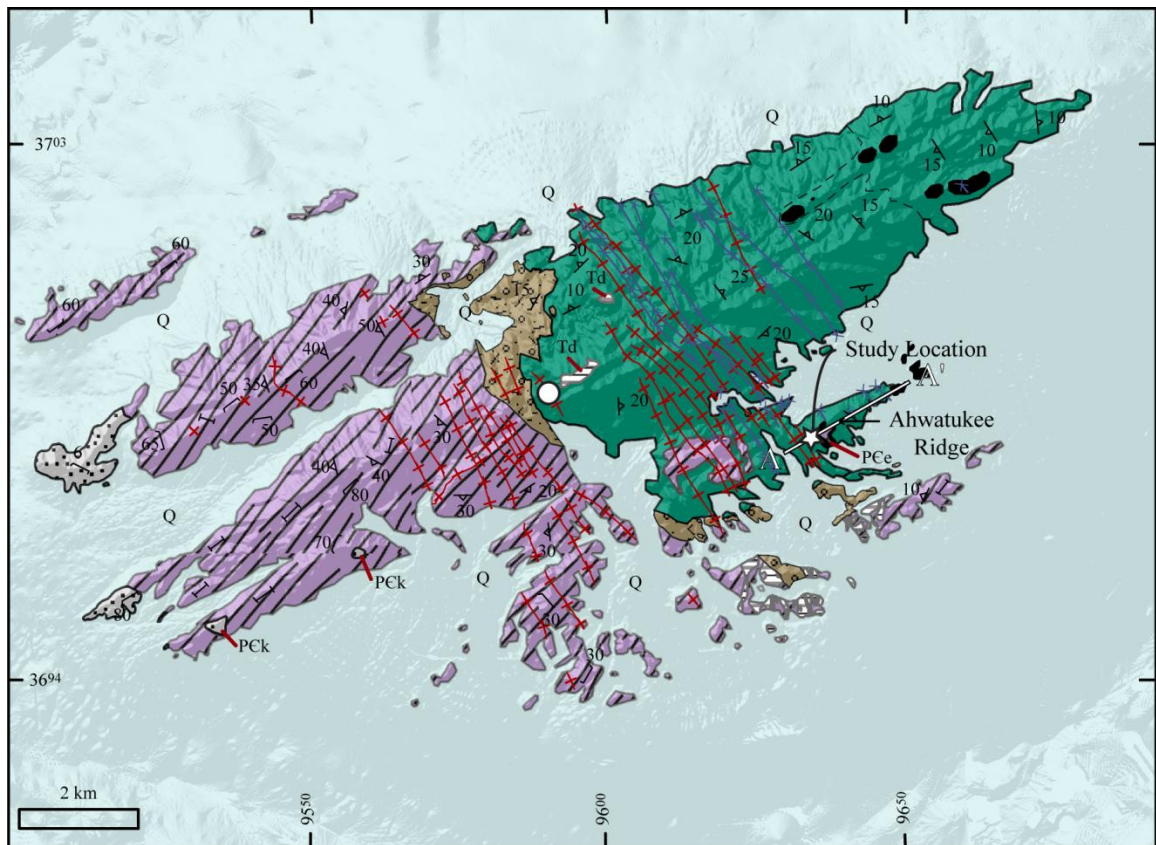


**Figure 2.1** Geologic map of the South Mountains metamorphic core complex (SMCC) in central Arizona, and cross-section of Ahwatukee Ridge (study area). Ahwatukee Ridge is the only exposure of the low angle detachment fault in the South Mountains.

## **Tertiary Structural Geology**

The three phases of the composite Tertiary pluton are synkinematic with extension; Tertiary extension associated with core complex development was accommodated in a top-to-the-east-northeast direction along a low-angle detachment fault based on the prevalence of east-northeast-trending stretching lineations (Reynolds, 1985). Much of the low angle detachment fault is eroded, except at Ahwatukee Ridge, the study area for this analysis (Figure 2.1). Rock types that comprise the footwall of the detachment fault at Ahwatukee Ridge include chlorite breccia rock fragments and South Mountain Granodiorite, whereas the hanging wall is composed of Precambrian rocks. The detachment fault surface is considered to have closely followed the current topographic crest along the eastern section of the range and to have projected well above the surface over the western section of the range (Figure 2.1) (Livaccari et al., 1995).

Extension within the South Mountains was accommodated by a ~100 to 200 m wide ductile shear zone, and this shear zone underwent progressive strain localization under increasingly brittle conditions until strain was localized along a discrete planar surface, or a brittle detachment surface (Reynolds, 1985; Reynolds et al., 1986; Livaccari et al., 1995). Previous studies estimate that ductile extension occurred at relatively shallow crustal depths, within 5 to 10 km of the surface (Reynolds, 1985) and at a rate of extension of  $\sim 0.3 \text{ cm yr}^{-1}$  (Fitzgerald et al., 1993). The rate of extension is for brittle, localized deformation along the detachment fault only; during ductile shear the strain rate slows down because it is distributed and not localized, therefore the slip rate is a maximum estimate. Brittle fabrics associated with detachment faulting include both the chlorite breccia and the uppermost part of the mylonites, directly below the breccia. The

chlorite breccia is composed of altered fragments of the South Mountains Granodiorite, making up the uppermost tens of meters of the footwall (Reynolds, 1985).

### **Mylonitization**

Mylonitization in the South Mountains metamorphic core complex was synkinematic to the Tertiary pluton and initiated around ~25-22 Ma and continued until ~20-19 Ma (Reynolds, 1985; Reynolds et al., 1986) (Figure 2.2). The upper limit of this range is defined by the age of emplacement of the composite Tertiary pluton. The cessation of mylonitization at ~20-19 Ma is constrained by the K/Ar biotite ages of the granitic rocks, which represent the age at which the rocks cooled below  $300 \pm 50^\circ \text{C}$  (Reynolds, 1985; Reynolds et al., 1986). Ductile deformation associated with core complex development was followed by brittle deformation, which is also associated with core complex development, was active from ~ 20 to 17 Ma (Figure 2.3) (Reynolds, 1985; Reynolds et al., 1986).

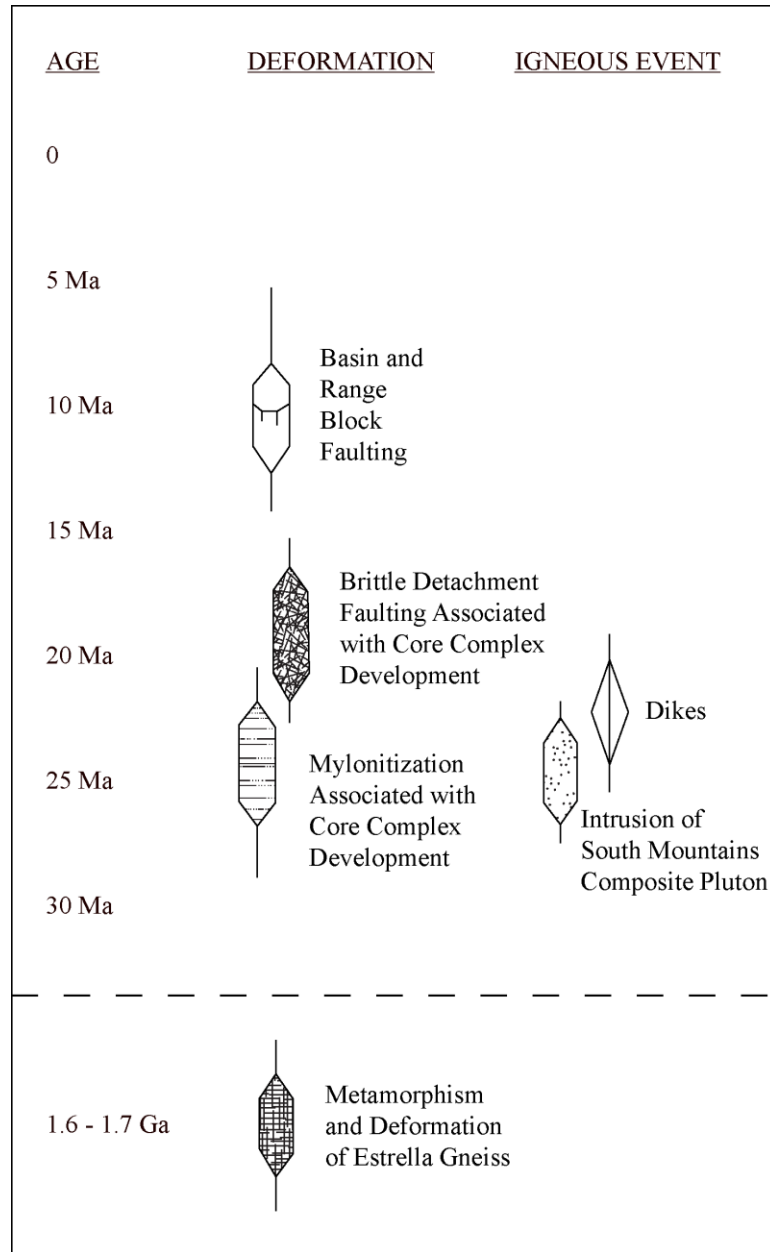


**Figure 2.2** Chronology of geologic events in the South Mountains. The South Mountains composite pluton was emplaced into Proterozoic crystalline basement rocks (Estrella Gneiss) at ~25-22 Ma (Reynolds, 1985; Reynolds et al., 1986). Mylonitization associated with core complex development was active from ~25 to 19 Ma (Reynolds, 1985; Reynolds et al., 1986). The primary deformation was progressively overprinted by localized ductile shear zones and eventually by brittle detachment faulting associated with core complex development from ~20 to 17 Ma (Reynolds, 1985; Reynolds et al., 1986; Fitzgerald et al. 1993). Figure modified from Reynolds (1985).

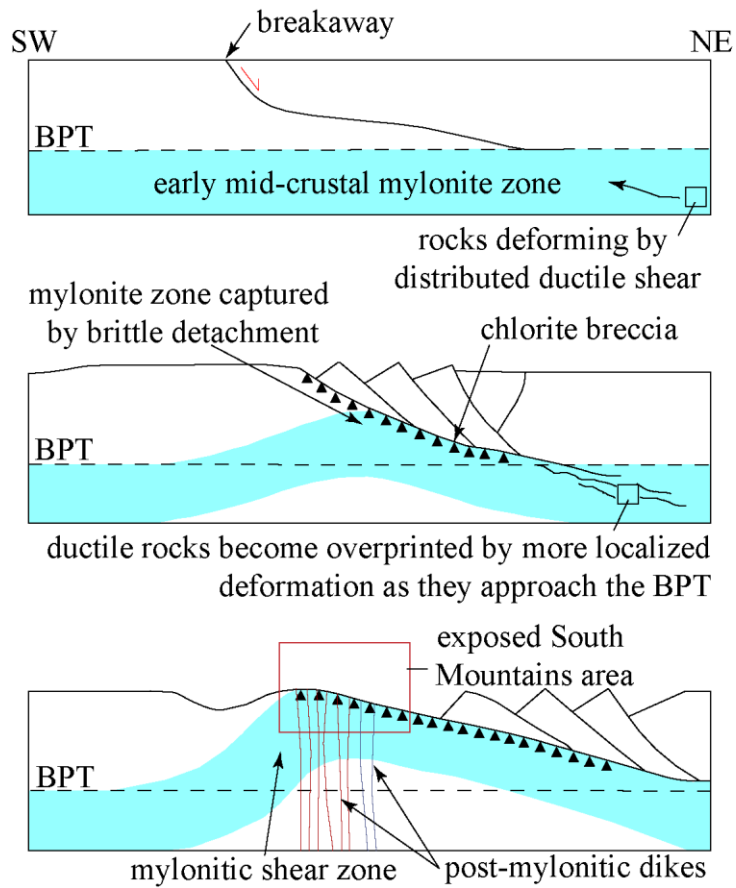


**Figure 2.3** Interpreted evolution of low-angle normal shear zones or low-angle detachment faults, showing progressive denudation of deep crustal rocks. Post-mylonitic dikes include intermediate to felsic (red) and microdiorite dikes (blue). Modified after Behr and Platt (2011).

## CHAPTER 3 : METHODS

### Sample Collection

The samples used in this study were collected along Ahwatukee Ridge in the South Mountains, where the only exposure of the Tertiary detachment fault surface exists (Figure 2.1) (Reynolds, 1985; Reynolds et al., 1986). Eighteen samples were collected from a 450 m-long transect across the footwall, detachment fault, and hanging wall (Figure 3.1). The eighteen samples are representative of a structural thickness of ~70 m of the shear zone. The rock units that crop out along the transect include protomylonitic to mylonitic South Mountains Granodiorite, chloritic fault breccia derived from South Mountains Granodiorite, and Estrella Gneiss (Figure 3.1). The transect was chosen to enable the collection of footwall samples in which mylonitic fabric intensity and strain localization can be compared with structural depth below the detachment fault surface. Three oriented granodiorite mylonite samples from the footwall, SM-07-05, SM-07-07, and SM-07-08, were chosen for detailed microstructural and EBSD analyses.

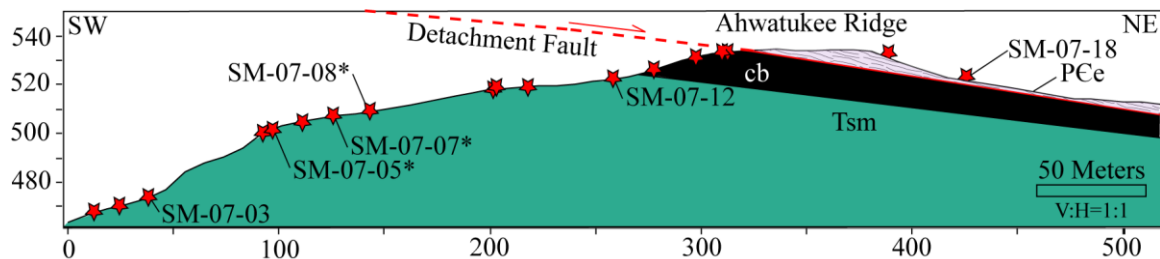


**Figure 3.1** Cross section along sample collection transect showing the locations of the samples with respect to the low angle detachment fault. Rock units designated by symbols: PCE = Estrella Gneiss; cb = chloritic breccia; Tsm = South Mountains Granodiorite. \*Samples used for EBSD analysis.

### Sample Selection and Preparation

The three samples selected for this thesis research were chosen because they represent the onset of strain localization in the footwall, as interpreted by a dramatic

increase in macroscopic mylonitic fabric intensity with decreasing structural depth beneath the detachment fault. Each of these oriented samples were cut perpendicular to mylonitic foliation and parallel to the stretching lineation so that the thin sections are cut in the motion plane (Appendix A). Microstructural analysis was performed on all three samples, and 3 micro-study areas within each sample were selected for EBSD analysis.

### **Microstructural Analysis**

Microstructural analysis is used to identify and describe deformation microfabrics in thin section, and to (1) estimate the modal proportions for the primary mineral phases (e.g. quartz, orthoclase, albite), (2) describe the quartz, orthoclase, and plagioclase microfabrics in the mylonites, (3) estimate the temperature conditions under which the mylonitic fabric developed, (4) interpret the associated pressure and/or temperature conditions under which those microfabrics develop, and (5) interpret the dominant deformation mechanisms (grain-scale deformation processes) that accommodate strain during microfabric development.

Microstructural analysis is essential for the selection of appropriate study areas for EBSD analysis. EBSD study areas were selected that include (1) layers of weaker phases (e.g. quartz) that exhibit dynamic recrystallization separating porphyroclasts (e.g. feldspar) that mostly lack intracrystalline deformation structures, and (2) grains with microstructures suggestive of peak microfabric development.

### **EBSD Analysis**

Electron backscatter diffraction (EBSD) provides a quantitative method to determine microstructural information about the crystallographic nature of minerals; for a brief discussion of EBSD and its applications, see Appendix B.

Prior to collection of EBSD data, thin sections were ultra-polished (Appendix A) in order to obtain high quality diffraction patterns, and sputter-coated with carbon (~2 to 5 nm thick) to help limit charging during SEM analysis. EBSD data were collected at California State University-San Francisco on an EBSD-equipped Zeiss Ultra 55 field emission gun scanning electron microscope at 20 kV. The samples were analyzed at a working distance of 16-20 mm. The HKL Channel 5 software was used to automatically acquire and index diffraction patterns from beam maps using the specific working conditions outlined in Appendix B. Energy Dispersive Spectroscopy (EDS) data were collected for primary elements (e.g. Si, Al, K, Na, and Ca) simultaneously with EBSD analysis to assist with phase discrimination during reprocessing. Subsequent reprocessing of saved diffraction patterns was completed with HKL Channel 5 software at California State University Northridge to remove misindexing and nonindexing errors.

EBSD analysis was used to describe the shape and distribution of grain and subgrain boundaries, and to measure the crystallographic orientations of individual grains or regions within grains on a micro-scale. The shape and distribution of grain and subgrain boundaries are used to confirm the presence or absence of dynamic recrystallization regimes identified during microstructural analyses. The crystallographic orientations are used to interpret the presence or absence of LPO in dynamically recrystallized minerals. The presence or absence of LPO is used to distinguish between the crystal plastic deformation mechanisms of dislocation creep and diffusion creep, respectively, in dynamically recrystallized minerals. Where LPO is present in a dynamically recrystallized mineral, EBSD analyses permit the identification of the crystal slip system that accommodated development of the LPO. In this study, I define grain

boundaries as those separating grains with misorientations greater than  $10^\circ$ , and I define subgrains as those separating intra-grain regions with misorientations greater than  $2^\circ$  and less than  $10^\circ$ . Crystallographic orientation data are displayed in equal area lower hemisphere scatter plots and in contoured pole figures when more than 200 crystallographic orientations are measured, and each measurement is representative of an individual grain.

Modal proportions of mineral phases for samples used for EBSD analysis were quantified petrographically and confirmed with EBSD to assess the quality of Channel 5 software indexing during post-processing. Mineral phases were confirmed with EBSD by evaluating elemental ratios from EDS data (e.g. K, Na, Ca, Si, Al) with Channel 5 software. EDS data consists of 30,000 to 50,000 data points, and modal proportions of the primary modal mineralogy (e.g. quartz, orthoclase, albite) for each data point were quantified with Channel 5 software.

### **Grain Size Measurements**

Mean grain sizes were calculated for quartz, albite, and orthoclase using the Channel 5 software line-intercept tools following the recommendation by Humphreys (2001) and Hacker et al. (1990). Intercepts were measured from grain boundaries identified from EBSD beam maps, when individual grains consisted of ~5-10 data points across a grain. A minimum number of ~200 quartz intercepts (one point per a grain) were measured parallel to both the maximum stretching (X) and shortening (Z) directions independently for each phase for a determination of grain size. The arithmetic mean is used rather than the geometric mean for consistency with experimental conditions from which the empirical piezometers and flow laws were derived. Grain size is calculated by

multiplying line intercepts by a geometric correction factor of 1.5. Grain size error is calculated for a 95% confidence level using Microsoft Excel data analysis tools.

Porphyroclasts were identified by a bimodal grain size distribution and preferentially excluded from this analysis.

## CHAPTER 4 : RESULTS

### Microstructures

Two microstructural types reflecting specific stages of microstructural development with distinct deformation microfabrics were identified in the South Mountains metamorphic core complex (SMCC) samples. I refer to these distinct microstructures as Type 1 and Type 2 mylonites, and I describe their characteristics in the forthcoming sections.

#### *Type I*

Type I mylonites are characterized by quartz grains that have sinuous and irregular grain shapes; many large grains (100-200  $\mu\text{m}$ ) have lobate grain boundaries, with individual lobes ranging from 30-50  $\mu\text{m}$  in diameter (Figure 4.1A). These grain shapes are consistent with microstructures indicative of GBM dynamic recrystallization. Within the large, lobate grains, there is subgrain development both near the centers and rims of the grains. Subgrains are  $\sim 20$   $\mu\text{m}$  in diameter (Figure 4.1A), and recrystallized grain sizes ( $\sim 20$ -30  $\mu\text{m}$ ) are slightly larger than the subgrains within the grains that they are replacing (Figure 4.1A).

Orthoclase and albite grains form porphyroclasts ( $\sim 400$   $\mu\text{m}$ ) within the mylonites (Figure 4.1A). Albite porphyroclasts are tabular in shape and commonly show igneous textures such as oscillatory zoning or Carlsbad or albite twinning. Albite porphyroclasts rarely show sweeping undulose extinction or deformation twinning. Orthoclase porphyroclasts are not as abundant as albite porphyroclasts, and form somewhat tabular grains. Both types of porphyroclasts are microfractured, and many porphyroclasts are fragmented and offset along the microfractures. Rare fine-grained orthoclase and albite

grains (50-100  $\mu\text{m}$ ) are restricted to the rims of grains or along microfractures within the porphyroclasts, and these grains have irregular and lobate grain boundaries. Individual lobes are  $<5 \mu\text{m}$  in diameter (Figure 4.1A). Many of the fine-grained orthoclase and albite grains exhibit irregular and patchy undulatory extinction (Figure 4.1A). The microfractured orthoclase and albite porphyroclasts are consistent with microstructures suggestive of cataclasis, and the microstructures of the fine-grained orthoclase and albite grains are consistent with those suggesting the onset of BLG recrystallization.

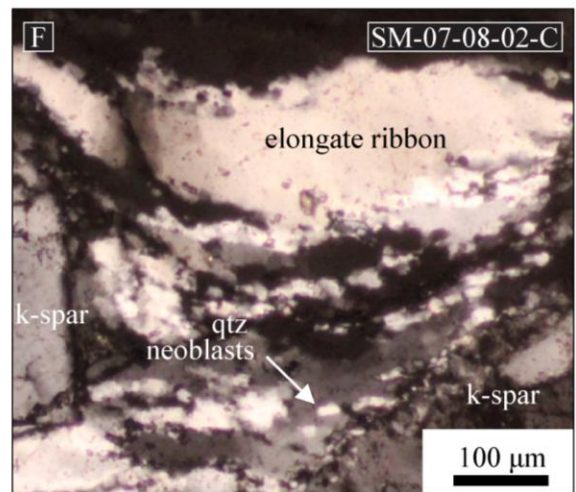
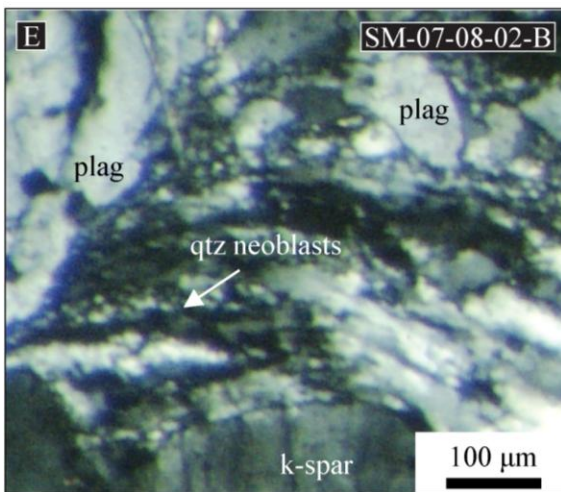
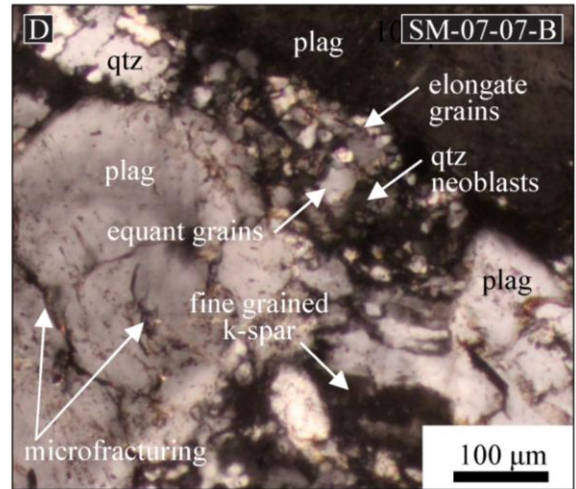
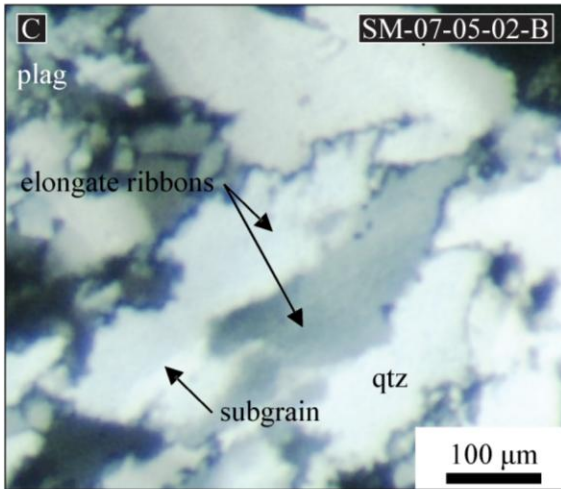
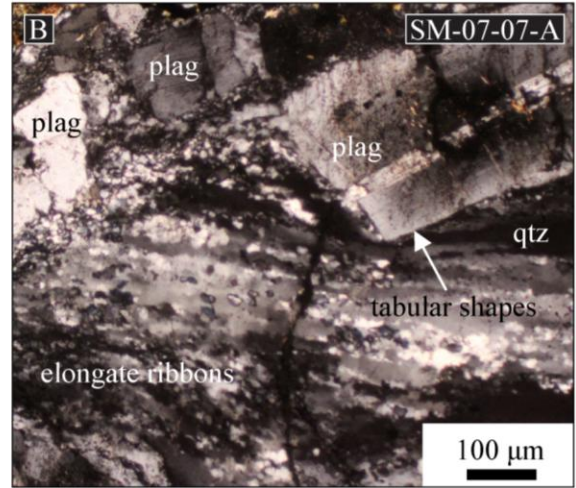
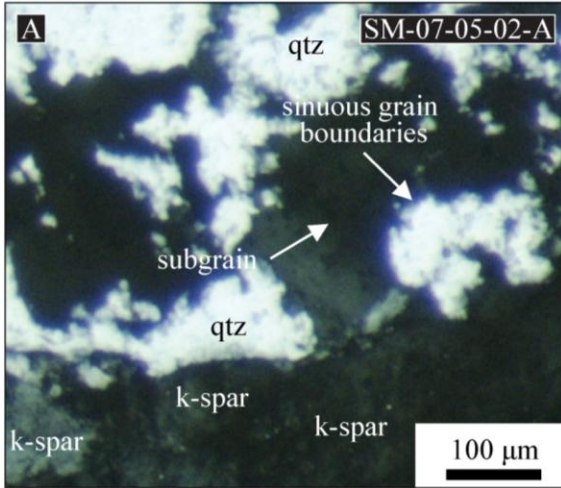


**Figure 4.1** Photomicrographs of quartz, orthoclase, and albite microstructures showing a range of deformation microstructures, corresponding to microstructural Types I and II. **A.** Type I microstructures in which quartz grain boundaries and grain shapes are lobate and irregular. Large quartz grains exhibit limited subgrain development near both the centers and boundaries of host grains. **B.** Type II microstructures in which quartz grains are predominately arranged as elongate ribbon-like structures (~3:1 aspect ratios). The large plagioclase (plag) grain has tabular grain boundaries and exhibits deformation twins that nucleate along grain boundaries. **C.** Type II microstructures in which quartz grains are predominately arranged as elongate ribbon-like structures. Many quartz grains exhibit extensive subgrain development, which produced a core and mantle structure of subgrains along the grain boundaries of the host grain. **D.** Type II microstructures in which quartz grains are predominately fine-grained and consist of both slightly elongate grains (~2:1 aspect ratio) and small equant grains. Both orthoclase (k-spar) and plagioclase grains exhibit microfracturing. Many orthoclase grains exhibit bulging grain boundaries that are suggestive of dynamic recrystallization. **E.** Type II microstructures in which quartz grains form elongate ribbon-like structures, where the elongation is oblique to the macroscopic foliation and is deflected around feldspar porphyroclasts. **F.** Type II microstructures in which recrystallized quartz grain sizes dramatically decrease and grain shapes become increasingly more equant, with increasing proximity to porphyroclasts.

### ***Type II***

Type II mylonites are characterized by quartz grains that are predominately arranged as elongate ribbons or flattened ribbon-like structures with an aspect ratio of ~3:1. Ribbon-like structures have an elongation parallel to the macroscopic foliation (Figure 4.1B), however within close proximities to feldspar porphyroclasts the elongation is oblique to the macroscopic foliation, and is deflected around the porphyroclasts (Figure 4.1C). Many grains exhibit subgrain development along both the centers and rims of the grains. Grains with extensive subgrain development along the rims of the grain exhibit a core and mantle structure (Figure 4.1C). Recrystallized grains mostly form along grain boundaries where recrystallized grain sizes (20-40  $\mu\text{m}$ ) are similar to subgrain grain sizes (Figure 4.1C). Many original quartz grains exhibit a sweeping undulatory extinction, whereas others exhibit deformation lamellae (Figure 4.1C). Quartz microstructures are consistent with microstructures indicative of SGR recrystallization.

Orthoclase and albite grains form large porphyroclasts (~400  $\mu\text{m}$ ) within the mylonites (Figure 4.1B, D, E, and F). Albite porphyroclasts are tabular in shape and commonly show igneous textures such as oscillatory zoning or Carlsbad or albite twinning, and rarely show sweeping undulose extinction or deformation twinning. Orthoclase porphyroclasts are not as abundant as albite porphyroclasts, and form somewhat tabular grains. Both types of porphyroclasts are microfractured, and many porphyroclasts are fragmented and offset along the microfractures (Figure 4.1D). The microfractures are commonly healed with potassium feldspar and quartz. Rare fine-grained orthoclase and albite grains (20-40  $\mu\text{m}$ ) are restricted to the rims of grains or along microfractures within the porphyroclasts, and these grains have irregular and lobate grain boundaries where individual lobes are <5  $\mu\text{m}$  in diameter (Figure 4.1D). Many fine-grained orthoclase and albite grains exhibit irregular and patchy undulatory extinction (Figure 4.1D). The microfractured orthoclase and albite porphyroclasts are consistent with microstructures suggestive of cataclasis, and the fine-grained orthoclase and albite grain shapes are consistent with microstructures suggestive of the onset of BLG recrystallization

#### ***EBSD Data from Type I Fabrics***

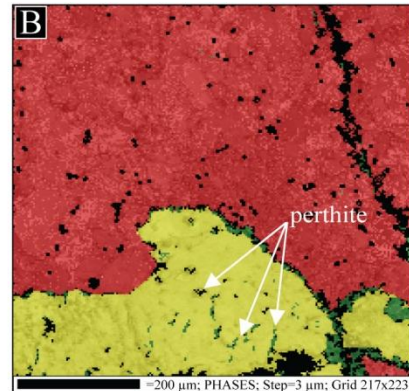
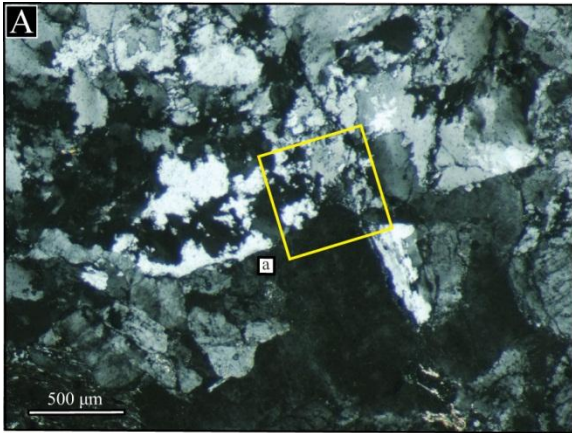
EBSD data were collected from an area displaying Type I fabric characteristics within sample SM-07-05-02 (Figure 4.2A). The region selected for EBSD analysis is dominated by quartz, but also contains minor potassium feldspar and rare plagioclase, based on element abundance measured by EDS (Figure 4.2B). Crystallographic orientation data reveal that the quartz forms an aggregate of recrystallized grains, whereas orthoclase and albite comprise few grains (Figure 4.2C). The quality of the

EBSD pattern data from which crystallographic orientation data are interpreted is estimated by a band contrast image (Figure 4.2D). In the band contrast image, brighter greyscale colors correspond to high quality patterns, and black corresponds to low quality patterns and is most commonly associated with grain boundaries or surface damage.

The quartz grain boundaries and grain shapes are consistent with the GBM dynamic recrystallization regime interpreted from the microstructures in thin section. In the center left part of the map, quartz grain shapes are sinuous and irregular; many large grains (100-200  $\mu\text{m}$ ) have lobate grain boundaries where an individual lobe is  $\sim 30\text{-}50$   $\mu\text{m}$  in diameter (Figure 4.2C). These grain shapes are consistent with microstructures indicative of GBM dynamic recrystallization. Many of these grains are mapped with green and blue colors, indicating a similar crystallographic orientation of the grains (Figure 4.2C). Within the large, lobate grains, there are subgrain boundaries both near the centers and rims of the grains. In some of the largest grains in the map, the internal subgrain boundaries of the lobate grains also mark slight color changes within the grain, and these color change boundaries are commonly oriented parallel to a line extending from the top-left to the bottom-right corners of the map. There are few subgrain-sized grains along the boundaries of these larger lobate grains with the internal subgrain development, with the exception of the grains within the center right region of the map. The few relict large lobate grains contain subgrains that are  $\sim 20$   $\mu\text{m}$ , which are slightly smaller than distinct grains along the grain boundaries. These small distinct grains are slightly elongate and much smaller than the lobate grains, and they are associated with more purple and red mapped colors indicating a greater variety in crystallographic orientation relative to the large lobate grains.

The quartz grains have a similar crystallographic orientation based on the predominance of similar map colors (Figure 4.2C). Coupled with the microstructures that are indicative of dynamic recrystallization, the abundance of quartz grains with green and blue colors indicate the presence of LPO in quartz. The green quartz grains have their  $\langle 1-100 \rangle$  poles to  $m$  prism planes aligned parallel to the macroscopic foliation (X direction), and the deep blue quartz grains have their  $\langle 0-110 \rangle$  poles to  $m$  prism planes aligned parallel to the macroscopic foliation (Figure 4.2D). Rare red quartz grains have their  $c$ -axes  $\langle 0001 \rangle$  aligned parallel to the macroscopic foliation. The  $c$ -axis crystallographic orientation data for all quartz grains are shown in the pole figures (Figure 4.2E). The quartz  $c$ -axes are clustered into a pattern suggestive of a Type I crossed girdle, and this is also consistent with the presence of LPO. There is slight asymmetry in the crossed girdle pattern, suggestive of a component of noncoaxial deformation.

The orthoclase and plagioclase feldspar grains are few in number, and do not show significant evidence for dynamic recrystallization. The large orthoclase grains are somewhat tabular, and do not exhibit internal subgrain development or irregular and lobate grain boundaries suggestive of dynamic recrystallization. However, the two orthoclase grains are rimmed by small equant albite grains ( $<10 \mu\text{m}$ ) with variable map colors (Figure 4.2B and C), suggesting that the small albite grains have dramatically different crystallographic orientations relative to the large orthoclase grain, and that these grains are more sodic in composition than the potassium-rich orthoclase grain. Given the limited number of feldspar grains, there are not enough data points to display in pole figures to interpret the presence or absence of LPO.



Orthoclase Albite Quartz

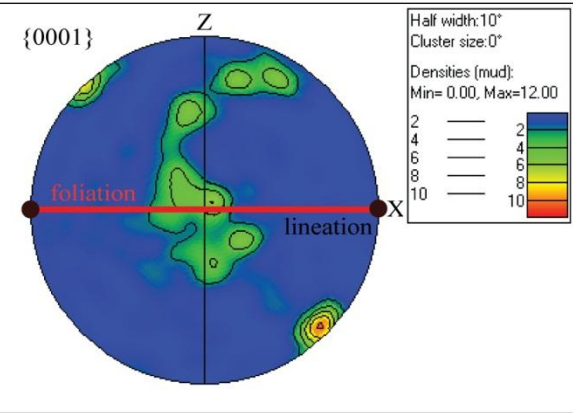
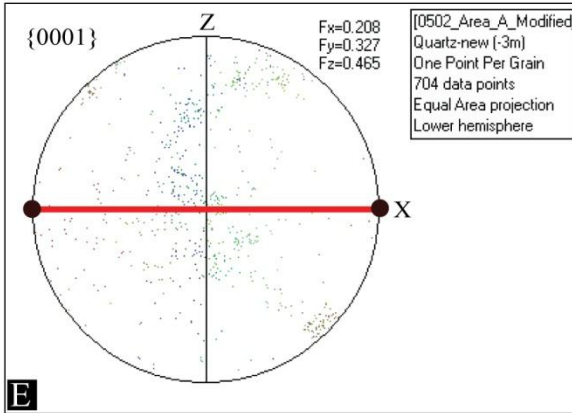
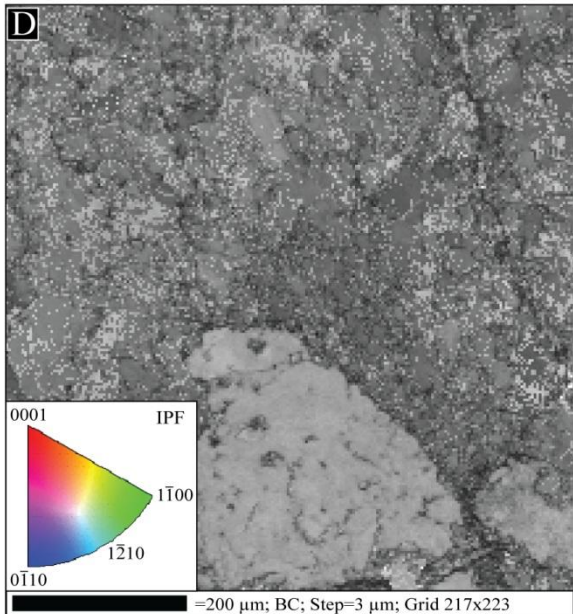
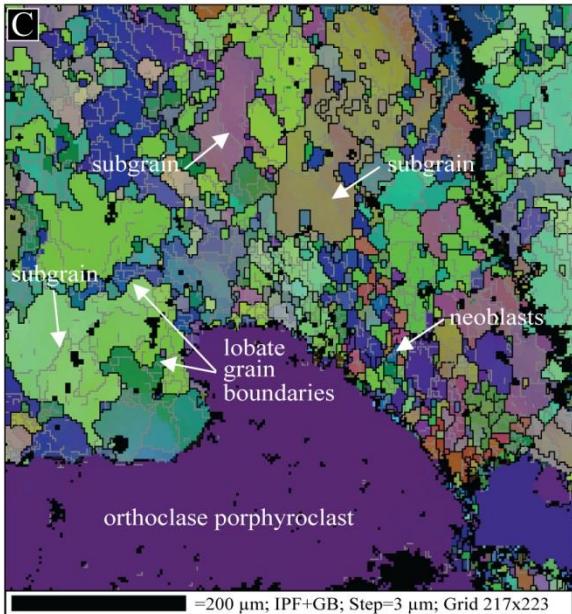


**Figure 4.2** Location of EBSD beam map and EBSD results for sample SM-07-05-02, study region A. **A.** Photomicrograph of a micro-scale ductile shear zone; the yellow rectangle corresponds to the area evaluated by EBSD analysis. **B.** Phase map in which orthoclase, albite, and quartz grains were identified. **C.** EBSD beam map from the inset area in A. IPF legend shows crystallographic directions of quartz grains oriented parallel to lineation, or the X-direction. Feldspar grain colors correspond to different Euler angle orientations. **D.** Band contrast map, used as a proxy for pattern quality. Bright colors correspond to high quality patterns, and dark color corresponds to low quality patterns. **E.** Quartz *c*-axis pole figures. Pole figures are lower hemisphere equal area plots where the macroscopic foliation is parallel to X and the stretching lineation is contained within the foliation and intersects the primitive circle. The X direction and the Y direction represent the finite strain axes of lengthening (X) and shortening (Z), respectively. Recrystallized quartz grains form an interconnected fabric around feldspar grains. Quartz grain boundaries and grain shapes are lobate and irregular, which are consistent with GBM dynamic recrystallization. Orthoclase and albite grains are few in number and consist of large-tabular grains that lack microstructural development suggestive of dynamic recrystallization. Orthoclase porphyroclasts exhibit brittle microfracturing and perthite exsolution along microfractures and grain boundaries.

#### ***EBSD Data from Type II Fabrics***

EBSD data were collected from an area displaying Type II fabric characteristics within sample SM-07-05-02 (Figure 4.3A). The region selected for EBSD analysis is dominated by quartz, but also contains minor plagioclase and rare potassium feldspar, based on elemental abundance measured by EDS (Figure 4.3B). Crystallographic orientation data reveal that the quartz forms an aggregate of recrystallized grains, whereas albite and orthoclase comprise few grains (Figure 4.3C).

The quartz-grain boundaries and grain shapes are consistent with the SGR dynamic recrystallization regime interpreted from the microstructures in thin section. In the bottom-center part of the map, quartz grain shapes are predominately arranged as large (150-250  $\mu\text{m}$ ) elongate ribbons or flattened ribbon-like structures with aspect ratios of  $\sim 3:1$  (Figure 4.3C). These elongate grain shapes and the presence of color gradations parallel to the elongation that are indicative of subgrain boundaries are both consistent with microstructures indicative of SGR dynamic recrystallization. Many large grains

have subgrain boundaries along both the centers and rims of the grains. The color change boundaries are commonly oriented parallel to a line extending from the top-left to the bottom-right corners of the map. Many of these subgrains are mapped with green and brown colors, indicating a similar crystallographic orientation of the subgrains.

The quartz grains have a similar crystallographic orientation based on the predominance of similar map colors (Figure 4.3C). Coupled with the microstructures that are indicative of dynamic recrystallization, the abundance of quartz grains with green and brown colors indicate the presence of LPO in quartz. The green quartz grains have their  $\langle 1-100 \rangle$  poles to  $m$  prism planes aligned parallel to the macroscopic foliation (X direction), and the purple quartz grains have their  $\langle 0-110 \rangle$  poles to  $m$  prism planes aligned parallel to the macroscopic foliation (Figure 4.3D). The  $c$ -axis crystallographic orientation data for all quartz grains are shown in the pole figures (Figure 4.3E). The quartz  $c$ -axes are clustered into a pattern suggestive of two  $c$ -axis maxima near the primitive circle, located about  $45^\circ$  clockwise from the macroscopic foliation direction (x-direction). This pattern is also consistent with the presence of LPO and suggestive of noncoaxial deformation.

The plagioclase and orthoclase feldspar grains are few in number, and neither show evidence for dynamic recrystallization. The large albite grains are somewhat tabular, and do not exhibit internal subgrain development or other microstructures suggestive of dynamic recrystallization (Figure 4.3B and C). The two large albite grains are characterized by solid green and bluish-purple colors separated by a boundary oriented parallel to a line connecting the upper-left to bottom-right corners of the map. These intra-grain color change boundaries are also parallel to the albite twinning shown

within the albite grain in the upper-right corner of the band contrast map (Figure 4.3). The color changes appear to be consistent with primary igneous Carlsbad twinning. Given the limited number of albite and orthoclase grains, there are not enough data to interpret any information about the presence of absence of LPO.

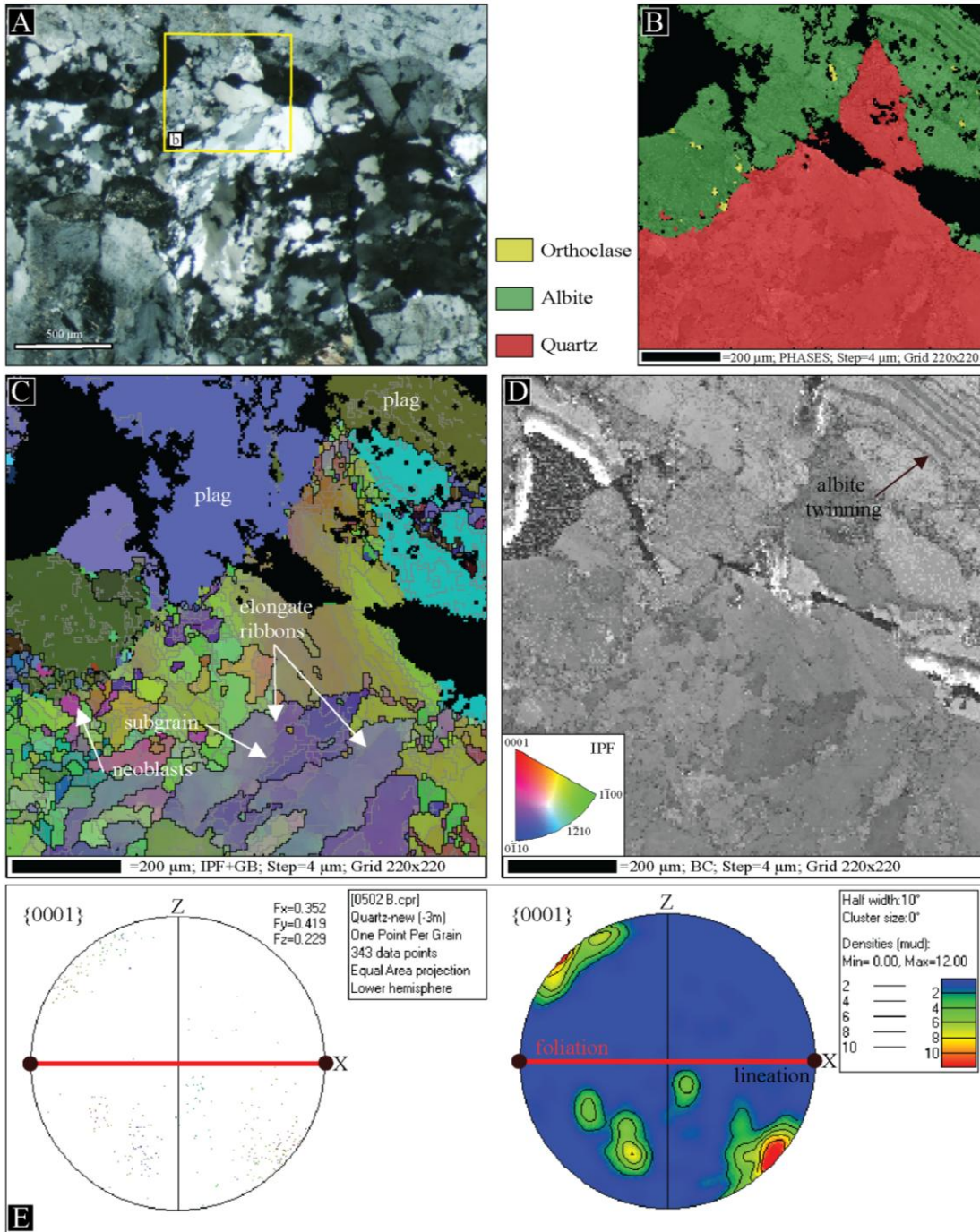


**Figure 4.3** Location of EBSD beam map and EBSD results for sample SM-07-05-02, study region B. Figure components (A:E) are explained in Figure 4.2. Quartz grain shapes are predominately arranged as elongate ribbon-like structures with aspect ratios of ~3:1. Elongate grains exhibit color gradations parallel to elongation (X-axis) that are indicative of subgrain development. Subgrains are located along both the center and rims of host grains. Quartz-grain boundaries and grain shapes are consistent with the SGR dynamic recrystallization. Plagioclase grains are few in number, and are predominately arranged as large-tabular grains that exhibit primary igneous fabrics (e.g. albite twinning).

EBSD data were collected from three areas displaying Type II fabric characteristics within sample SM-07-07; sample locations are discussed later. The first area contains elongate quartz ribbons or flattened ribbon-like structures that surround a large albite porphyroclast with tabular grain boundaries. The second and third areas contain similar microstructures, since the third area is a portion of the second area that was sampled at higher detail (smaller EBSD step size). These areas contain both quartz grains with elongate quartz ribbon-like structures and others with sinuous grain boundaries, surrounded by albite porphyroclasts and a matrix of fine-grained orthoclase feldspar.

### *Area 1*

The quartz grain boundaries and grain shapes from the first area are consistent with the SGR dynamic recrystallization regime interpreted from the microstructures in thin section. In the bottom-right and bottom-center parts of the map, quartz grain shapes are predominately arranged as large (200-300  $\mu\text{m}$ ) elongate ribbons or flattened ribbon-like structures with aspect ratios of ~3 to 4:1 (Figure 4.4B). These grain shapes are consistent with microstructures indicative of SGR dynamic recrystallization. Many large grains have subgrain boundaries along both the centers and rims of the grains. Many of these subgrains are mapped with green and blue colors, indicating a similar

crystallographic orientation of the subgrains. The color change boundaries are commonly oriented subparallel to the horizontal bottom edge of the map. Quartz grains within close proximity to the albite porphyroclast have significantly smaller grain sizes ( $<10\ \mu\text{m}$ ) relative to the quartz ribbons. These small distinct grains are more equant and much smaller than adjacent subgrains within quartz ribbons, and they are associated with more purple and red mapped colors indicating a greater variety in crystallographic orientation relative to the large ribbon-like grains.

The quartz ribbon grains and associated subgrains have a similar crystallographic orientation based on the predominance of similar map colors. Coupled with the microstructures that are indicative of dynamic recrystallization, the abundance of quartz grains with green and blue colors indicate the presence of LPO in quartz. The green quartz grains have their  $\langle 1-100 \rangle$  poles to  $m$  prism planes aligned parallel to the macroscopic foliation (X direction), and the light blue quartz grains have their  $\langle 1-210 \rangle$  poles to  $m$  prism planes aligned parallel to the macroscopic foliation (Figure 4.4B). Rare red quartz grains have their  $c$ -axes  $\langle 0001 \rangle$  aligned parallel to the macroscopic foliation. The  $c$ -axis crystallographic orientation data for all quartz grains are shown in the pole figures (Figure 4.4E). The quartz  $c$ -axes are clustered into a pattern suggestive of a single  $c$ -axis maximum near the Y finite strain axis, and it is slightly elongate parallel to the Z finite strain axis of shortening. This pattern is also consistent with the presence of LPO.

The plagioclase and orthoclase feldspar grains are few in number, and do not show significant evidence for dynamic recrystallization. The large albite grains are somewhat tabular, and do not exhibit internal subgrain development or other microstructures suggestive of dynamic recrystallization (Figure 4.4C and D). However,

the large albite grain has albite twins with tapered edges, nucleated along grain boundaries, which are consistent with deformation twins (Figure 4.4C). Many albite porphyroclasts in the top-center parts of the map are rimmed by small equant orthoclase grains (<10  $\mu\text{m}$ ) with variable map colors (Figure 4.4B and D), suggesting that the small orthoclase grains have dramatically different crystallographic orientations relative to the large albite grains, and that these grains are more potassium-rich in composition than the sodic albite grain. Given the limited number of feldspar grains, there are not enough data points to display in pole figures to interpret the presence or absence of LPO.

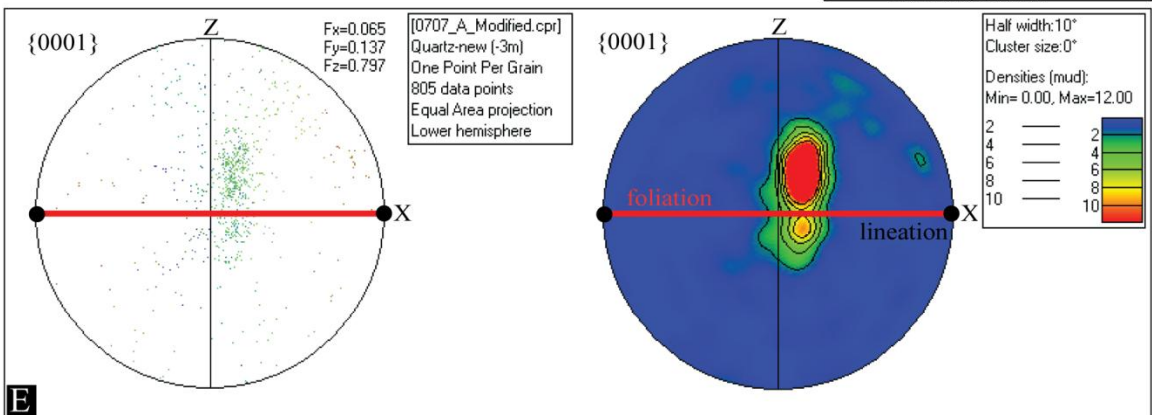
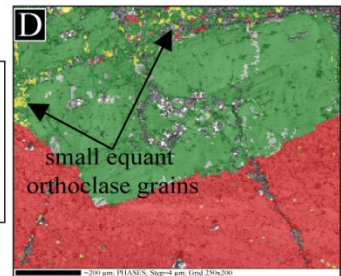
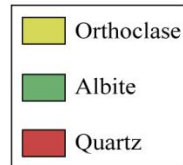
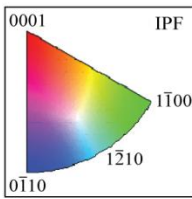
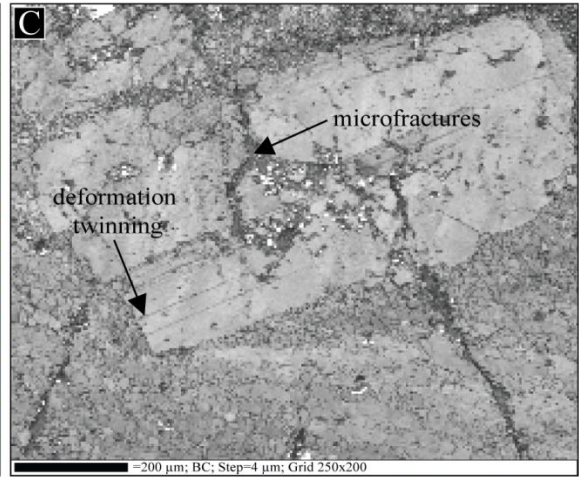
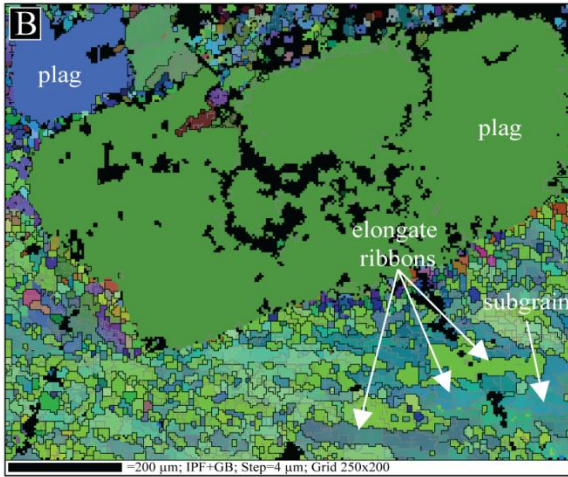
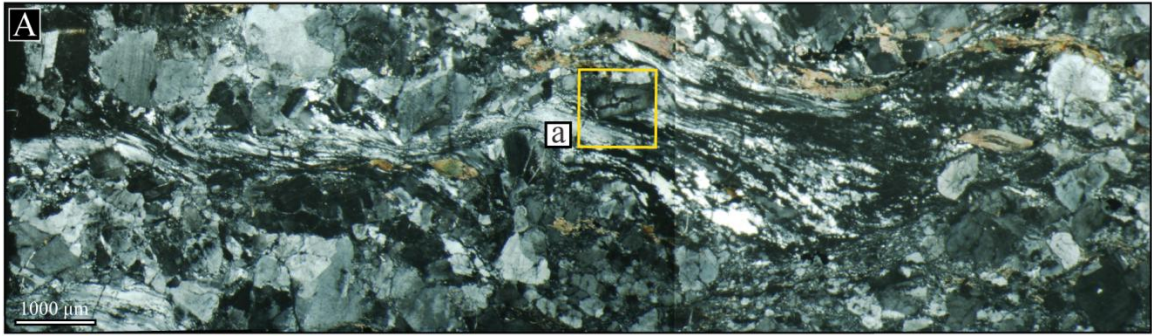


**Figure 4.4** Location of EBSD beam map and EBSD results for sample SM-07-07, study region A. Figure components (A:E) are explained in Figure 4.2. Quartz grain shapes are predominately arranged as elongate ribbon-like structures with aspect ratios of ~3:1. Quartz-grain boundaries and grain shapes are consistent with the SGR dynamic recrystallization. Quartz grains within close proximity to porphyroclasts have significantly smaller grain sizes and more equant grain shapes, with respect to the elongate ribbon-like quartz grains. Plagioclase and orthoclase grains are few in number, and consist of large-tabular grains. The large plagioclase grain in the center of the figure exhibits deformation twinning that nucleates from grain boundaries. Plagioclase grains are rimmed by small equant orthoclase grains.

## *Area 2*

The quartz grain boundaries and grain shapes from the second area of sample SM-07-07 (Figure 4.5A) are inconsistent with the diagnostic microstructures of any dynamic recrystallization regime. The quartz forms fine-grained (~20-25  $\mu\text{m}$ ) aggregates of equant-sized grains with rare, slightly elongate (2:1 aspect ratio) grains (Figure 4.5C). These dominantly equant grain shapes are inconsistent with the microstructures of SGR dynamic recrystallization, and there are few fine-grained (<5  $\mu\text{m}$ ) bulging grain boundaries consistent with BLG dynamic recrystallization. The aggregate of grains may be most consistent with GBM recrystallization given their equant sizes and rare lobate and irregular grain boundaries, but most grains do not show these diagnostic microstructures indicative of this dynamic recrystallization mechanism. It may be that the microstructures were developed through the contributions of multiple dynamic recrystallization mechanisms. Regardless of dynamic recrystallization mechanism(s) that contributed to the development of the recrystallized microstructure, many of these grains are mapped with green and reddish colors indicating a similar crystallographic orientation of the grains (Figure 4.5C).

The quartz grains have a similar crystallographic orientation based on the predominance of similar map colors. Coupled with the microstructures that are indicative

of some variety of dynamic recrystallization, the abundance of quartz grains with green and reddish colors indicate the presence of LPO in quartz. The green quartz grains have their  $\langle 1-100 \rangle$  poles to  $m$  prism planes aligned parallel to the macroscopic foliation (X direction), and the red quartz grains have their  $c$ -axes  $\langle 0001 \rangle$  aligned parallel to the macroscopic foliation (Figure 4.5C). The  $c$ -axis crystallographic orientation data for all quartz grains are shown in the pole figures (Figure 4.5E). The quartz  $c$ -axes are modestly clustered into a pattern suggestive of a diffuse  $c$ -axis maximum near the Y finite strain axis. This pattern is also consistent with the presence of LPO.

The plagioclase grain boundaries and grain shapes are consistent with primary igneous fabrics interpreted from the microstructures in thin section. In the center part of the map, the albite porphyroblast grain is tabular in shape and exhibits oscillatory zoning (Figure 4.5A). Albite grains do not exhibit internal subgrain development or irregular and lobate grain boundaries suggestive of extensive dynamic recrystallization (Figure 4.5C). However, there are rare deformation twins present in the albite porphyroblast, indicating the onset of limited crystal plasticity (Figure 4.5D).

Fine-grained orthoclase grains in the top-left, bottom-center, and bottom-right parts of the map have grain boundaries and grain shapes consistent with the BLG dynamic recrystallization regime interpreted from the microstructures in thin section (Figure 4.5C). Orthoclase grain shapes are sinuous and irregular; many grains (20-40  $\mu\text{m}$ ) have lobate grain boundaries where an individual lobe is  $<5 \mu\text{m}$  in diameter (Figure 4.5C). These grain shapes are consistent with microstructures indicative of BLG dynamic recrystallization. Many of these grains are mapped with purple, blue, and green colors, indicating a similar crystallographic orientation of the grains (Figure 4.5C).

The orthoclase grains have a similar crystallographic orientation based on the predominance of similar map colors. Coupled with the microstructures that are indicative of modest dynamic recrystallization, the abundance of orthoclase grains with blue and brown colors indicates a modest presence of a LPO in orthoclase. The crystallographic  $a$ ,  $b$ , and  $c$ -plane and corresponding direction orientation data for all orthoclase grains are shown in the pole figures (Figure 4.6). The orthoclase poles to the  $b$ -planes show a slight maxima parallel to the  $Z$  finite strain axis in the  $\{010\}$  pole figure. There is also a slight concentration of  $\langle 001 \rangle$  axes parallel to the  $X$  finite strain direction (lineation direction). This pattern is also consistent with the presence of a weak to modest LPO.

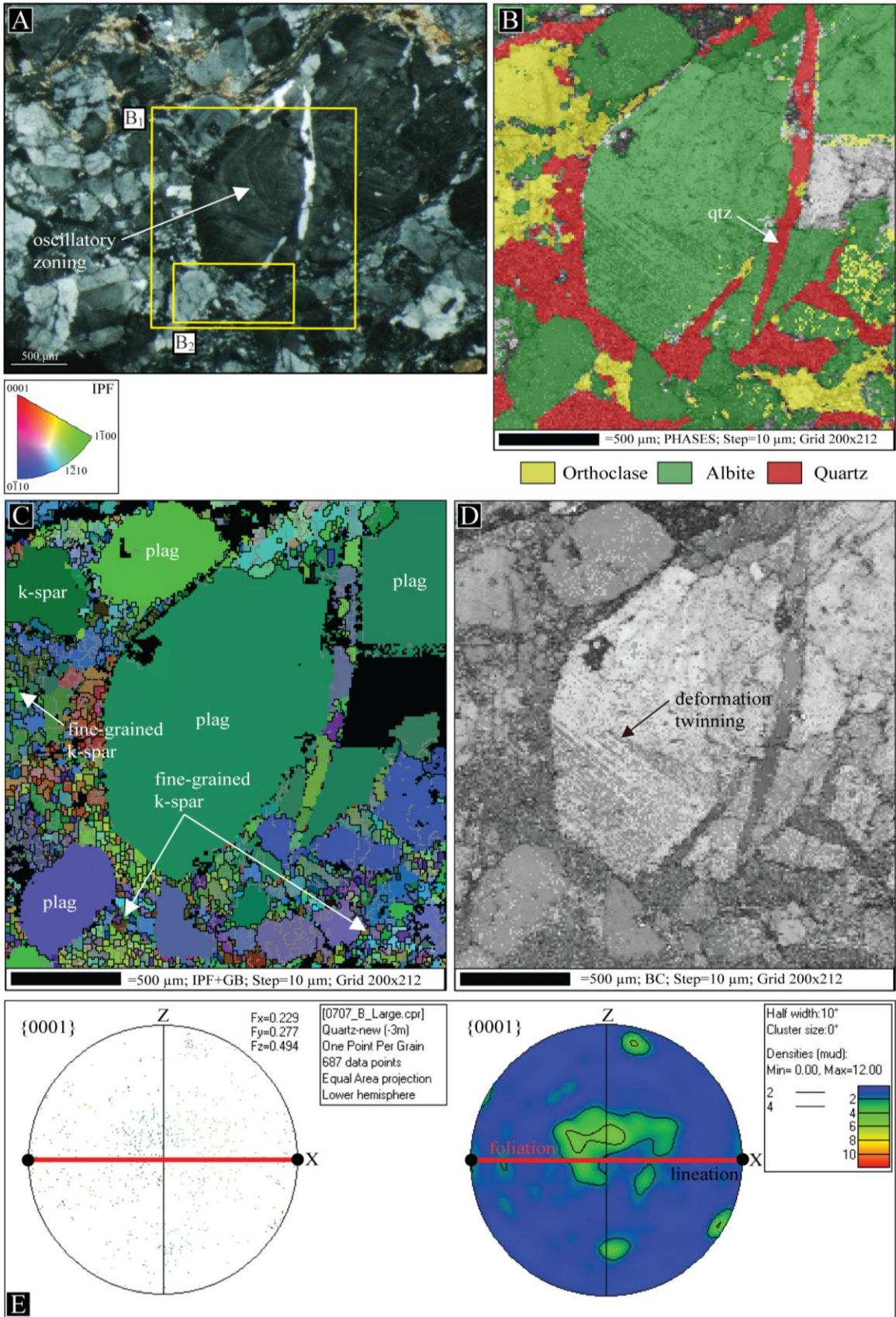


**Figure 4.5** Location of EBSD beam map and EBSD results for sample SM-07-07, study region B<sub>1</sub>. Figure components (A:E) are explained in Figure 4.2. Quartz grain shapes are predominately equant, with few elongate (2:1 aspect ratio) grains, and few grains with bulging grain boundaries (<5 μm). Quartz grain boundaries and grain shapes are inconsistent with the diagnostic microstructures of any one dynamic recrystallization regime. Regardless of recrystallization regime, many quartz grains have similar IPF colors, which is indicative of similar crystallographic orientations. Plagioclase grains are predominately arranged as large-tabular grains that exhibit primary igneous fabrics (e.g. oscillatory zoning). The large plagioclase porphyroclast exhibits deformation twins that nucleate along grain boundaries. Fine-grained orthoclase grains have sinuous and irregular grain boundaries; orthoclase grain boundaries and grain shapes are consistent with BLG dynamic recrystallization.

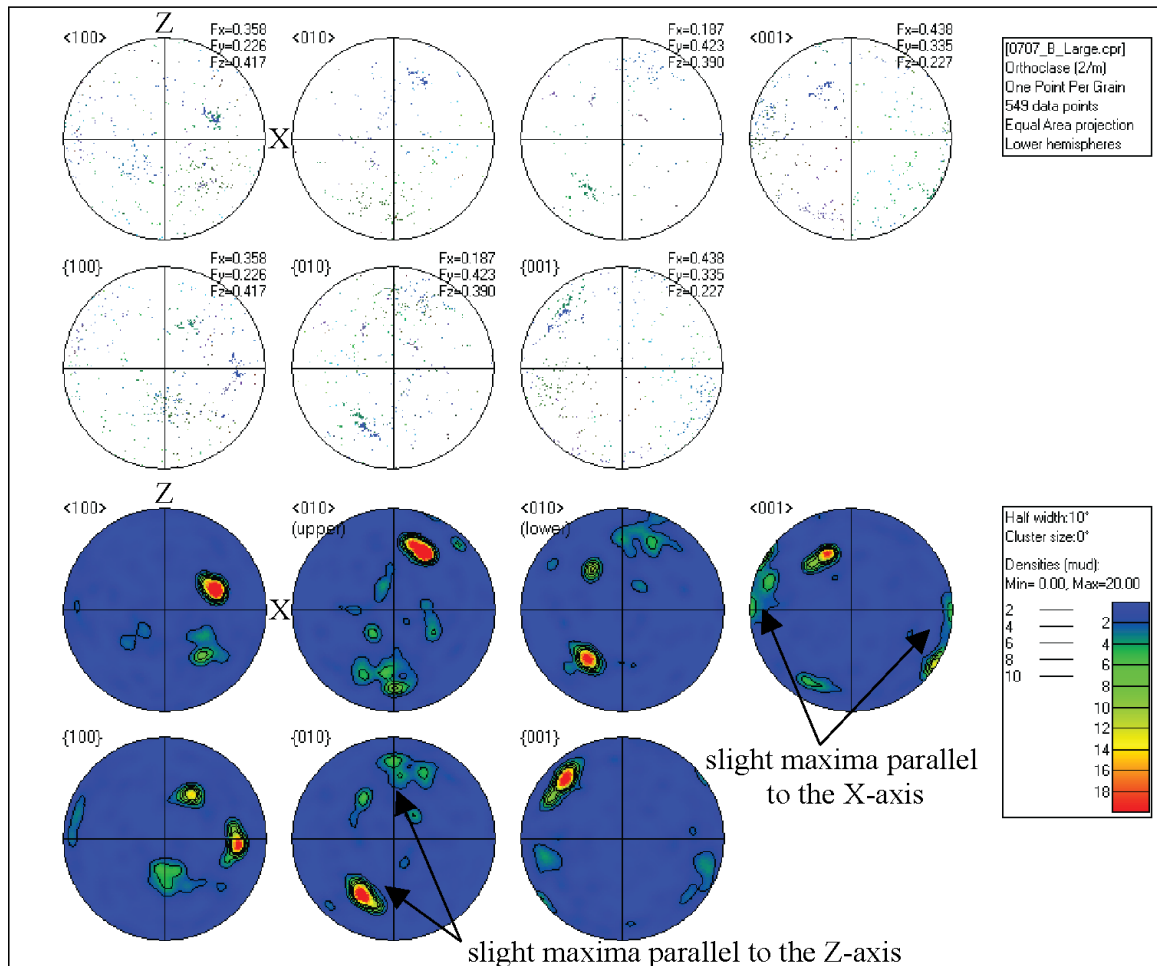


**Figure 4.6** Orthoclase pole figures for sample SM-07-07, study region B<sub>1</sub>. Lower hemisphere feldspar pole figures include: *a*-direction  $\langle 100 \rangle$ , *b*-direction  $\langle 010 \rangle$  (upper and lower hemisphere), *c*-direction  $\langle 001 \rangle$ , *a*-plane  $\{100\}$ , *b*-plane  $\{010\}$ , and *c*-plane  $\{001\}$  plots. Orthoclase crystallographic orientations exhibit a slight maxima of the poles to the *b*-planes  $\{010\}$  parallel to the Z-finite strain axis, and a slight maxima of *c*-axes  $\langle 001 \rangle$  parallel to the X finite strain direction.

### **Area 3**

The quartz grain boundaries and grain shapes from the third area are most consistent with the SGR dynamic recrystallization regime interpreted from the microstructures in thin section. In the center-right part of the map, quartz grain shapes are predominately arranged as fine-grained ( $\sim 20\text{-}25\ \mu\text{m}$ ) elongate ribbon-like structures with aspect ratios of  $\sim 2:1$  (Figure 4.7C). These grain shapes are consistent with the elongate grains indicative of SGR dynamic recrystallization. Many of these grains are mapped with green and purple colors, indicating a similar crystallographic orientation of the grains (Figure 4.7C). However, in the center part of the map, most of the quartz grains are fine-grained ( $< 20\ \mu\text{m}$ ) and roughly equant in shape, with the larger grains among them showing sinuous grain boundaries. These grain shapes are similar to those observed in the second area from sample SM-07-07 (Figure 4.5), and are somewhat consistent with microstructures indicative of GBM recrystallization. Many of these grains are mapped with green colors, indicating a self-similar crystallographic orientation, and an orientation similar to the elongate grains in the center-right part of the beam map (Figure 4.7C).

The quartz grains have a similar crystallographic orientation based on the predominance of similar map colors. Coupled with the microstructures that are indicative of SGR and a component of GBM dynamic recrystallization, the abundance of quartz grains with green and purple colors indicate the presence of LPO in quartz. The green quartz grains have their  $\langle 1\text{-}100 \rangle$  poles to *m* prism planes aligned parallel to the

macroscopic foliation (X direction) and the purple quartz grains have their  $\langle 0-110 \rangle$  poles to  $m$  prism planes aligned subparallel to the macroscopic foliation (Figure 4.7C). The  $c$ -axis crystallographic orientation data for all quartz grains are shown in the pole figures (Figure 4.7E). The quartz  $c$ -axes are modestly clustered into a pattern suggestive of a diffuse  $c$ -axis maximum near the Y finite strain axis. This pattern is also consistent with the presence of LPO.

The plagioclase grain boundaries and grain shapes are consistent with primary igneous fabrics interpreted from the microstructures in thin section. In the bottom-left, bottom-right, and top-right parts of the map, the albite porphyroclasts are tabular in shape and the grain in the top-right part of the map exhibits oscillatory zoning (Figure 4.7A and C). Albite grains do not exhibit internal subgrain development or irregular and lobate grain boundaries suggestive of dynamic recrystallization (Figure 4.7C).

Fine-grained orthoclase grains in the bottom-center part of the map have grain boundaries and grain shapes consistent with the BLG dynamic recrystallization regime interpreted from the microstructures in thin section (Figure 4.7C). Orthoclase grain shapes are sinuous and irregular; many fine-grained grains (20-40  $\mu\text{m}$ ) have lobate grain boundaries where an individual lobe is  $<5 \mu\text{m}$  in diameter (Figure 4.7C). These grain shapes are consistent with microstructures indicative of BLG dynamic recrystallization. Many of these grains are mapped with purple and brown colors, indicating a similar crystallographic orientation of the grains (Figure 4.7C).

The orthoclase grains have a similar crystallographic orientation based on the predominance of similar map colors. Coupled with the microstructures that are indicative of modest dynamic recrystallization, the abundance of orthoclase grains with purple and

brown colors indicates the presence of a LPO in orthoclase. The crystallographic orientation data for all orthoclase grains are shown in the pole figures (Figure 4.8). In contrast to the presence of LPO indicated by the EBSD map colors, the orthoclase crystallographic data in the pole figures exhibit considerable scatter, and show a random crystallographic orientation of the grains. The pole figures show that fewer than 200 orthoclase grains were measured from this third study region of sample SM-07-07, which is a fewer number of orthoclase data points than those collected from the orthoclase grains in the second study region of sample SM-07-07 (Figure 4.8).

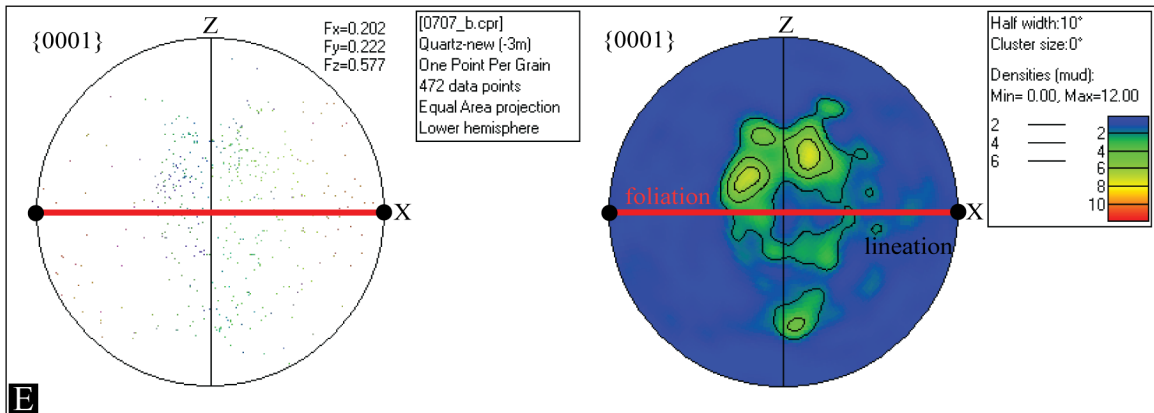
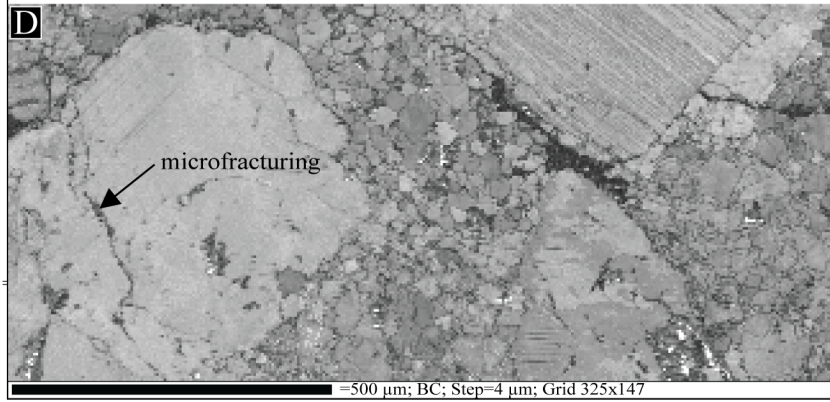
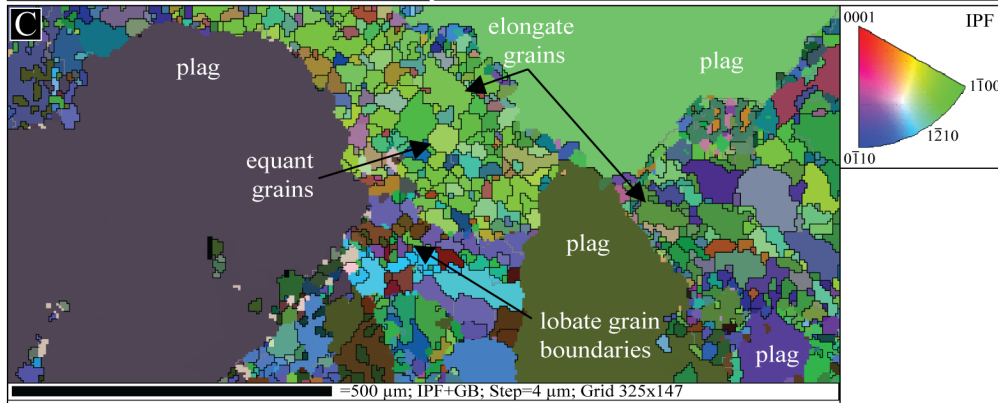
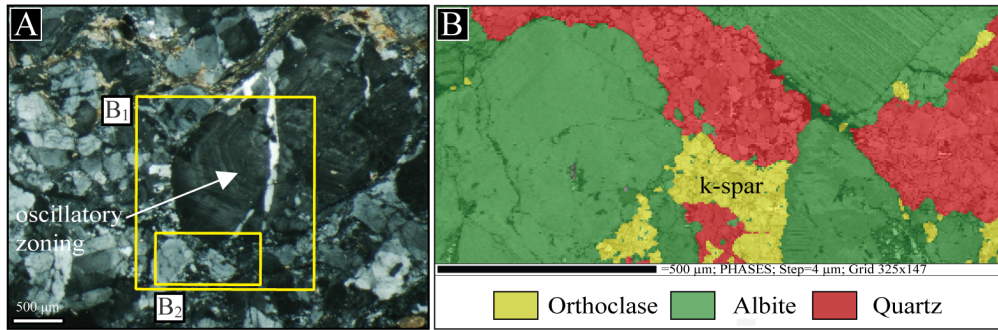


**Figure 4.7** Location of EBSD beam map and EBSD results for sample SM-07-07, study region B<sub>2</sub>. Figure components (A:E) are explained in Figure 4.2. In the center-right part of the map quartz grain shapes are elongate (~2:1 aspect ratio), whereas in the center part of the map quartz grains are roughly equant in shape. Many of the larger equant grains have sinuous grain boundaries. Quartz grain boundaries and grain shapes are predominately consistent with SGR dynamic recrystallization regime. Plagioclase grains are predominately arranged as large-tabular grains that exhibit primary igneous fabrics (e.g. oscillatory zoning). Fine-grained orthoclase grains have sinuous and irregular grain boundaries; orthoclase grain boundaries and grain shapes are consistent with BLG dynamic recrystallization.

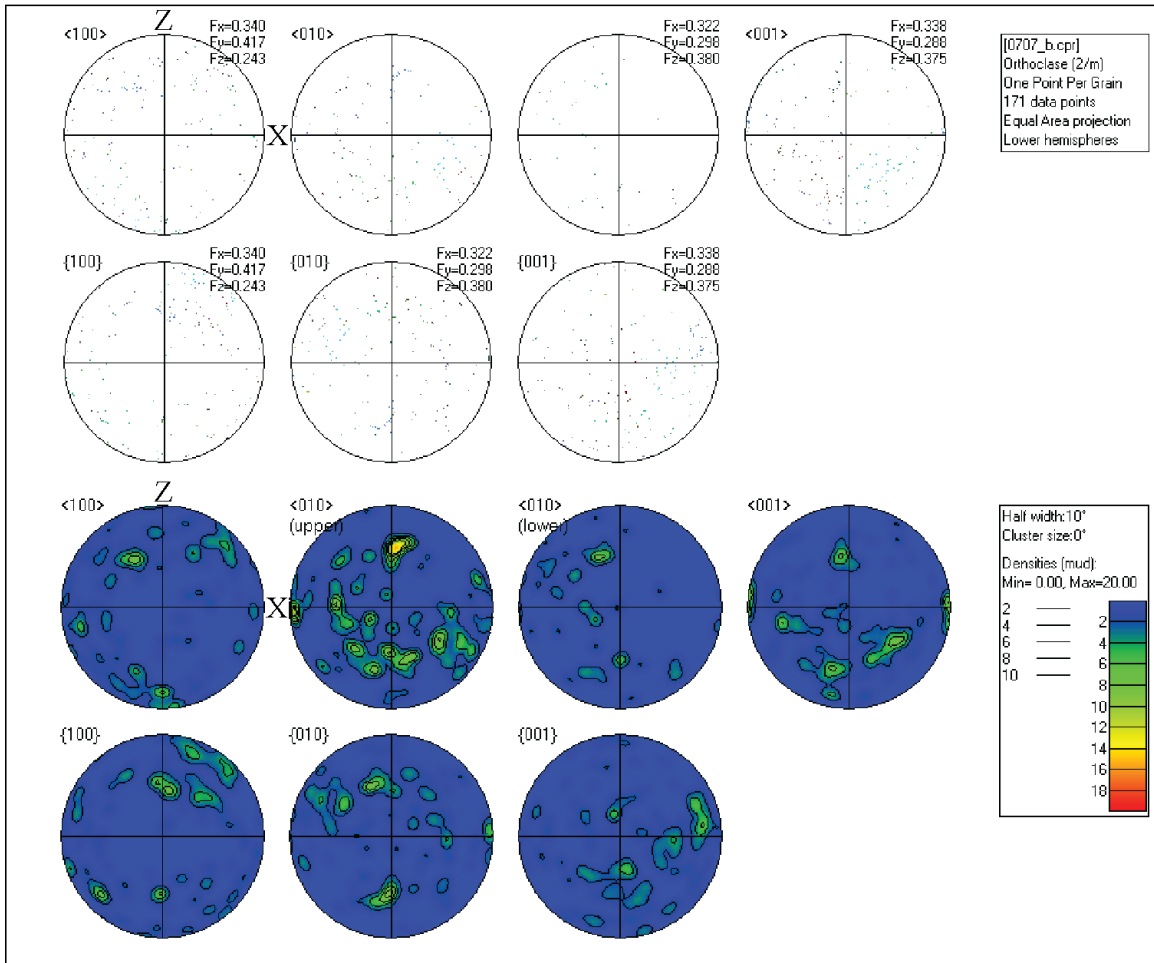


**Figure 4.8** Orthoclase pole figures for sample SM-07-07, study region B<sub>2</sub>. Figure components are explained in Figure 4.6. Orthoclase pole figures exhibit considerable scatter of crystallographic orientations of the grains. The pole figures are composed of 171 crystallographic orientations. Pole figures composed of fewer than 200 data points are considered estimates in this study.

### Modal Abundance of Primary Mineralogy

Proportions of mineral phases for samples used for EBSD analysis were quantified with Channel 5 software. Modal abundances for study areas with high proportions of quartz include: 2-30% albite, 0-25% orthoclase, 50-78% quartz, and <10% accessory minerals (e.g. biotite and oxides), whereas modal abundances for study areas with high proportions of feldspar include: 50-90% albite, 1-17% orthoclase, 1-40% quartz, and <10% accessory minerals (Table 4.1).

Sample	Modal % Quartz	Modal % Orthoclase	Modal % Albite	Others
SM-07-05-02-A	67.2	24.5	2.0	6.3
SM-07-05-02-B	49.5	0.3	33.0	17.2
SM-07-05-02-C	72.6	7.3	4.2	15.9
SM-07-07-A	38.5	1.4	50.3	9.8
SM-07-07-B <sub>1</sub>	17.5	14.7	55.0	12.8
SM-07-07-B <sub>2</sub>	27.0	8.4	64.0	0.6
SM-07-07-C	-	-	-	-
SM-07-08-02-A	1.7	8.0	90.0	0.3
SM-07-08-02-B	18.0	16.6	65.0	0.4
SM-07-08-02-C	78.1	5.8	2.5	13.6

**Table 4.1** Primary modal mineralogy (e.g. quartz, orthoclase, albite, and others) of rock samples. Modal percentages were derived from phases identified by EBSD and EDS analysis. Other phases include: biotite, oxides, and EBSD zero solutions. Modal percentages for study area SM-07-07-C were not quantified due to the lack of EDS data.

## Constraints on Deformation Conditions

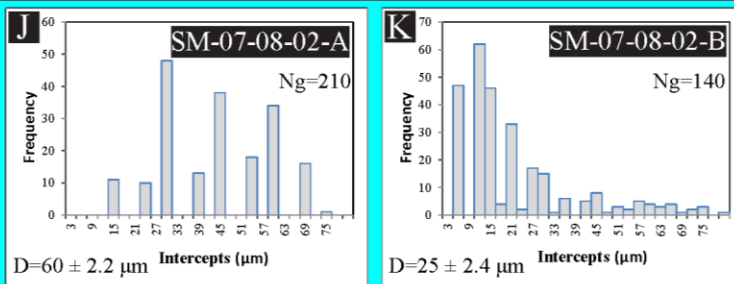
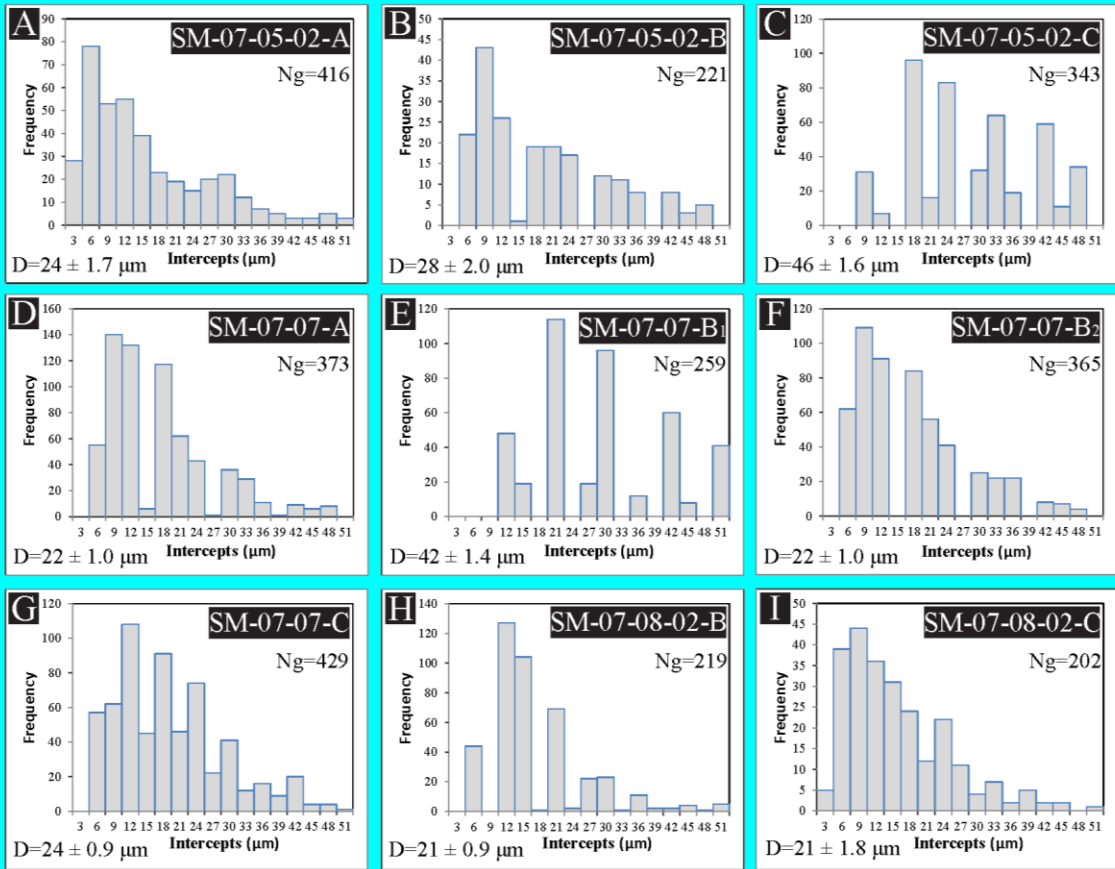
### *Grain Size*

Calculated grain intercept lengths parallel to the X and Z directions have many grains with X:Z aspect ratios ranging from 2:1 to 3:1 (e.g. SM-07-05-02-B and SM-07-07) in regions with well-developed SGR dynamic recrystallization microstructures. The standard deviation of grain size for the South Mountain samples is typically ~50-100% of the calculated mean. Intercept lengths for primary modal mineralogy for most study areas have log-normal distributions for the X and Z measured orientations (Figure 4.9). Line

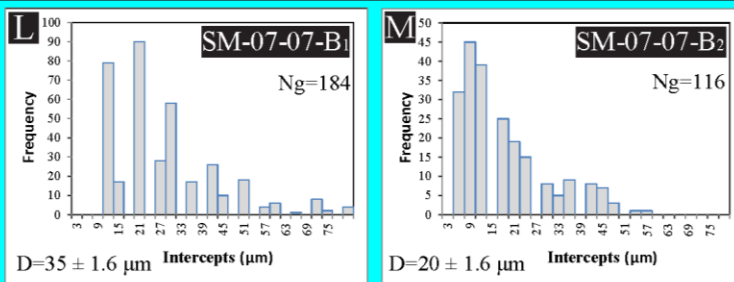
intercept distributions that lack log-normal distributions (Figure 4.9C, E, J) correspond to study areas with large proportions of EBSD misindexing and nonindexing errors.

Quartz grain sizes from study areas with high proportions of quartz range from  $21 \pm 1.8$  to  $46 \pm 1.6$   $\mu\text{m}$  in diameter. Albite grain sizes are significantly larger than adjacent quartz and orthoclase grains, ranging from  $25 \pm 2.4$  to  $60 \pm 2.2$   $\mu\text{m}$  in diameters, whereas orthoclase has the finest grain sizes of the two feldspars, ranging from  $20 \pm 1.6$  to  $35 \pm 1.6$   $\mu\text{m}$  in diameter.

quartz



albite



orthoclase

**Figure 4.9** Line intercept distribution for recrystallized quartz grains (**A:I**), albite porphyroclasts (**J:K**), and orthoclase porphyroclasts (**L:M**). Histogram intercept axes have maximum and minimum values corresponding to the minimum EBSD step size and maximum value that include 99% of the measured intercept lengths.  $D$  = grain size. Bin size = 3  $\mu\text{m}$ .  $N_g$  = number of linear intercepts. Line intercept distributions mostly have log-normal distributions. Line intercept distributions that lack a log-normal distribution (e.g. **C**, **E**, **J**) correspond to study regions with high proportions of EBSD misindexing and nonindexing errors. Grain sizes for study areas with significantly fewer than 200 linear intercepts (e.g. **K**, **M**) are considered estimates in this study.

### *Differential Stress*

The quartz empirical piezometer of Stipp and Tullis (2003) is used in this study to estimate differential stress as a function of recrystallized grain size, since this piezometer is specific to individual dynamic recrystallization mechanisms (i.e. Regimes I and II/III). Using the most robust grain size estimates from highly indexed EBSD maps, the calculated differential stresses for recrystallized quartz in study areas SM-07-05-02, SM-07-07, and SM-07-08-02 are 47-54 MPa, 54-58 MPa, and 59-60 MPa, respectively (Table 4.2). The calculated differential stresses for SMCC samples increases slightly with decreasing structural depth beneath the detachment fault, corresponding to a gradual decrease in recrystallized grain size from samples SM-07-05-02 to SM-07-08-02, or with increasing proximity to the detachment surface.

Sample	D [ $\mu\text{m}$ ]	$N_g$	$\sigma$ [MPa]
SM-07-05-02-A	$24 \pm 1.7$	416	54 (-2.8/+3.2)
SM-07-05-02-B	$28 \pm 2.0$	221	47 (-2.5/+2.9)
*SM-07-05-02-C	$46 \pm 1.6$	343	32 (-0.8/+1.0)
SM-07-07-A	$22 \pm 1.0$	373	58 (-2.0/+2.2)
*SM-07-07-B <sub>1</sub>	$42 \pm 1.4$	259	35 (-0.8/+1.0)
SM-07-07-B <sub>2</sub>	$22 \pm 1.1$	365	58 (-2.1/+2.4)
SM-07-07-C	$24 \pm 0.9$	429	54 (-1.5/+1.7)
SM-07-08-02-A	-	-	-
SM-07-08-02-B	$21 \pm 0.9$	219	59 (-1.9/+2.1)
SM-07-08-02-C	$21 \pm 1.8$	202	60 (-3.8/+4.4)

**Table 4.2** Summary of quartz grain size and stress for the South Mountains mylonites. D=recrystallized grain size,  $N_g$ =number of linear intercepts,  $\sigma$ =differential stress. \*SM-07-05-02-C grain sizes and calculated stresses are estimates due to limited indexing by Channel 5 software. \*SM-07-07-B<sub>1</sub> large step size artificially inflates the calculated recrystallized grain size and calculated differential stresses. Grain size error is calculated for a 95% confidence level.

On a plot of recrystallized grain size versus differential stress, the SMCC samples are tightly clustered along the Stipp and Tullis (2003) piezometric relationship, and are predicted to have Regime III (GBM) dynamic recrystallization microstructures (Figure 4.10). Calculated differential stresses from the Stipp and Tullis (2003) piezometer are slightly lower than predicted by the Twiss (1977) piezometer (Figure 4.10).

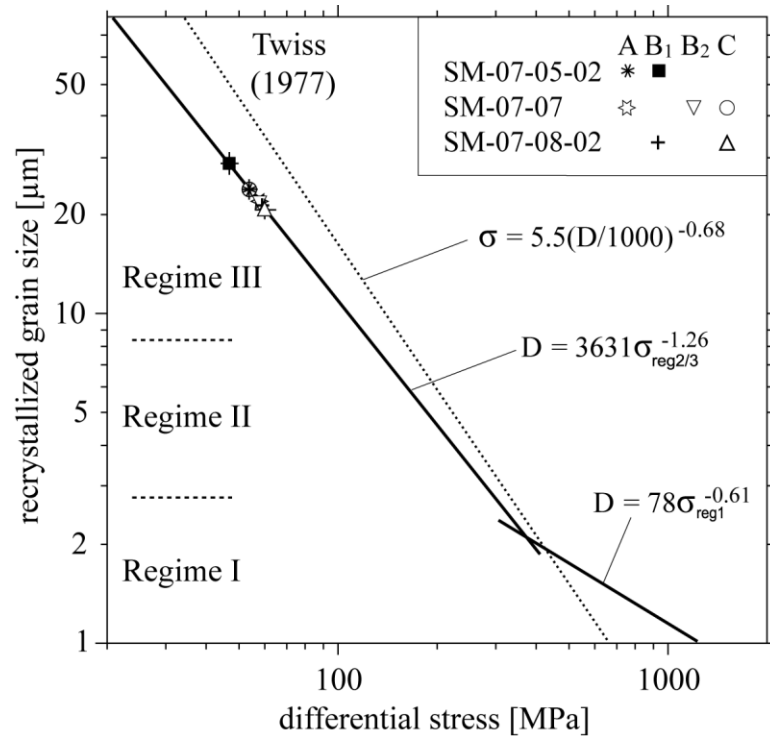


**Figure 4.10** Quartz recrystallized grain size piezometer for dynamic recrystallization Regimes I, II, and III (Stipp and Tullis, 2003). The empirical piezometer of Twiss (1977) is plotted for comparison. Samples are plotted using robust grain size estimates from high resolution EBSD maps. Error bars are plotted as horizontal and vertical lines extending from the primary symbols. Errors are relatively small and mostly do not exceed the size of the sample symbol on the figure. Calculated differential stresses increase with increasing proximity to the interpreted detachment fault surface (SM-07-05-02:SM-07-08-02).

### ***Strain Rate***

Strain rate for the South Mountains was calculated assuming that the rate of extension of the metamorphic core complex was accommodated by shear within a ductile shear zone. A strain rate for the shear zone was estimated by dividing the rate of extension by the total shear zone thickness, assuming that strain is accommodated homogeneously within the 100 to 200 m wide ductile shear zone (Davis et al., 1986). For a slip rate of  $\sim 0.3 \text{ cm yr}^{-1}$  (Fitzgerald et al., 1993), the shear strain rate is  $\approx 10^{-12}$  to  $10^{-13} \text{ s}^{-1}$ , which is in relative agreement with geologically reasonable strain rates for deformation

within extensional environments (Campbell-Stone and John, 2002; Gans and Bohrson, 1998).

## CHAPTER 5 : DISCUSSION

Type I mylonites show evidence for substantial crystal plastic deformation of quartz and limited crystal plasticity in plagioclase and orthoclase. The quartz forms a matrix of recrystallized grains that surrounds plagioclase and orthoclase porphyroclasts. The quartz is dynamically recrystallized and exhibits microstructures indicative of Regime III GBM recrystallization, which is the highest temperature category of dynamic recrystallization (Hirth and Tullis, 1992). In contrast, the relict igneous zoning and twinning textures observed in the microfractured plagioclase and orthoclase porphyroclasts indicates that the grains have not been deformed by penetrative plastic deformation. The feldspars exhibit some evidence for limited crystal plasticity in the form of bulging grain boundaries, but only along microfractures or grain boundaries, indicating that dislocations are not freely gliding or climbing within the lattice structures to promote recovery. The microstructures indicate the relative strengths of the phases during deformation; quartz readily deforms by dynamic recrystallization and is the weakest phase in the rock, whereas orthoclase and plagioclase are rheologically strong and deform with very limited crystal plasticity. These quartz and feldspar microstructures are consistent with amphibolite-grade temperatures of deformation (Passchier and Trouw, 2005). In Type I mylonites, strain localization is promoted by dynamic recrystallization of the rheologically weak and modally abundant quartz phase.

Type II mylonites also show evidence for substantial crystal plastic deformation of quartz and limited crystal plasticity in plagioclase and orthoclase, but orthoclase exhibits slightly more crystal plastic deformation than in Type I mylonites. As with Type I mylonites, the quartz forms a matrix of recrystallized grains that surround

microfractured plagioclase and orthoclase porphyroclasts. The quartz is dynamically recrystallized and exhibits microstructures indicative of Regime II SGR recrystallization, which is a lower temperature category of dynamic recrystallization compared to the Type I mylonites. The relict igneous zoning and twinning textures observed in the microfractured plagioclase and orthoclase porphyroclasts indicates that the grains have not been deformed by penetrative plastic deformation. Local and limited crystal plasticity in feldspar grains is found along microfractures or grain boundaries, indicating that dislocations are not freely gliding or climbing within the lattice structures to promote recovery. Though crystal plasticity is limited in feldspar relative to quartz, there is a slightly higher intensity of crystal plastic deformation in orthoclase grains relative to plagioclase grains in Type II mylonites. Similar to Type I mylonites, the microstructures indicate that quartz is the weakest phase in the rock, whereas orthoclase and plagioclase are rheologically strong and deform with very limited crystal plasticity. These quartz and feldspar microstructures are also consistent with amphibolite-grade temperatures of deformation (Passchier and Trouw, 2005). In Type II mylonites, strain localization is promoted by dynamic recrystallization of the rheologically weak and modally abundant quartz phase.

The mylonitic fabrics change from Type I to Type II microstructures with increasing proximity to the detachment surface, but with some microstructural variability at the macroscopic and microscopic scale. With increasing proximity to the detachment surface, the grains of the rheology-controlling phase (quartz) become increasingly interconnected, contributing to the ease of grain boundary movement during dynamic recrystallization and progressive strain localization within quartz. The transition from

high-temperature GBM recrystallization to intermediate-temperature SGR recrystallization with increasing proximity to the detachment fault indicates that strain became localized at progressively lower temperatures. Progressive strain localization with decreasing structural depth beneath the detachment fault surface and with decreasing temperatures is also indicated by the appearance of macroscopic and localized brittle shear zones that cut the mylonitic foliation.

## Slip Systems and Temperature Interpretations

### *Quartz Slip Systems*

Quartz slip systems interpreted from inverse pole figures, scatter plots, and contoured pole figures correspond to slip along the  $m$ -planes  $\{1-100\}$  and  $\{0-110\}$  in the  $a$ -direction, with a modest amount along the  $c$ -plane  $\{0001\}$ . Interpreted slip planes correspond to basal, rhomb, and prism slip systems (Figure 5.1).

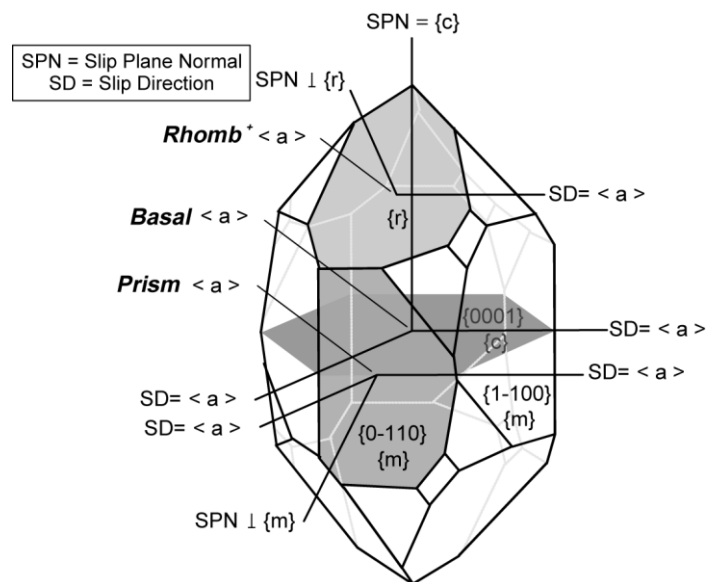


**Figure 5.1** Diagram illustrating the primary types of motion that occur for the three quartz slip systems (basal, rhomb, and prism slip) with respect to the crystal lattice. Basal  $\langle a \rangle$  slip means that dislocations move parallel to the  $\langle a \rangle$  slip direction along lattice planes that are oriented parallel to the  $c$ -plane ( $\{c\}$ ), which is the plane oriented perpendicular to the  $c$ -axis (SPN= $\{c\}$ ). Basal dominated slip produces a Type I crossed girdle skeleton fabric in quartz  $c$ -axes pole figures. Rhomb  $\langle a \rangle$  slip means that dislocations parallel to the  $\langle a \rangle$  slip direction along lattice planes oriented parallel to  $\{r\}$ . Rhomb dominated slip produces a maxima of the poles to the  $c$ -planes  $\{0001\}$  parallel to the Z-finite strain axis in quartz  $c$ -axes pole figures. Prism  $\langle a \rangle$  slip means that dislocations move parallel to the  $\langle a \rangle$  slip direction along lattice planes that are oriented parallel to the prism planes ( $\{0-110\}$  or  $\{1-100\}$ ). Prism dominated slip produces a single  $c$ -axis maximum centered on the Y-principal strain axis in quartz  $c$ -axes pole figures. Modified from Neumann (2000).

Interpreted slip systems from EBSD analysis are consistent with moderate deformation temperatures, ranging from  $\sim 500$ - $600^\circ\text{C}$  (Figure 5.2; Table 5.1) (Schmid and Casey, 1986). Temperatures interpreted in this study for active deformation temperatures in the South Mountains ductile shear zone are in relative agreement with temperature estimates from previous studies (Fitzgerald et al., 1993; Greenberg, 2010; Livaccari et al., 1995; Smith et al., 1991).

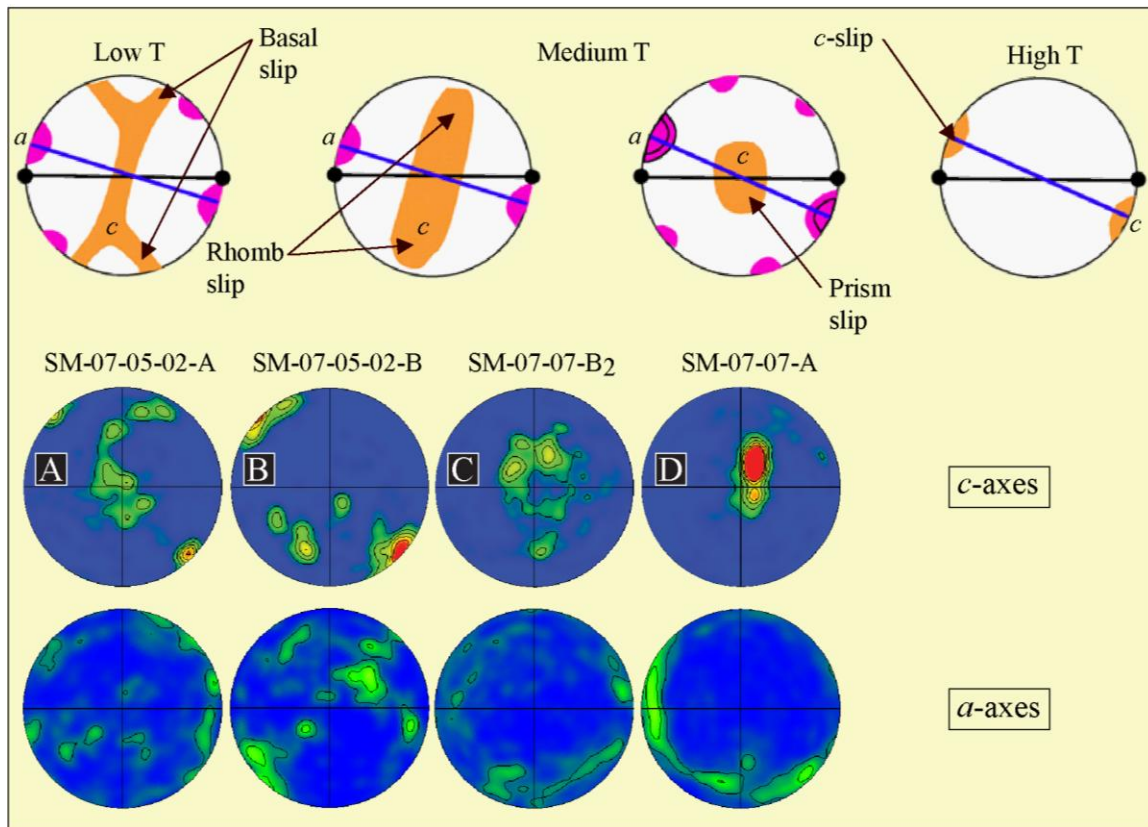


**Figure 5.2** Interpreted temperatures for various active slip systems (Schmid and Casey, 1986) and correlating South Mountain samples. Pole figures along the top row correspond to four idealized types of contoured LPO patterns for quartz *c*-axes (orange) and *a*-axes (pink). Idealized contoured LPO patterns, from left to right correspond to basal, rhomb, prism, and *c*-slip dominated slip systems, respectively. At low temperatures or high stresses more than one slip system may be active, whereas at higher temperatures only one slip system is active (Schmid and Casey, 1986; Passchier and Trouw, 1998). Therefore with an increase in relative temperature there is a progression from basal, rhomb, and prism slip to only prism slip. Samples from the South Mountains are interpreted to correlate with the following idealized contoured LPO patterns: (A) corresponds with basal dominated slip, (B) corresponds with a transition between basal and rhomb dominated slip, (C) corresponds with a transition between rhomb to prism dominated slip, and (D) corresponds with prism dominated slip.

Sample	Relative Deformation Temperature	Slip system
SM-07-05-02-A	500°C	basal $\langle a \rangle$ , rhomb $\langle a \rangle$ , and prism $\langle a \rangle$
SM-07-05-02-B	500°C	basal $\langle a \rangle$ , rhomb $\langle a \rangle$ , and prism $\langle a \rangle$
SM-07-07-B <sub>2</sub>	550°C	rhomb $\langle a \rangle$ and prism $\langle a \rangle$ slip
SM-07-07-A	600°C	rhomb $\langle a \rangle$ and prism $\langle a \rangle$ slip

**Table 5.1** Interpreted slip systems and relative deformation temperatures (Schmid and Casey, 1986; Passchier and Trouw, 1998).

### ***Feldspar Slip Systems***

Orthoclase slip systems identified from orthoclase scatter plots/contoured pole figures show samples with limited LPO development as a result of slip along the {010}<001> slip system (Figure 4.6). The {010}<001> slip system is the easiest feldspar slip system on the basis of crystal structure due to large spacing between slip planes and the small spacing in the slip direction (Mehl and Hirth, 2008). The {010}<001> slip system is indicative of medium to high-grade metamorphic conditions (Olsen and Kohlstedt, 1985), which is consistent with temperatures interpreted from quartz slip systems. Albite scatter plots/contoured pole figures show random concentrations of crystallographic axes or poles, which is suggestive of no LPO.

A strength contrast between orthoclase and albite grains lead to the development of grain size reduction dominantly by microfracturing in albite, whereas grain size reduction was accommodated by both microfracturing and very limited crystal plastic deformation in orthoclase. These observations can be interpreted as the result of differences in effectiveness of dislocation movement within the two feldspars perhaps due to chemistry. Another interpretation is that orthoclase crystal plasticity is enhanced when the proportion of the weak phase (quartz) decreases and proportions of the strong phases increase (albite and orthoclase); however this relationship has not been reported for naturally deformed or experimental samples elsewhere.

### **Dominant Deformation Mechanisms**

In both Type I and Type II mylonites, the quartz microstructures and LPO patterns suggest that quartz deforms primarily by the deformation mechanism known as dislocation creep. The prevalence of GBM and SGR recrystallization microstructures

indicate that both strain and recovery were occurring due to movement of dislocations through the quartz lattice structures. The energy to promote dislocation glide and climb through the quartz lattice structures was likely provided by the elevated temperatures of deformation implied by the quartz slip systems interpreted from the LPO patterns. Dislocation creep of quartz was also promoted by grain boundary mobility within the interconnected matrix of quartz grains. Given the modally abundant but rheologically weak nature of the quartz, I consider quartz the rheology-controlling mineral phase in the mylonites. Dislocation creep of quartz is therefore considered the rheology-controlling deformation mechanism in the mylonites.

In both Type I and Type II mylonites, the plagioclase and orthoclase microstructures and accompanying random or weak LPO patterns suggest that the feldspars were not deforming by dislocation creep or any other plastic deformation mechanism. The limited and local crystal plasticity along microfractures and grain boundaries suggests that plastic strain was accumulating in the grains, but that recovery was difficult for the rheologically-stronger feldspar grains at deformation temperatures of 500°-600° C. The random LPO patterns in plagioclase and the weak LPO pattern suggestive of limited operation of the  $\{010\}\langle 100\rangle$  slip system in orthoclase also supports the interpretation that the feldspars were not deforming dominantly by dislocation creep. Though the deformation mechanism known as diffusion creep is associated with a weak or randomized LPO, the average recrystallized grain sizes required for grain-size-sensitive diffusion creep are generally  $<10\ \mu\text{m}$ , whereas the average recrystallized feldspar grain sizes identified in this study range from  $\sim 20$  to  $70\ \mu\text{m}$ . Diffusion creep is also associated with higher deformation temperatures than those associated with

dislocation creep, but the interpreted quartz slip systems for the South Mountains samples are more consistent with moderate deformation temperatures (~500-600°C). Given the microfracturing common in the feldspar porphyroclasts, the dominant deformation mechanism for the feldspars is likely to be brittle fracturing.

### **Comparison of Natural and Predicted Conditions**

Based on microstructural and EBSD data from the naturally-deformed mylonites, I interpret that dislocation creep of quartz controls the rheology of the mylonites during ductile extension. To assess the robustness of this interpretation, I compare my interpreted deformation mechanism at the temperature interpreted from quartz *c*-axis fabrics with the deformation mechanism predicted by experimental quartz flow laws; I do this by constructing deformation mechanism maps (DMMs). DMMs display the differential stress and grain size conditions associated with the operation of a particular deformation mechanism. I construct deformation maps for quartz flow laws at the minimum and maximum temperatures of deformation (500° and 600° C, respectively), and the maps show the conditions under which dislocation and diffusion creep are operative.

The conditions where dislocation creep and diffusion creep are the dominant creep processes are calculated using experimental flow laws with the form:

$$\dot{\epsilon} = A\sigma^n d^{-m} f_{H_2O}^r e^{-(Q+pV)/RT}$$

where  $\dot{\epsilon}$  is strain rate,  $A$  is the material constant,  $\sigma$  is stress (MPa),  $n$  is the power law stress exponent,  $d$  is grain size ( $\mu\text{m}$ ),  $m$  is the grain size exponent,  $f_{H_2O}$  is the water fugacity,  $r$  is the water fugacity exponent,  $Q$  is the activation energy,  $p$  is the pressure,  $V$  is the activation volume,  $R$  is the molar gas constant, and  $T$  is absolute temperature.

I use wet quartz flow laws to construct the DMMs because the mylonitic fabric development occurred in the presence of abundant circulating fluids (Smith et al., 1991). I account for the fluid activity in the flow laws, and I used the water fugacity ( $f_{H_2O}$ ) exponent ( $r$ ) defined for the respective flow laws; water fugacities were calculated using the Tony Withers fugacity calculator which uses the Pitzer and Sterner (1994) equation.

$$\ln f = [\ln \rho + A^{\text{res}}/RT + P/\rho RT]_{P,T} + \ln(RT) - 1,$$

where  $f$  is fugacity,  $A^{\text{res}}$  is residual Helmholtz energy,  $\rho$  is 'molar' density ( $n/V$ ) and  $P$ ,  $T$ , and  $R$  are pressure, temperature and the universal gas constant, respectively. I assume that the maximum principal stress was vertical, the average bulk density is 2.6 g/cm<sup>3</sup>, and the average depth is 7.5 km, since there was 5 to 10 km of tectonic unroofing in the South Mountains (Reynolds, 1985; Livaccari et al., 1995). Water fugacities for a maximum principal stress of 191.25 MPa at 500 and 600°C are 69.6 and 101.9 MPa, respectively.

The accuracy of DMMs relies on the accuracy of differential stress estimates and appropriate selection of piezometric relationships. Therefore SMCC samples are plotted on DMMs using measured grain sizes determined by linear intercept method and the differential stress calculated from the Stipp and Tullis (2003) empirical recrystallized grain size piezometer. The Stipp and Tullis (2003) piezometer was used in this study since experimentally-produced microstructures used to calibrate their piezometer are similar to naturally-produced microstructures identified in the South Mountains. The Twiss (1977) piezometer is used only for comparison since it overestimates stress for steady state conditions (Twiss, 1977; Stipp and Tullis, 2003).

I calculate the differential stress at the BPT using Byerlee's Law. The brittle strength of the crust down to the BPT is predicted by Byerlee's law (Byerlee, 1978). I

assume that the maximum principal stress was vertical, and that the pore fluid factor ( $\lambda$ ) for the deepest parts of the South Mountains detachment fault is  $\lambda=0.4$  (hydrostatic), and that 5 to 10 km of tectonic unroofing of overburden occurred during extension (Reynolds, 1985; Livaccari et al., 1995). A Mohr circle diagram using these assumptions and Byerlee's law (coefficient of friction,  $\mu=0.85$ ) was constructed for both 5 and 10 km depth to calculate differential stress (Figure 5.3). The calculated values for the maximum and minimum differential stress for the BPT are 120 and 60 MPa, respectively. These estimates are in agreement with the highest flow stress calculated for the South Mountains using the Stipp and Tullis (2003) piezometer. Therefore a pore fluid factor of  $\lambda=0.4$  is reasonable, since a factor greater than 0.4 would reduce calculated differential stresses at the BPT below differential stresses calculated for ductile mylonites.

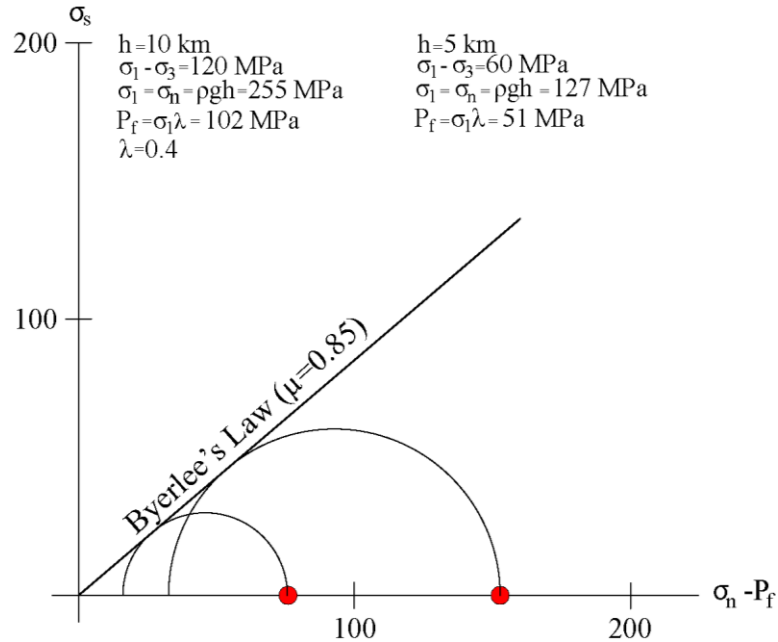


**Figure 5.3** Mohr construction for our estimated maximum and minimum brittle-plastic transition in the South Mountains of ~120 and 60 MPa.

### ***Deformation Mechanism Maps***

Two sets of DMMs were constructed using flow laws for wet quartzite (Rutter and Brodie, 2004; Hirth et al., 2001) for 500 and 600°C and a series of strain rates ( $10^{-9}$  to  $10^{-15}$  s $^{-1}$ ).

#### **500°C DMMs**

The SMCC samples plot within the dislocation creep field at 500°C, which is consistent with microstructural observations. The samples are well fit by the wet quartz flow law of Hirth et al. (2001) at a strain rate of  $10^{-11}$  to  $10^{-12}$  s $^{-1}$  strain rate contours (Figure 5.4A), which is consistent with strain estimates calculated for the South Mountains in this study ( $10^{-12}$  to  $10^{-13}$  s $^{-1}$ ). In contrast, a strain rate of  $10^{-14}$  to  $10^{-15}$  s $^{-1}$  is predicted using the wet quartz flow law of Rutter and Brodie (2004) for dislocation creep at the same conditions (Figure 5.4B). In order to have strain rates of  $10^{-14}$  to  $10^{-15}$  s $^{-1}$  with

a slip rate of  $\sim 0.3 \text{ cm yr}^{-1}$  the shear zone would have to be  $\sim 1100 \text{ m}$  thick, which is not reasonable for the South Mountains.

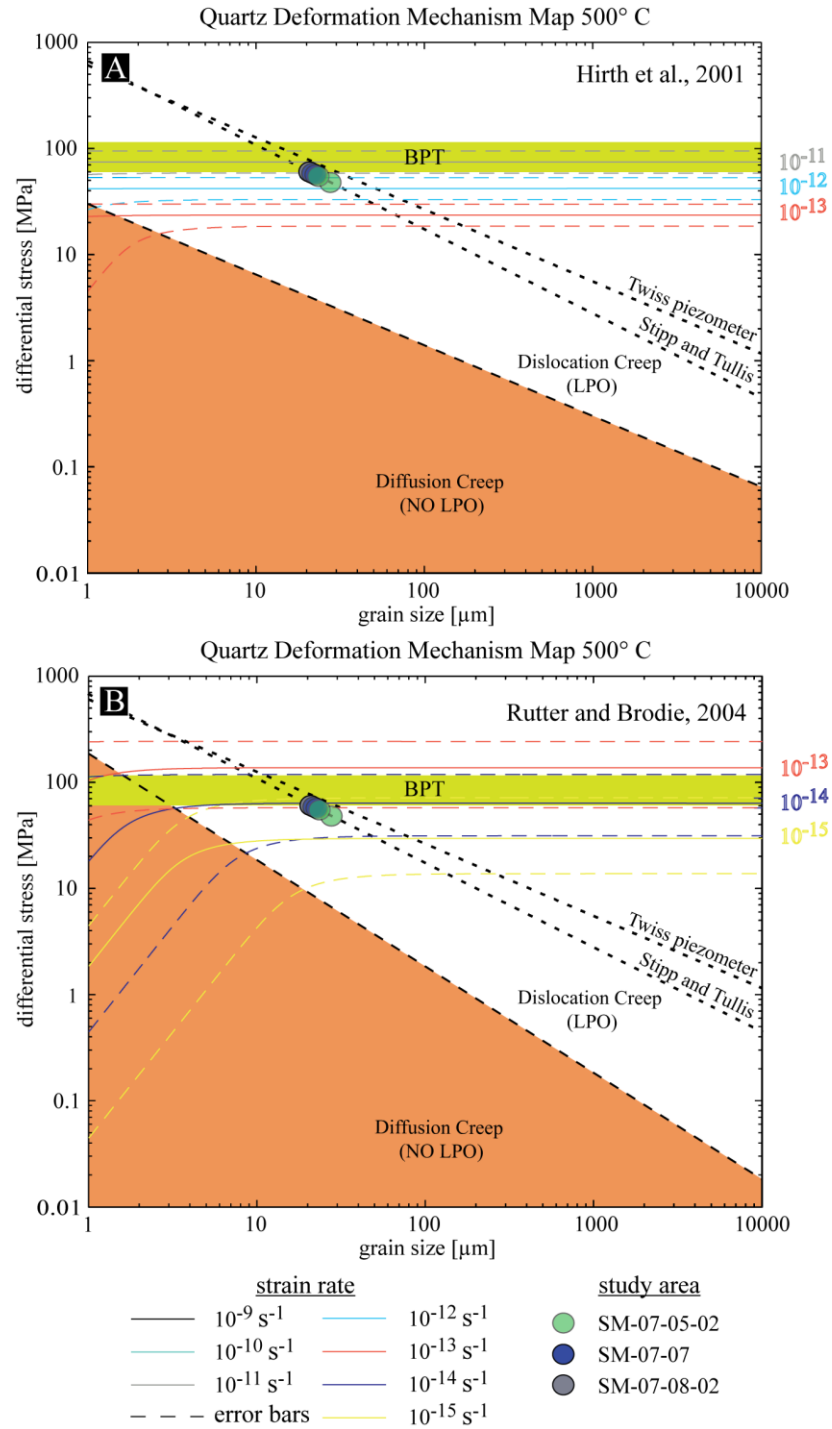


**Figure 5.4** Deformation mechanism maps (DMMs) for wet quartz at 500°C. Samples are plotted using robust grain size estimates from high resolution EBSD maps. The grain size piezometers of Stipp and Tullis (2003) and Twiss (1977) are shown with dashed lines. Calculated grain size and differential stress errors are relatively small and do not exceed the size of the sample symbol on the figure. The yellow horizontal array between 60 and 120 MPa represents the brittle-plastic transition (BPT) or the threshold stress for the onset of brittle failure. Orange shading indicates the region of diffusion creep and the dashed line represents the field boundary and transition to dislocation creep. Strain rate error is shown with dashed lines above and below the respective flow law for a given strain rate, and error bar colors correspond to that of the respective strain rate. **A.** DMM constructed using the Hirth et al. (2001) quartz flow law parameters for dislocation creep and Rutter and Brodie (2004) quartz flow law parameters for diffusion creep, and strain rates ranging from  $10^{-11}$  to  $10^{-13}$  s<sup>-1</sup>. **B.** DMM constructed using the Rutter and Brodie (2004) quartz flow law parameters for both dislocation and diffusion creep, and strain rates ranging from  $10^{-13}$  to  $10^{-15}$  s<sup>-1</sup>. For strain rates estimated in this study for the South Mountains ( $10^{-12}$  to  $10^{-13}$  s<sup>-1</sup>), the data are bracketed by the flow law of Hirth et al. (2001), whereas the flow law of Rutter and Brodie (2004) overestimates the strength of the SMCC samples.

### 600°C DMMs

Similar to the results for 500°C DMMs, the samples plot within the dislocation creep field at 600°C. The samples are well fit by the wet quartz flow law of Hirth et al. (2001) at a strain rate of  $10^{-10}$  to  $10^{-11}$  s<sup>-1</sup> strain rate contours (Figure 5.5A), which is slightly faster than strain estimates calculated for the South Mountains in this study ( $10^{-12}$  to  $10^{-13}$  s<sup>-1</sup>). Slower strain rates of  $10^{-12}$  to  $10^{-13}$  s<sup>-1</sup> are predicted using the wet quartz flow law of Rutter and Brodie (2004), which is more consistent with strain estimates for the South Mountains (Figure 5.5B).

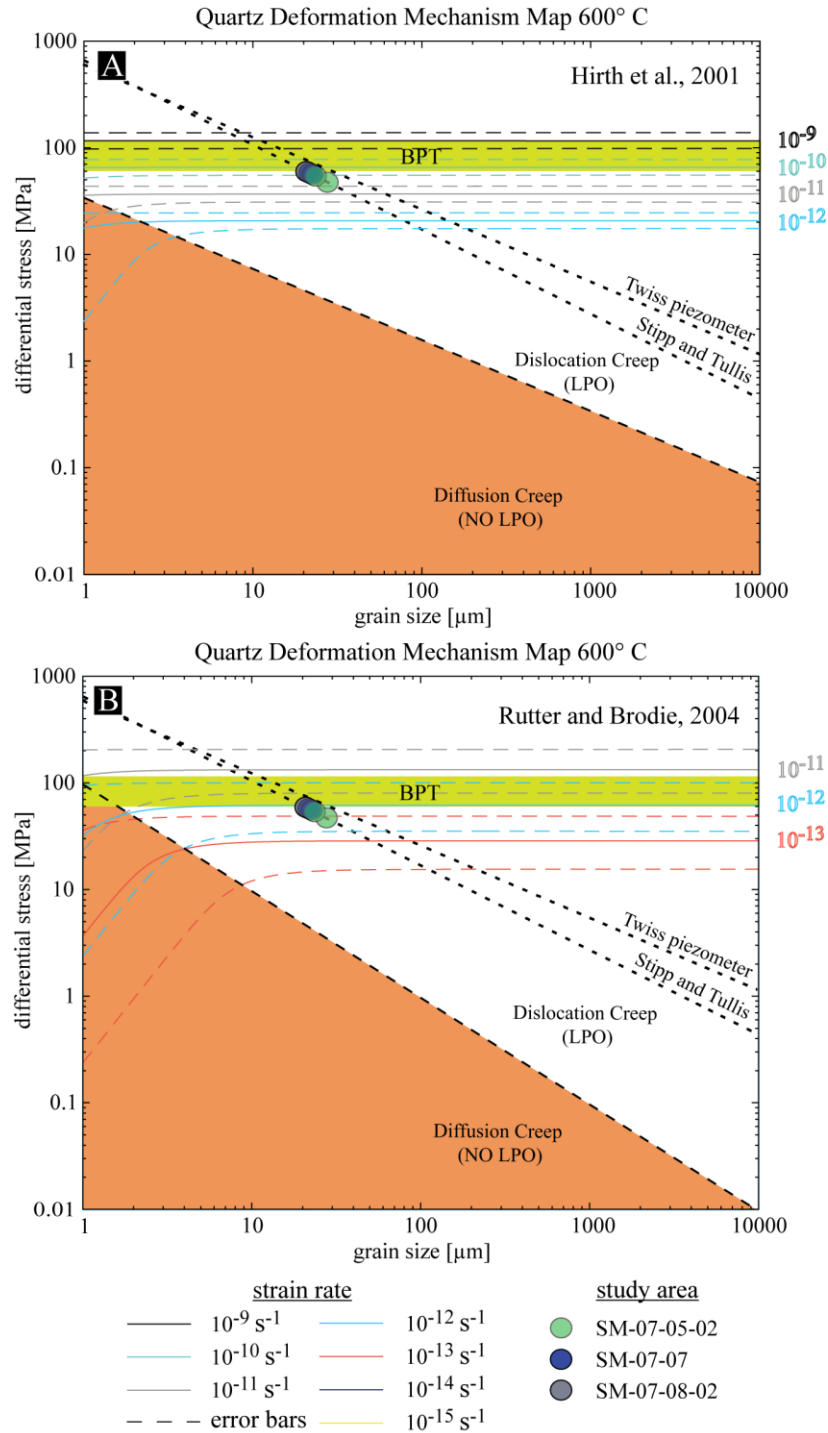


**Figure 5.5** Deformation mechanism maps for wet quartz at 600°C. Figure components are explained in Figure 5.4. For strain rates estimated in this study for the South Mountains ( $10^{-12}$  to  $10^{-13}$  s<sup>-1</sup>), the data are bracketed by the flow law of Rutter and Brodie (2004), whereas the flow law of Hirth et al. (2001) underestimates the strength of the SMCC samples.

### *Differential Stress-Temperature Curves*

Differential stress-temperature curve plots are another way to evaluate wet quartzite flow laws (Rutter and Brodie, 2004; Hirth et al., 2001) for geologically reasonable strain rates interpreted for the South Mountains from DMMs ( $10^{-12}$  to  $10^{-14}$  s<sup>-1</sup>). Differential stress-temperature curves are constructed for dislocation creep, which is consistent with microstructural observations. The SMCC samples are plotted using constraints determined in this study, which include temperatures estimated from slip systems (500 to 600°C) and differential stresses calculated from piezometry (47 to 60 MPa).

The SMCC samples are well fit by the wet quartz flow law of Hirth et al. (2001) at a strain rate of  $\sim 10^{-10}$  to  $10^{-12}$  s<sup>-1</sup> strain rate contours and Rutter and Brodie (2004) flow law at a strain rate of  $\sim 10^{-12}$  to  $10^{-14}$  s<sup>-1</sup> (Figure 5.6), which are in relative agreement with strain estimates calculated for the South Mountains in this study ( $10^{-12}$  to  $10^{-13}$  s<sup>-1</sup>). The Hirth et al. (2004) flow law predicts slightly faster strain rate or a weaker rheology for the South Mountains samples than the Rutter and Brodie (2004) flow law. However, the South Mountains samples are not expected to ‘fit’ a single strain rate, since strain in metamorphic core complexes becomes more localized with times, which leads to higher strain rates (Davis et al., 1986). Therefore, the SMCC samples are not represented by a single strain rate, but define an envelope or range from low to high strain.

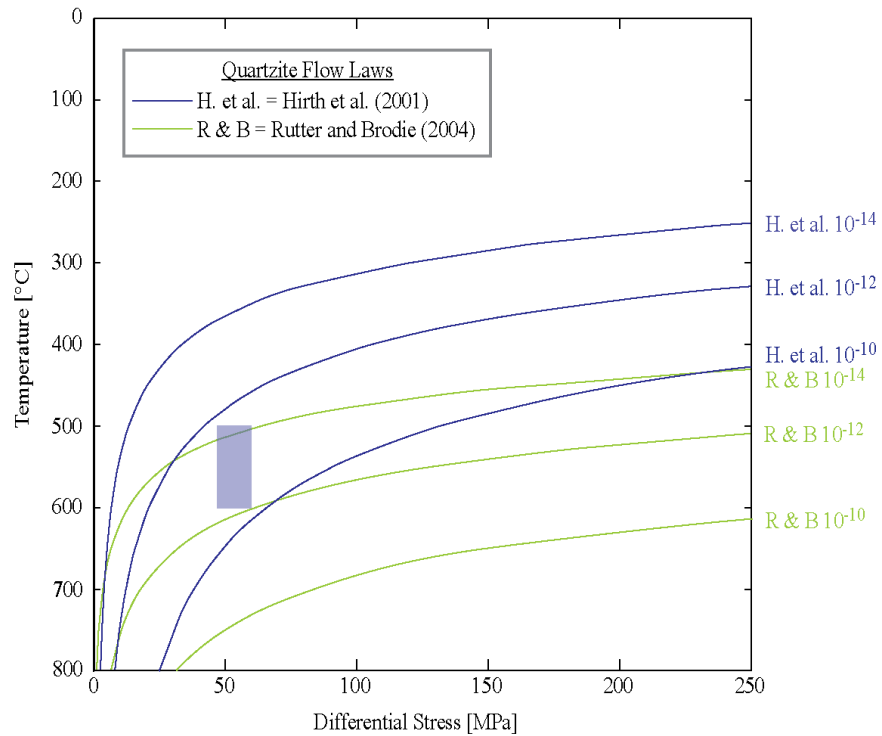


**Figure 5.6** Differential stress-temperature curves for quartzite flow laws at strain rates ranging from  $10^{-10}$  to  $10^{-14}$   $s^{-1}$ . The shaded region represents the constrained data location for strain localization within naturally deformed mylonites at the South Mountains. For strain rates estimated in this study for the South Mountains ( $10^{-12}$  to  $10^{-13}$   $s^{-1}$ ), the data are bracketed by the flow law of Hirth et al. (2001) at moderate temperatures ( $\sim 500$  to  $550^\circ\text{C}$ ), whereas the data are bracketed by the flow law of Rutter and Brodie (2004) at higher temperatures ( $>600^\circ\text{C}$ ).

### ***Log Stress-Log Strain Rate Curves***

Two sets of log stress-log strain rate curves were constructed using flow laws for wet quartzite (Rutter and Brodie, 2004; Hirth et al., 2001) and  $\text{Ab}_{100}$  (Offerhaus et al., 2001) for  $500$  and  $600^\circ\text{C}$ . Wet quartz flow laws are used in this figure to constrain the maximum strain rate, since quartz is interpreted to have deformed crystal plastically (dislocation creep), whereas a wet albite flow law (Offerhaus et al., 2001) is used to constrain the minimum strain rate, since albite constitutes a primary modal mineralogy in the South Mountains and lacks crystal plastic deformation.

### **500°C Log Stress-Log Strain Rate Curve**

The SMCC samples are plotted on the log stress-log strain rate curves using differential stresses calculated from the Stipp and Tullis (2003) empirical piezometer. All the SMCC samples are constrained by the wet quartz flow law of Hirth et al. (2001) and the wet  $Ab_{100}$  flow law of Offerhaus et al. (2001) at a strain rate of  $10^{-11}$  to  $10^{-14}$   $s^{-1}$  (Figure 5.7A), which is consistent with strain estimates calculated for the South Mountains in this study ( $10^{-12}$  to  $10^{-13}$   $s^{-1}$ ) and estimates from DMMs for 500°C. The Hirth et al. (2001) wet quartz flow law predicts the fastest strain rate for the three flow laws and the Offerhaus et al. (2001) flow law for wet  $Ab_{100}$  predicts a similar to slightly faster strain rate than the Rutter and Brodie (2004) wet quartz flow law.

### **600°C Log Stress-Log Strain Rate Curve**

The SMCC samples are constrained by the wet quartz flow law of Hirth et al. (2001) and the wet  $Ab_{100}$  flow law of Offerhaus et al. (2001) at a strain rate of  $10^{-10}$  to  $10^{-11}$   $s^{-1}$  (Figure 5.7B), which is slightly faster than strain estimates calculated for the South Mountains in this study ( $10^{-12}$  to  $10^{-13}$   $s^{-1}$ ). The Hirth et al. (2001) wet quartz flow law predicts the fastest strain rate and the Offerhaus et al. (2001) flow law for wet  $Ab_{100}$  predicts a slightly faster strain rate than the Rutter and Brodie (2004) wet quartz flow law.

The Offerhaus et al (2001) wet  $Ab_{100}$  flow law predicts a faster strain rate than the Rutter and Brodie (2004) wet quartz flow law at both 500 and 600°C, which indicates that the Rutter and Brodie (2004) flow law predicts that feldspar is weaker than quartz and is therefore crystal plastically deformed. However, these predictions are not

consistent with observed microstructures, which indicate that the Rutter and Brodie (2004) flow law underestimates the strain rate for dislocation creep at both 500 and 600°C. Therefore, the Hirth et al. (2001) flow law for wet quartzite is a better predictor of natural conditions for the SMCC samples at strain rates and temperatures interpreted for deformation conditions of the South Mountains.

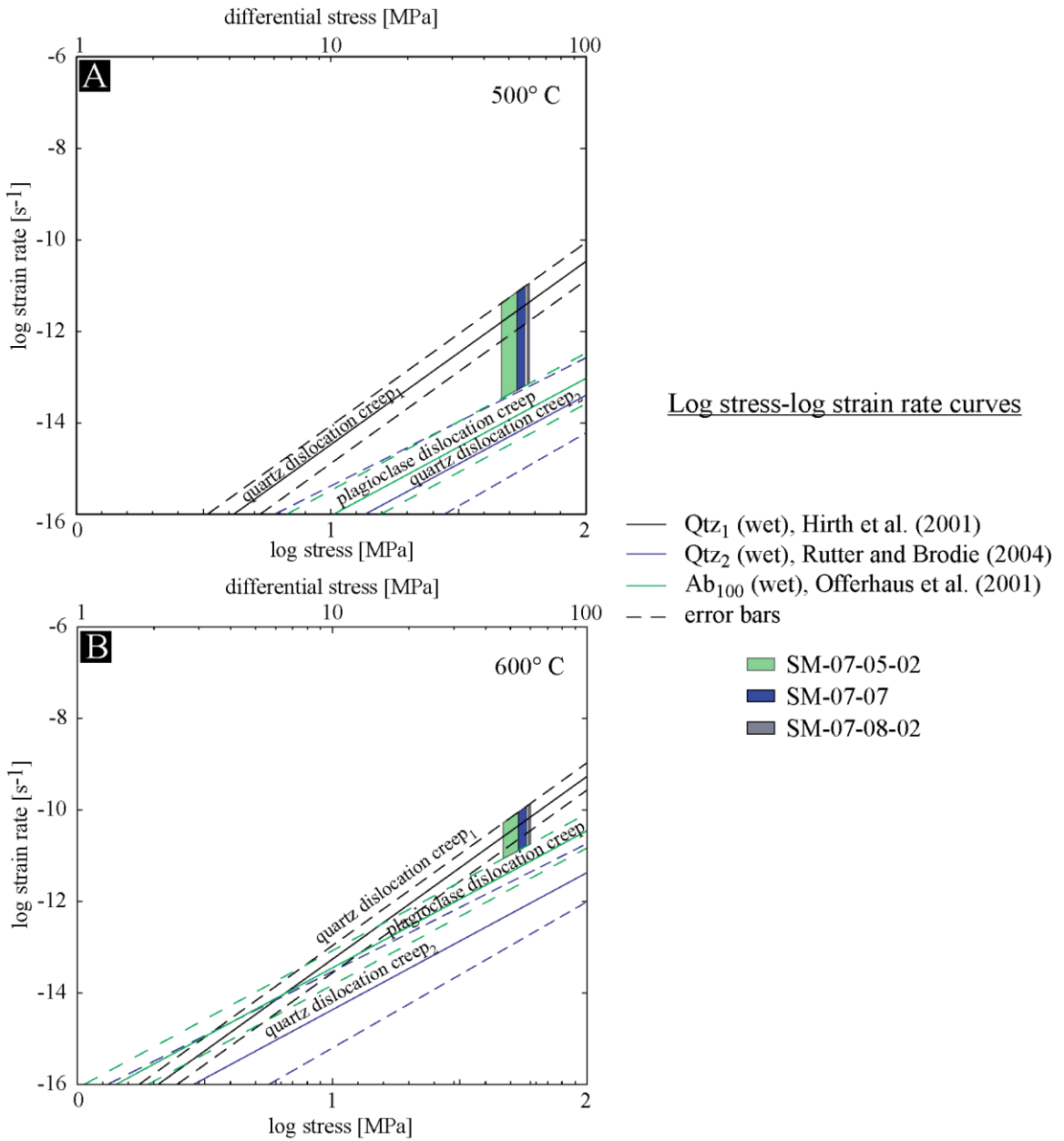


**Figure 5.7** Log stress-log strain rate curves for dislocation creep parameters for quartzite (Hirth et al., 2001; Rutter and Brodie, 2004), and  $Ab_{100}$  flow laws (Offerhaus et al., 2001) at (A) 500°C and (B) 600°C. Dashed lines represent error bars for the flow laws and reflect the error in the stress exponents of each dislocation creep flow law. The SMCC samples are plotted as a range between the highest and lowest calculated differential stress for the study areas that comprise the SMCC samples. The data are bracketed by the quartz flow law of Hirth et al. (2001) (maximum strain rate) and the albite flow law of Offerhaus et al. (2001) (minimum strain rate) at both 500 and 600°C, whereas the quartz flow law of Rutter and Brodie (2004) significantly overestimates the strength of the study areas (See text for further discussion).

## CHAPTER 6 : IMPLICATIONS FOR STRAIN LOCALIZATION

To evaluate the weakening of continental crust by strain localization, I evaluated differential stress, deformation mechanisms, and strain rates at multiple structural depths or relative depths to the interpreted South Mountains low-angle detachment fault. I identified conditions within close proximity to the fault surface to have grain sizes in the range of 20 to 21  $\mu\text{m}$ , differential stresses in the range of 59 to 60 MPa, deformation mechanisms consistent with dislocation creep, and strain rates in the range of  $10^{-10}$  to  $10^{-12}$   $\text{s}^{-1}$ . Conditions from the farthest study area from the interpreted detachment surface within the shear zone to have grain sizes in the range of 24 to 28  $\mu\text{m}$ , differential stresses in the range of 47 to 54 MPa, deformation mechanisms consistent with dislocation creep, and strain rates in the range of  $\sim 10^{-12}$  to  $10^{-14}$   $\text{s}^{-1}$ . These results show that the grain size is reduced between  $\frac{1}{4}$  to  $\frac{1}{2}$ , stress increases by  $\frac{1}{4}$  to  $\frac{1}{2}$ , and strain rates increase by up to a factor of two with increasing proximity to the interpreted detachment fault surface. The reduction in recrystallized grain size with increasing proximity to the interpreted detachment fault surface is consistent with the increase in strain localization associated with deformation in the vicinity of the BPT.

Future studies could include measurements of fluid concentration and more accurate temperatures with titanium in quartz thermometry (Wark and Watson, 2006). Accurate fluid concentrations could be combined with data derived from this study to further evaluate deformation conditions and application of flow laws for naturally deformed quartzofeldspathic rocks in the South Mountains metamorphic core complex. Titanium in quartz thermometry is ideal for determining temperatures for Type I microstructures, or microstructures dominated by GBM dynamic recrystallization (Grujic

et al., 2011). Thermometry from Type I microstructures could be used to verify temperatures interpreted from quartz slip systems, and further constrain natural deformation conditions in the South Mountains.

## CONCLUSIONS

Quartz comprises a volumetrically significant proportion (>20%) of the rock composition in the South Mountains. Microstructural and EBSD analyses were used to interpret a strong lattice preferred orientation in recrystallized quartz grains and a modest to absent LPO in orthoclase and plagioclase feldspar, respectively. Recrystallized quartz grains have LPOs consistent with basal ( $\{c\}\langle a \rangle$ ), prism ( $\{m\}\langle a \rangle$ ), and rhomb slip ( $\{r\}\langle a \rangle$ ), and orthoclase grains have a limited LPO consistent with  $\{010\}\langle 001 \rangle$  slip. EBSD analyses reveal that strain is accommodated by crystal plastic deformation in quartz, brittle fracturing in plagioclase, and limited crystal plasticity in orthoclase. These interpretations indicate that quartz has as a dominant effect on the bulk rheology.

The results suggest that wet quartzite monophasic flow laws are reasonable for modeling and evaluating deformation conditions in naturally deformed quartzofeldspathic rocks in extensional environments when quartz is volumetrically significant, interconnected, and interpreted as the weakest phase. For the strain rates ( $10^{-12}$  to  $10^{-13}$  s<sup>-1</sup>) and deformation temperatures (~500 to 550°C) estimated in this study for the South Mountains, the data are bracketed by the flow law of Rutter and Brodie (2004) at moderate temperatures, whereas the Rutter and Brodie (2004) flow law over-estimates the strength of this region. However, the Rutter and Brodie (2004) flow law may be a better predictor of natural deformation conditions at higher temperatures (>600°C).

## REFERENCES

- Behr, W.M., Platt, J.P., 2011. A naturally constrained stress profile through the middle crust in an extensional terrain. *Earth and Planetary Science Letters* 303: 181-192.
- Bons, P.D., Urai, J.L., 1994. Experimental deformation of two-phase rock analogues, *Materials Science and Engineering*, A175: 221-229.
- Brace, W., Kohlstedt, D., 1980. Limits on lithospheric stress imposed by laboratory experiments. *J. Geophys. Res.* 85: 6248-6252.
- Burgmann, R., Dresen, G., 2008. Rheology of the Lower Crust and Upper Mantle: Evidence from Rock Mechanics, Geodesy, and Field Observations, *Earth Planetary Science*, 36: 531-67.
- Byerlee, J., 1978. Friction of rocks. *Pure Appl. Geophys.* 116: 615-626.
- Campbell-Stone, E., John, B., 2002. Temporal changes in deformation mode: from failure to flow in the Colorado River extensional corridor. *Int. Geol. Rev.* 44, 512–527.
- Davis, G.A., Lister, G. S., Reynolds, S.J., 1986. Structural evolution of the Whipple and South mountains shear zones, southwestern United States, *Geology*, Vol.14: 7-10.
- Dell'Angelo, L.N., Tullis, J., 1989. Fabric development in experimentally sheared quartzites, *Tectonophysics* 169: 1-21.
- Dell'Angelo, L.N., Tullis, J., 1996. Textural and mechanical evolution with progressive strain in experimentally deformed aplite, *Tectonophysics* 256: 57-82.
- De Bresser, J.H., Ter Heege, J.H., Spiers, C. J., 2001. Grain size reduction by dynamic recrystallization: can it result in major rheological weakening? *International Journal of Earth Sciences*, 90: 28-45.
- Fitzgerald P.G., Reynolds S.J., Stump, E., Foster, D.A., Gleadow, A.J.W., 1993. Thermochronologic evidence for timing of denudation and rate of crustal extension of the South Mountains Metamorphic Core Complex and Sierra Estrella, Arizona. *Nucl. Tracks Radiat. Meas.*, Vol. 21, No. 4: 555-563.
- Gans, P., Bohron, W., 1998. Suppression of volcanism during rapid extension in the Basin and Range Province, United States. *Science* 279, 66–68.
- Gleason, C.G., Tullis, J., 1993. Improving flow laws and piezometers for quartz and feldspar aggregates, *Geophysical Research Letter*, Vol. 20, No. 19: 2111-2114.
- Greenberg, R.M., 2010. Strain localization in quartzofeldspathic mylonites: a microstructural and electron backscatter diffraction (EBSD) study of the South

- Mountains core complex, Arizona, M.S. Thesis, California State University Northridge, 1-101.
- Grujic, D., Stipp, M., Wooden, J.L., 2011. Thermometry of quartz mylonites: Importance of dynamic recrystallization on Ti-in-quartz reequilibration, *Geochemistry Geophysics Geosystems*, Vol. 12, No. 6: 1525-2027.
- Hacker, B.R., Yin, A., Christie, J.M., 1990. Differential Stress, Strain Rate, and Temperatures of Mylonitization in the Ruby Mountains, Nevada: Implications for the Rate and Duration of Uplift, *Journal of Geophysical Research*, Vol. 95, No. B6: 8569-8580.
- Hacker, B.R., 1992. Stress magnitude, strain rate, and rheology of extended middle continental crust inferred from quartz grain sizes in the Whipple Mountains, *Tectonics*, Vol. 11: 36-46.
- Handy, M.R., 1990. The solid-state flow of polymineralic rocks, *Journal of Geophysical Research*, Vol. 95, No. B6: 8647-8661.
- Handy, M.R., 1994. Flow laws for rocks containing two non-linear viscous phases: a phenomenological approach, *Journal of Structural Geology*, Vol. 16, No. 3: 287-301.
- Hirth, G., Tullis J., 1992. Dislocation creep regimes in quartz aggregates, *Journal of Structural Geology* 14: 145-159.
- Hirth, G., Teyssier, C., Dunlap, J. W., 2001. An evaluation of quartzite flow laws based on comparisons between experimentally and naturally deformed rocks, *International Journal of Earth Sciences*, 90: 77-87.
- Humphreys, F., 2001. Grain and subgrain characterisation by electron backscatter diffraction. *J. Mater. Sci.* 36: 3833-3854.
- Ji, S., Zhao, P., Xia, B., 2003. Flow laws of multiphase materials and rocks from end-member flow laws. *Tectonophysics* 270: 129-145.
- Kohlstedt, D.L., Evans, B., Mackwell, S.J., 1995. Strength of the lithosphere: Constraints imposed by laboratory experiments, *Journal of Geophysical Research*, Vol. 100, No. B9: 17,587-17,602.
- Livaccari, R.F., Geissman, J.W., Reynolds, S.J., 1995. Large-magnitude extensional deformation in the South Mountains metamorphic core complex, Arizona: Evaluation with Paleomagnetism. *GSA Bulletin*, Vol.107, No.8: 877-894.

- Mehl, L., Hirth, G., 2008. Plagioclase preferred orientation in layered mylonites: Evaluation of flow laws for the lower crust, *Journal of Geophysical Research*, Vol.113: 1-19.
- Neumann, B., 2000. Texture development of recrystallised quartz polycrystals unravelled by orientation and misorientation characteristics, *Journal of structural Geology* 22: 1695-1711.
- Offerhaus, L.J., Wirth, R., Dresen, G., 2001. High-temperature creep of polycrystalline albite. In: de Meer, S., et al. (Eds.), *Deformation Mechanisms, Rheology and Tectonics*. Utrecht University, Noordwijkerhout, The Netherlands, 124.
- Olsen, T.S., Kohlstedt, K.L., 1985. Natural deformation and recrystallization of some intermediate plagioclase feldspars, *Tectonophysics* 111: 107-131.
- Passchier, C.W., Trouw, R.A., 1998. *Microtectonics*. Springer, Berlin.
- Pitzer, K.S. and Sterner, S.M., 1994. Equations of state valid continuously from zero to extreme pressures for H<sub>2</sub>O and CO<sub>2</sub>. *Journal of Chemical Physics*. 101: 3111-3116.
- Post, A., Tullis, J., 1999. A recrystallized grain size piezometer for experimentally deformed feldspar aggregates, *Tectonophysics* 303: 159-173.
- Reynolds, S.J., 1985. *Geology of the South Mountains, central Arizona*. Arizona Bureau of Geology and Mineral Technology Bulletin 195.
- Reynolds, S.J., Shafiqullah, M., Damon, P.E., DeWitt, E., 1986. Early Miocene mylonitization and detachment faulting, South Mountains, central Arizona. *Geology* 14: 283-286.
- Rutter, E.H., Brodie, K.H., 2004. Experimental intracrystalline plastic flow in hot-pressed synthetic quartzite prepared from Brazilian quartz crystals, *Journal of Structural Geology* 26: 259-270.
- Schmid, S.M., Casey, M., 1986. Complete fabric analysis of some commonly observed quartz C-axis patterns. *Geophys Monogr* 36: 263-286.
- Sibson, R., 1983. Continental fault structure and the shallow earthquake source. *J. Geol. Soc.* 140: 741-767.
- Smith, B.M., Reynolds, S.J., Day, H.W., Bodnar, R., 1991. Deep-seated fluid involvement in ductile-brittle deformation and mineralization, South Mountains metamorphic core complex, Arizona. *Geological Society of America Bulletin*, Vol. 103: 559-569.

- Stipp, M., Stunitz, H., Heilbronner, R., Schmid, S.M., 2002. The eastern tonale fault zone: a 'natural laboratory' for crystal plastic deformation of quartz over a temperature range from 250 to 700°C, *Journal of Structural Geology* 24: 1861-1884.
- Stipp, M., Tullis, J., 2003. The recrystallized grain size piezometer for quartz, *Geophysical Research Letters*, Vol. 30, NO. 21, 2088.
- Stipp, M., Kunze, K., 2008. Dynamic recrystallization near the brittle-plastic transition in naturally and experimentally deformed quartz aggregates, *Tectonophysics* 448: 77-97.
- Stockhert, B., Brix, M.R., Kleinschrodt, R., Hurford, A. J., Wirth, R., 1999. Thermochronometry and microstructures of quartz-a comparison with experimental flow laws and predictions on the temperature of the brittle-plastic transition, *Journal of Structural Geology* 21: 351-369.
- Trimby, P., 2009. Analysis of the crystallographic signature of electron beam welds in Cu: implications for variations in etching characteristics, SKB Rapport R-09-18. SKB, Stockholm.
- Tullis, J., 2002. Deformation of Granitic Rocks: Experimental Studies and natural Examples. In: *Plastic deformation of minerals and rocks. Reviews in mineralogy and geochemistry* Volume 51: 51-96.
- Twiss, R.J., 1977. Theory and applicability of a recrystallized grain size paleopiezometer, *Pageophysics* 115: 227-244.
- Wark, D.A., Watson, E.B., 2006. TitaniQ: A titanium-in-quartz geothermometer, *Contrib. Mineral. Petrol.*, 152: 743-754.

## APPENDIX A : THIN SECTION AND POLISHING PROCEDURES

Thin sections used in this study were cut parallel to lineation and perpendicular to foliation (Figure A.1). Thin sections were cut with a water cooled rock saw with a diamond blade into approximately ½ inch thick billets, with lengths and widths consistent with standard thin sections. After billets were prepared and mounted onto slides, samples were cut and polished to a standard thin section thickness of ~30 µm. Final thickness was determined by comparing the interference colors of minerals with high modal abundances (e.g. quartz, feldspar) to standard interference color charts.

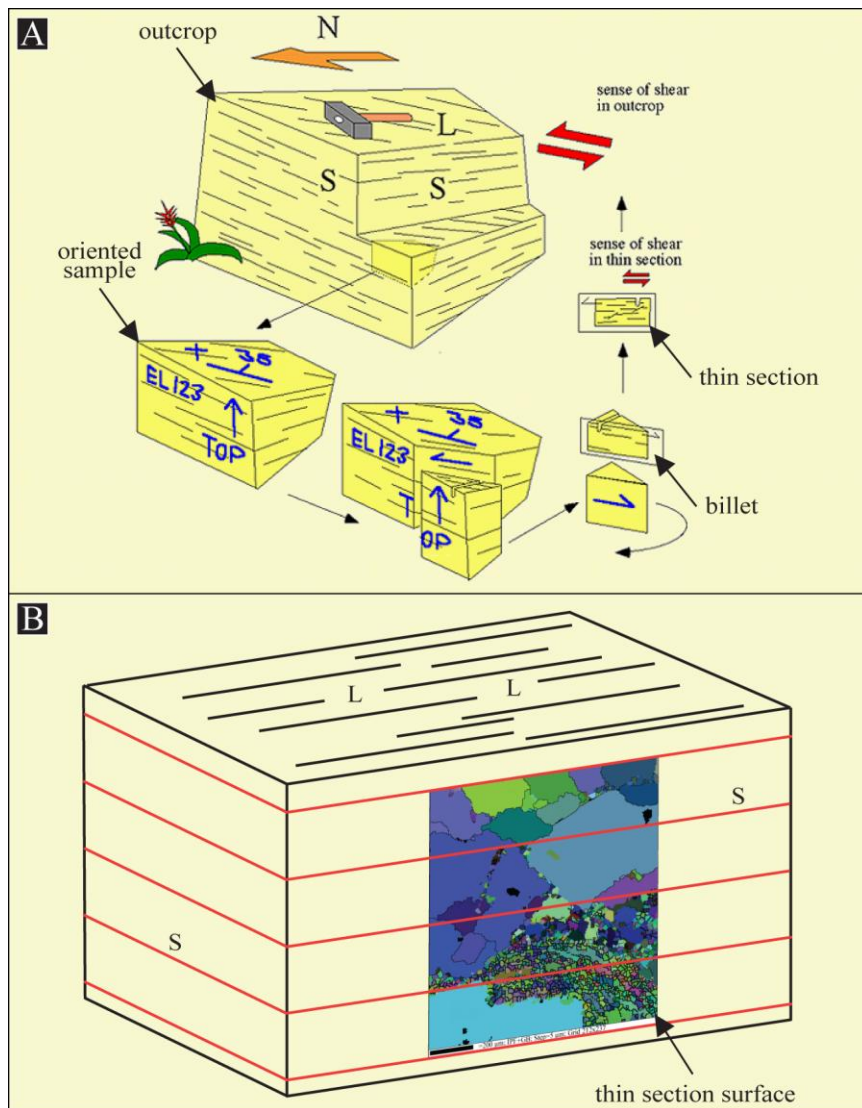


**Figure A.1** Diagram illustrating collecting oriented field samples and thin section production. Oriented samples are collected with respect to foliation and lineation. **(A)** Thin sections are constructed so that they are representative of the motion plane; the thin section surface is cut perpendicular to foliation (S) and parallel to lineation (L). **(B)** Thin sections used for microstructural and EBSD analysis are analyzed with respect to the motion plane. Modified from Passchier and Trouw (1998).

Thin section construction introduces crystal damage in the uppermost surface of the sample and therefore required extensively polished before EBSD analyses. Polishing minimizes surface damage and helps generate better quality and reproducible EBSD data. Thin section polishing consists of four rounds of polishing with the Buehler MiniMet 1000 Grinder-Polisher. Required materials include distilled water, kimwipes, Buehler Metadi polishing fluids (1, 3, and 6  $\mu\text{m}$ ), MasterMet 2 non-crystallizing colloidal silica, Fisher Scientific 20 Tabletop Ultrasonic Cleaner, Buehler adhesive-backed polishing microcloth, glass plates, and polishing bowls. There is a specific glass plate and polishing bowl for each round of polishing to help minimize contamination.

Polishing procedures include: adding approximately four pumps of polishing fluid and distilled water to the polishing cloth and respective polishing bowl. The samples were then polished with four different types of polishing fluid (1, 3, 6  $\mu\text{m}$ , and non-crystallizing colloidal silica) for 60 minutes per a fluid (Table A.1). Preceding each polishing round slides are rinsed with distilled water and then washed in an Ultrasonic Cleaner for 3 minutes to remove residual polishing solution. Slides are dried with Kimwipes to prevent abrasion and contamination to polished surfaces.

<b>Time:</b> <b>6 <math>\mu\text{m}</math></b>	<b>Time:</b> <b>3 <math>\mu\text{m}</math></b>	<b>Time:</b> <b>1 <math>\mu\text{m}</math></b>	<b>Time:</b> <b>Silica</b>	<b>Pressure</b>	<b>RPM</b>
60 min.	60 min.	60 min.	60 min.	4 lb	25

**Table A.1** Polishing description including polished time at 6, 3, and 1  $\mu\text{m}$ , and colloidal silica; pressure applied during polishing; and polishing speed (RPM).

## APPENDIX B : EBSD PROCESSING AND RE-INDEXING PROCEDURES

Electron backscatter diffraction (EBSD) provides a quantitative method to determine microstructural information about the crystallographic nature of minerals (Figure B.1). Types of crystallographic information calculated by EBSD includes: (1) determining crystallographic orientations, (2) identifying primary modal mineralogy and quantifying modal proportions, (3) calculating grain and subgrain boundaries with crystallographic misorientations of adjacent points, and (4) calculating grain sizes using grain boundaries that were determined by crystallographic misorientations.

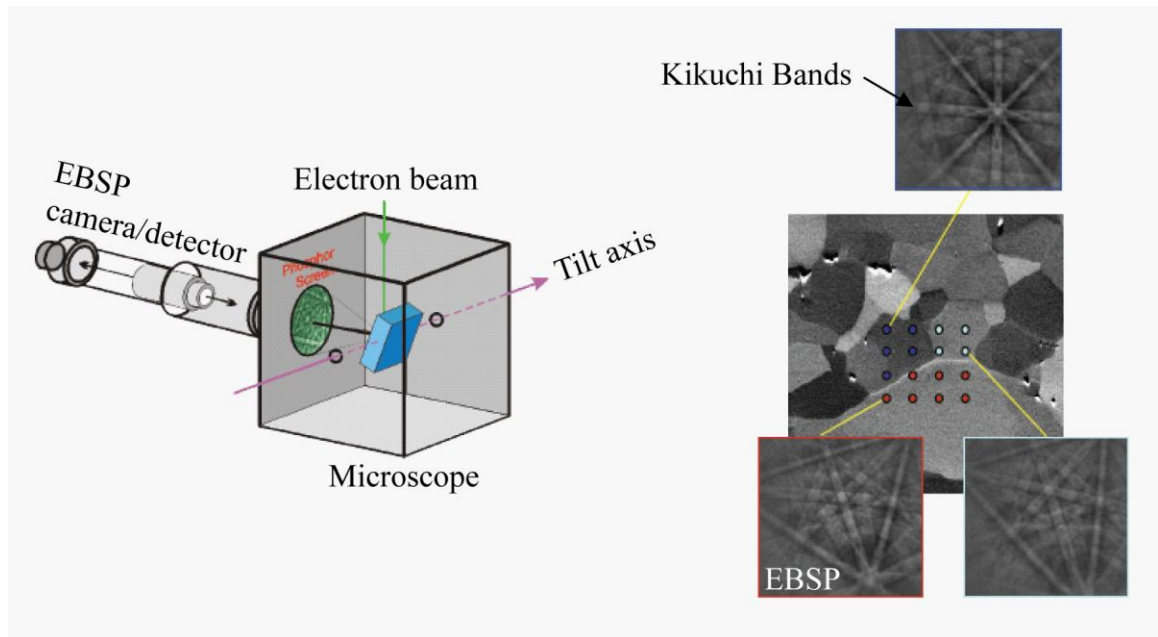


**Figure B.1** Diagram illustrating how EBSD works and how it is utilized in this study. EBSD works by projecting an electron beam onto the sample surface, which is tilted to  $70^\circ$ , relative to the incident beam. The interaction of the electron beam with the crystal lattice results in a low energy loss of electrons, which are subject to path differences that lead to constructive and destructive interference. A phosphor screen is placed a short distance from the sample surface in the path of the diffraction loss, which allows the diffraction pattern to be seen and captured with a camera. Channel 5 software is used to identify kikuchi bands for each electron backscatter pattern (EBSP). Kikuchi bands are used to identify mineral phases and crystallographic orientations of the crystal lattice for each point. The diagram shows how crystallographic misorientations between adjacent points are used to quantify grain boundaries. Modified from Trimby (2009).

EBSD data was collected at California State University San Francisco and reprocessed with CHANNEL 5 suite software at California State University Northridge. Standard noise reduction was conducted in which all wild spikes were removed and a minimum grain boundary angle of 10° was set. The following phases were analyzed: quartz, orthoclase, and albite. The dependent variables outlined in Table B.1 were applied to all EBSD analyses.

Parameter	Comment
kV and aperture	20 kV
Tilt	70°
Binning	2x2
Gain	Low
Calibration V/H	0.762
Hough Resolution	70
EDS Phases	Al, Si, K, Na, Ca

**Table B.1** Testing parameters and conditions for EBSD analysis.

Independent variables for EBSD analyses include maximum and minimum band widths, mean angular deviation (MAD), working distance, EBSD camera distance, timing per frame, number of frames, and noise reduction. The number of detection bands is correlated to the symmetry of the material being indexed. More detection bands reduce misindexing, especially for low symmetry materials, but too many detection bands will decrease hit rates. Too few detection bands increase the hit rate and causing indexing to proceed faster, but too few bands can lead to misindexing of both phases and crystallographic orientations. Common settings for low symmetry materials like geologic samples are between 5 and 8. The mean angular deviation or quality of solution is ideally less than 1 and in general the smaller the better. The average working distance ranges from 12 to 20 mm. The camera distance is ~175.5 mm. The timing per frame controls the

exposure time of the sample and generally ranges from 50 to 100. Independent variables for each EBSD analyses are outlined in Table B.2, Table B.3, and Table B.4.

<b>Study region</b>	<b>Min Bands</b>	<b>Max Bands</b>	<b>Calibration File</b>	<b>Timing per Frame</b>	<b>Hough</b>	<b># Reflectors</b>
<b>A</b>	-	-	WD 20.0 mm	100 ms	-	-
Re-index #1	5	6	175.5 mm	-	50	78
Re-index #2	7	8		-	60	78
<b>B</b>	-	-	WD 20.0 mm	100 ms	-	-
Re-index #1	5	6	175.5 mm	-	60	70
Re-index #2	6	7		-	60	78
Re-index #3	6	7		-	50	70
<b>C</b>	-	-	WD 20.0 mm	100 ms	-	-
Re-index #1	5	6	175.5 mm	-	60	78
Re-index #2	6	7		-	60	70
Re-index #3	6	8		-	60	78
Re-index #4	6	8		-	50	78
Re-index #5	5	6		-	50	78

**Table B.2** Sample 07-05-02 independent variables for EBSD analyses. Independent variables include: minimum bands, maximum bands, calibration parameters, timing per frame, Hough number, and number of frames. The Mean angular deviation is less than 1.

<b>Study region</b>	<b>Min Bands</b>	<b>Max Bands</b>	<b>Calibration File</b>	<b>Timing per Frame</b>	<b>Hough</b>	<b># Reflectors</b>
<b>A</b>	-	-	WD 18.0 mm	40 ms	-	-
Re-index #1	6	7	175.5 mm	-	50	78
Re-index #2	6	7		-	50	78
Re-index #3	5	6		-	50	70
<b>B<sub>1</sub></b>	-	-	WD 16.0 mm	80 ms	-	-
Re-index #1	5	6	175.5 mm	-	60	70
Re-index #2	6	7		-	55	65
Re-index #3	7	8		-	50	65
<b>B<sub>2</sub></b>	-	-	WD 16.0 mm	80 ms	-	-
Re-index #1	5	6	175.5 mm	-	50	78
Re-index #2	6	8		-	50	78
<b>C</b>	6	7	WD 18.0 mm	40 ms	50	78
Re-index #1	5	6	175.5 mm	-	50	70

**Table B.3** Sample 07-07 independent variables for EBSD analyses. Independent variables include: minimum bands, maximum bands, calibration parameters, timing per frame, Hough number, and number of frames. The Mean angular deviation is less than 1.

<b>Study region</b>	<b>Min Bands</b>	<b>Max Bands</b>	<b>Calibration File</b>	<b>Timing per Frame</b>	<b>Hough</b>	<b># Reflectors</b>
<b>A</b>	-	-	WD 20.0 mm	100 ms	-	-
Re-index #1	5	6	175.5 mm	-	50	70
Re-index #2	6	7		-	55	60
Re-index #3	7	8		-	50	65
Re-index #4	6	8		-	60	60
Re-index #5	5	6		-	70	60
<b>B</b>	-	-	WD 20.0 mm	100 ms	-	-
Re-index #1	5	6	175.5 mm	-	50	70
Re-index #2	6	8		-	60	70
<b>C</b>	-	-	WD 20.0 mm	80 ms	-	-
Re-index #1	6	7	175.5 mm	-	50	78
Re-index #2	6	8		-	50	78
Re-index #3	6	8		-	50	78

**Table B.4** Sample SM-07-08-02 independent variables for EBSD analyses. Independent variables include: minimum bands, maximum bands, calibration parameters, timing per frame, Hough number, and number of frames. The Mean angular deviation is less than 1.

## APPENDIX C : EBSD BEAM MAPS AND POLE FIGURES

Many of the EBSD beam maps and pole figures included in the results section of this thesis are repeated below. Figures are repeated to allow for the inclusion of a comprehensive set of unannotated EBSD beam maps, quartz *c*-axis and *a*-axes pole figures in order of increasing proximity to the interpreted detachment surface (SM-07-05-02:SM-07-08-02).

EBSD beam map figures are composed of the following subfigures: **(A)** photomicrograph of a micro-scale ductile shear zone; the yellow rectangle corresponds to the area evaluated by EBSD analysis, **(B)** phase map in which orthoclase, albite, and quartz grains were identified, **(C)** EBSD beam map from the inset area in the photomicrograph where quartz and feldspar crystallographic orientations are defined by IPF (IPF coloring corresponds to specific crystallographic directions oriented parallel to lineation) and Euler angles (Euler angle coloring corresponds to relative crystallographic orientations), respectively, **(D)** band contrast map, used as a proxy for pattern quality, and **(E)** quartz *c*-axis pole figures (lower hemisphere equal area plots).

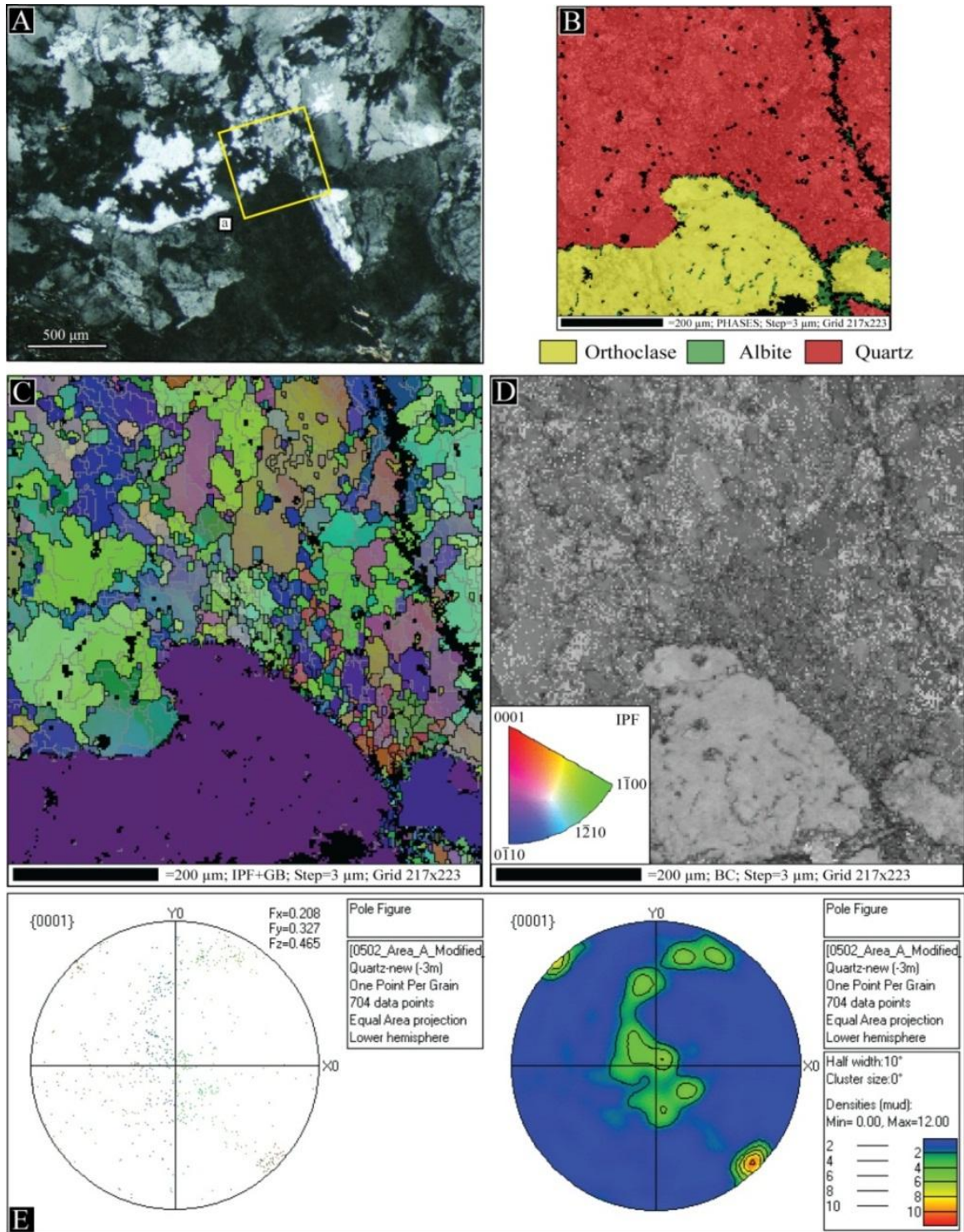


**Figure C.1** Location of EBSD beam map and EBSD results for sample SM-07-05-02, study region A.

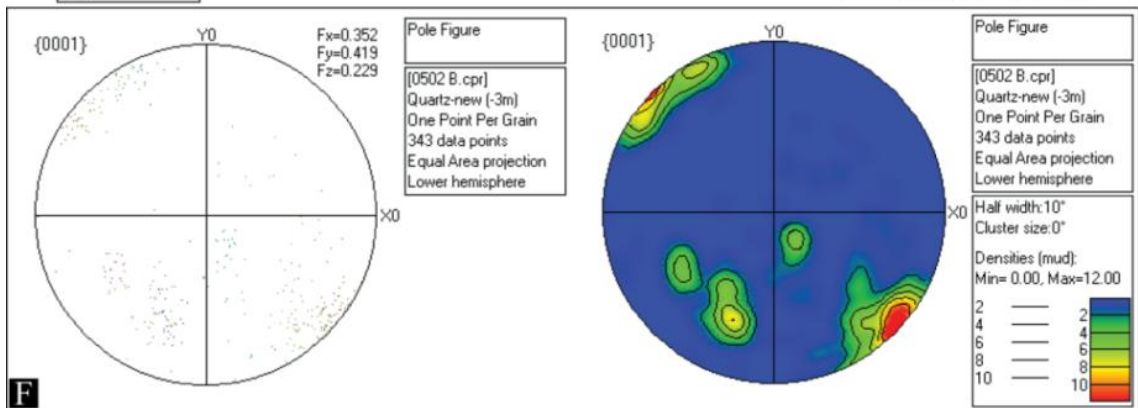
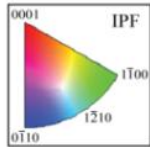
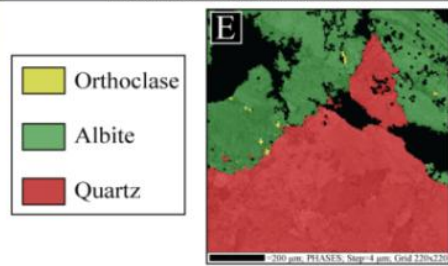
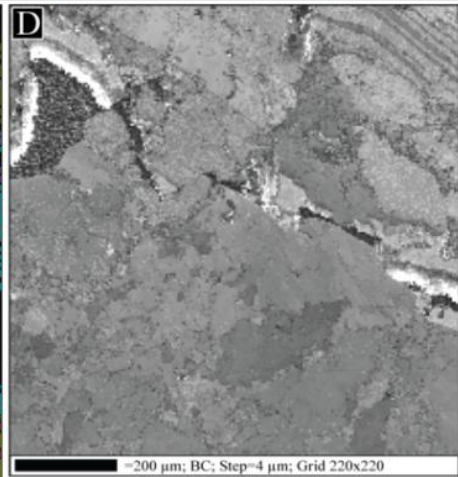
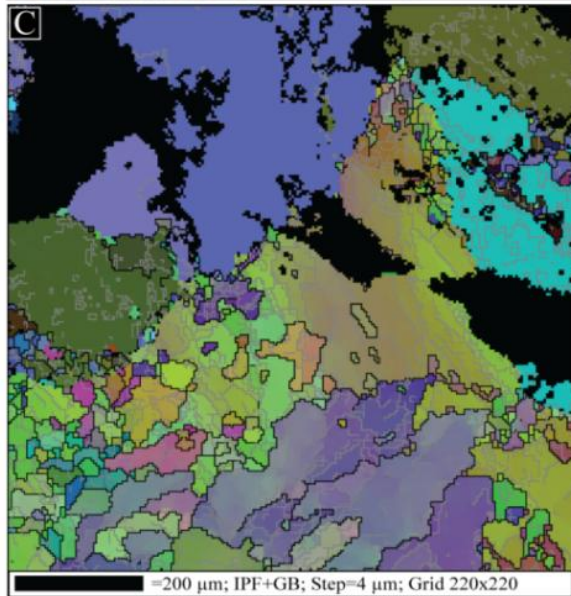
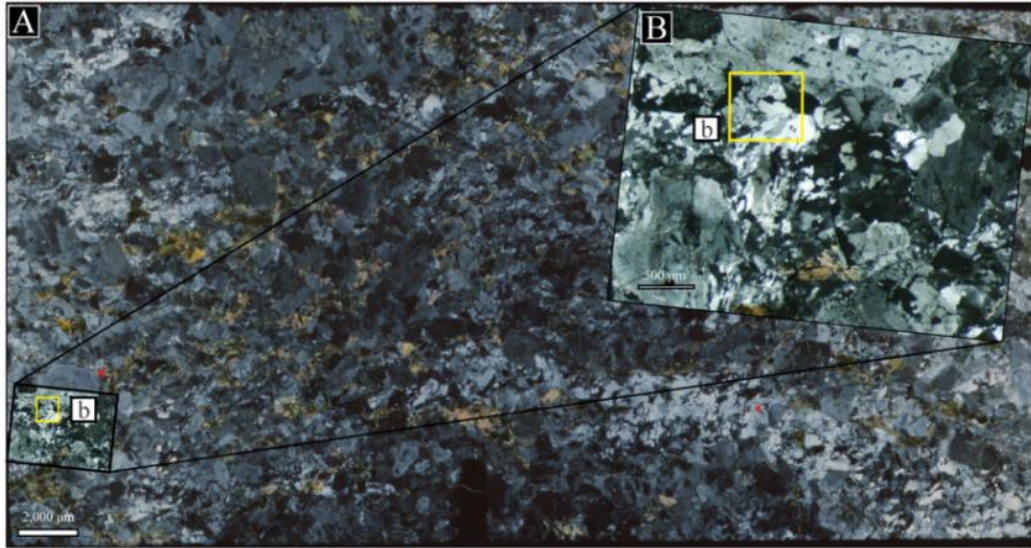


**Figure C.2** Location of EBSD beam map and EBSD results for sample SM-07-05-02, study region B.

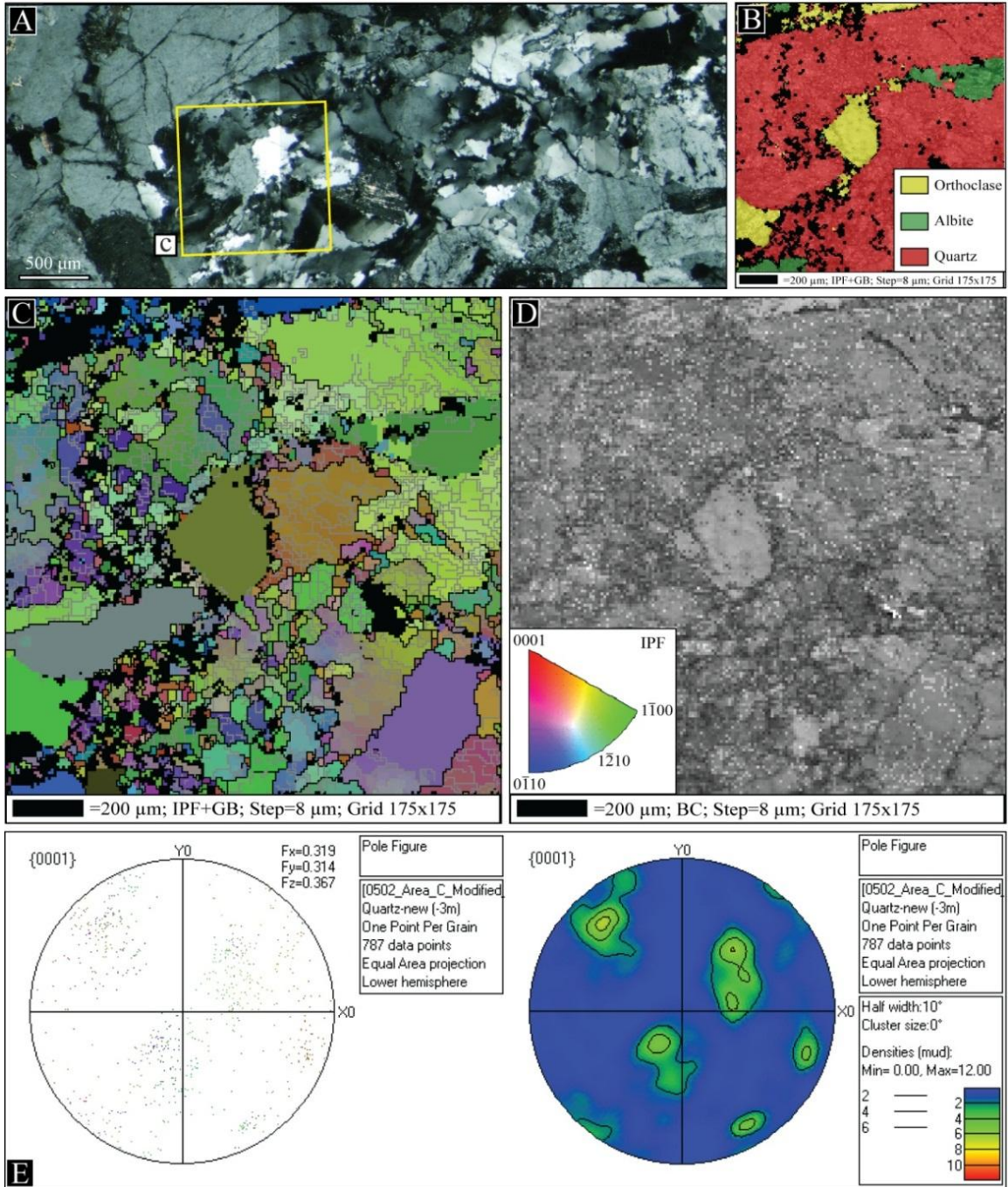


**Figure C.3** Location of EBSD beam map and EBSD results for sample SM-07-05-02, study region C.

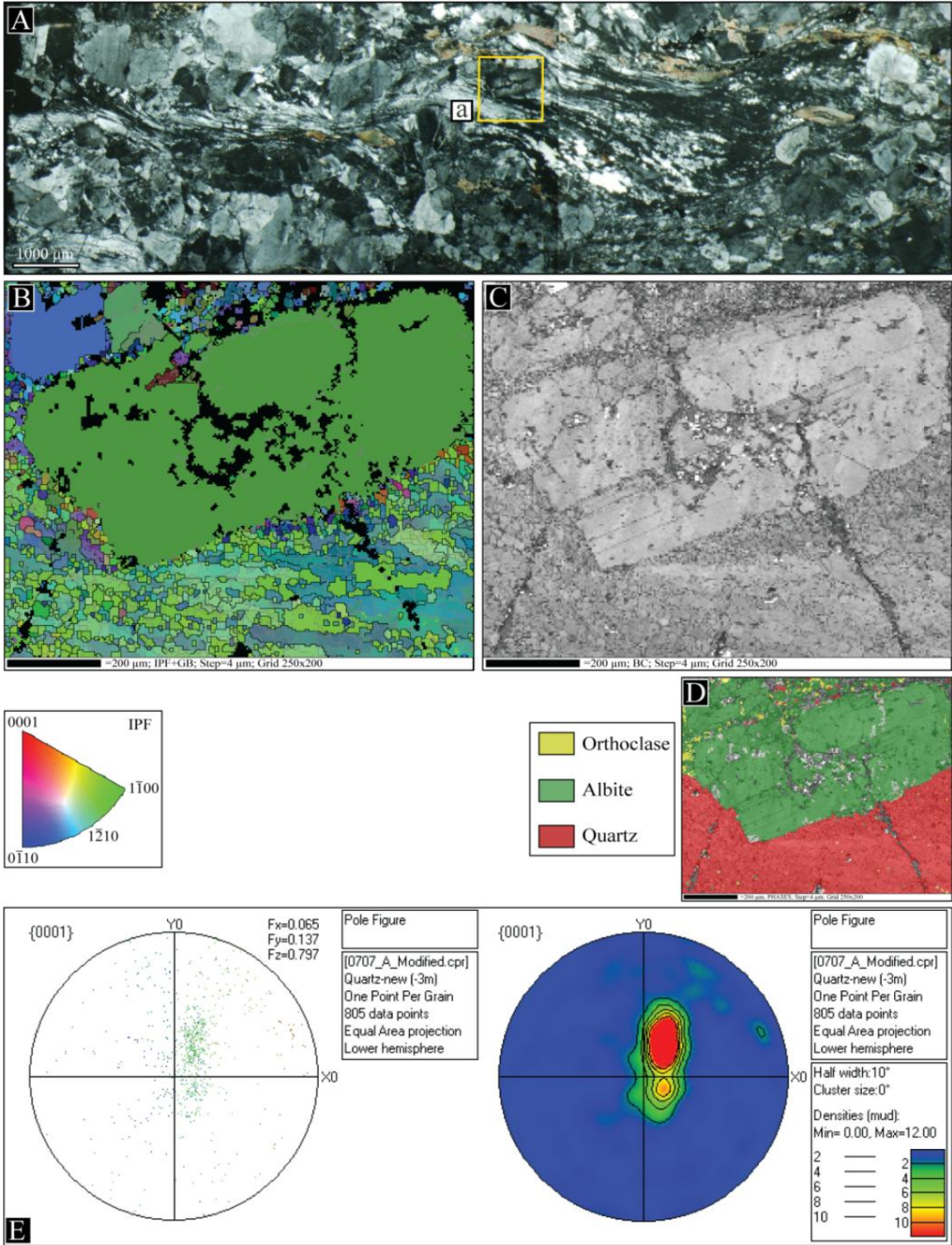


**Figure C.4** Location of EBSD beam map and EBSD results for sample SM-07-07, study region A.

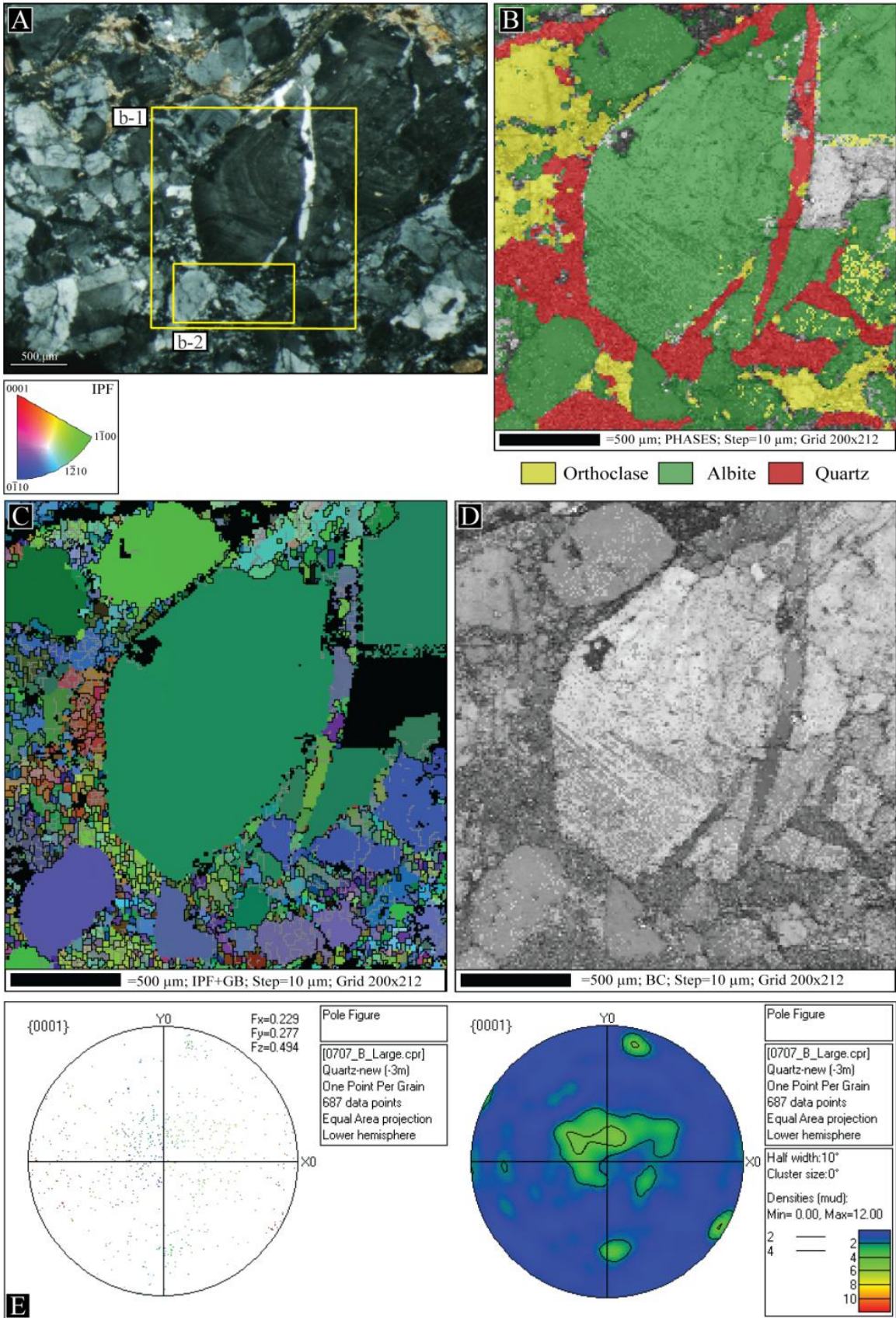


**Figure C.5** Location of EBSD beam map and EBSD results for sample SM-07-07, study region B<sub>1</sub>.

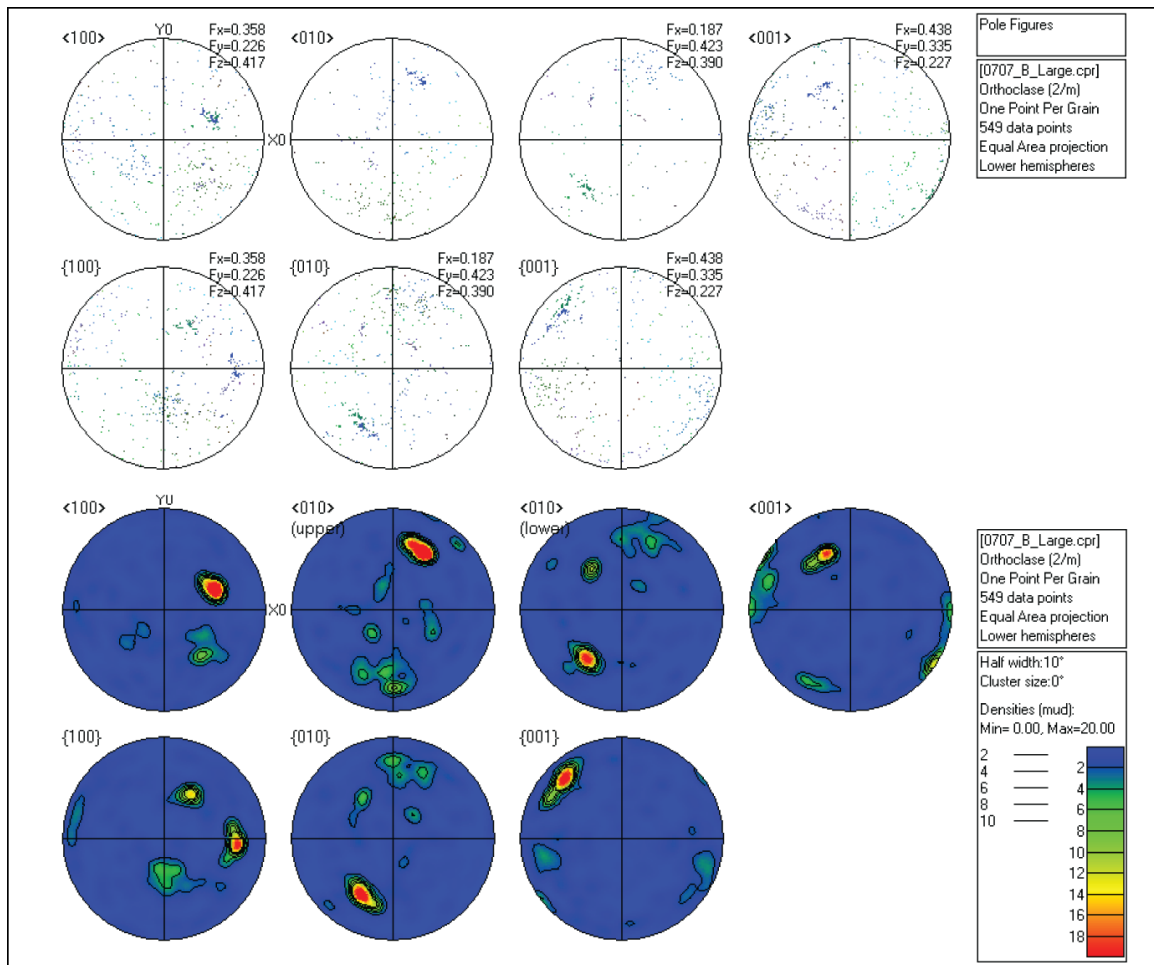


**Figure C.6** Orthoclase pole figures for sample SM-07-07, study region B<sub>1</sub>. Pole figures are constructed such that the macroscopic foliation is parallel to X0 and the stretching lineation is contained within the foliation and intersects the primitive circle.

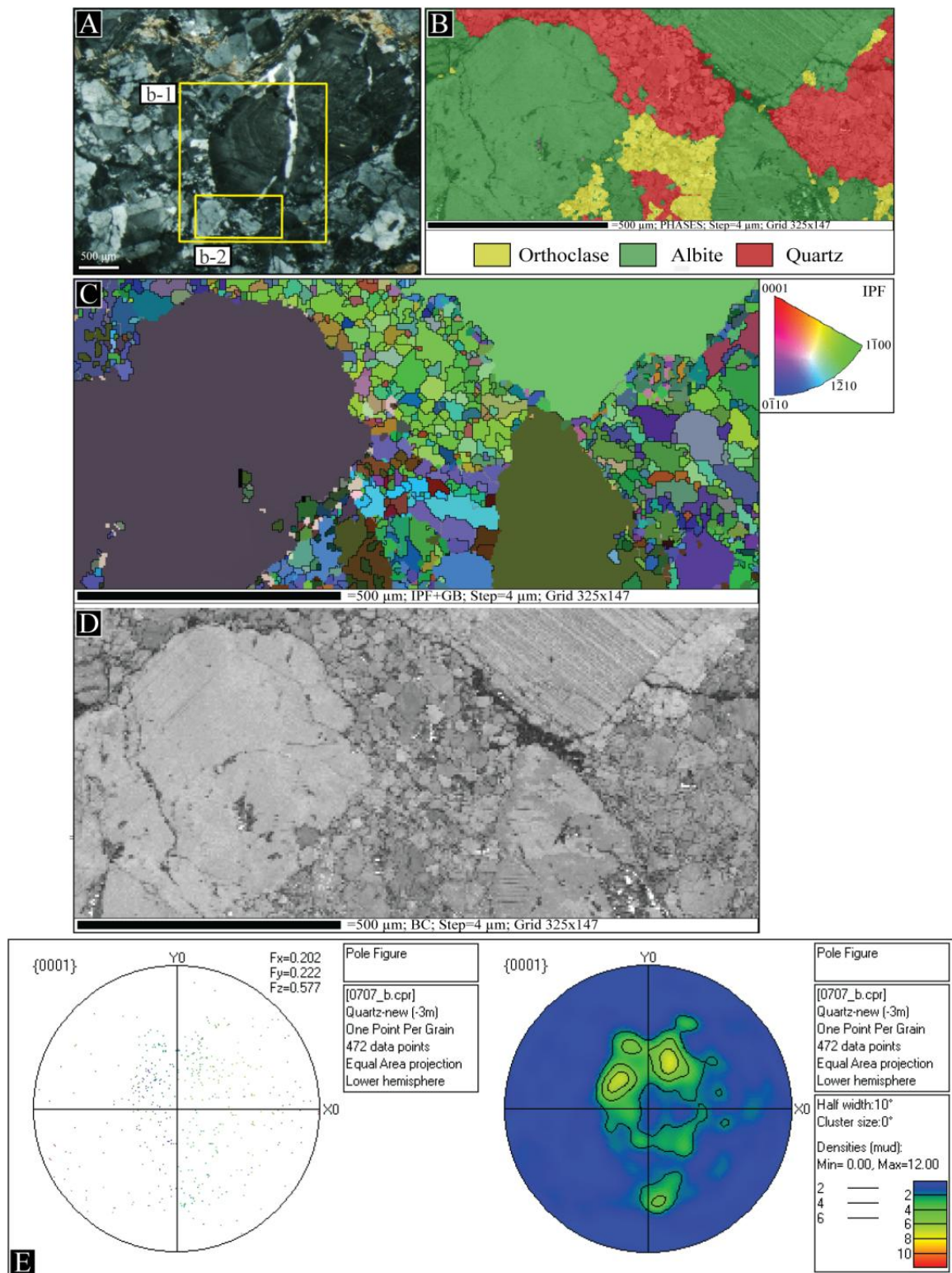


**Figure C.7** Location of EBSD beam map and EBSD results for sample SM-07-07, study region B<sub>2</sub>.

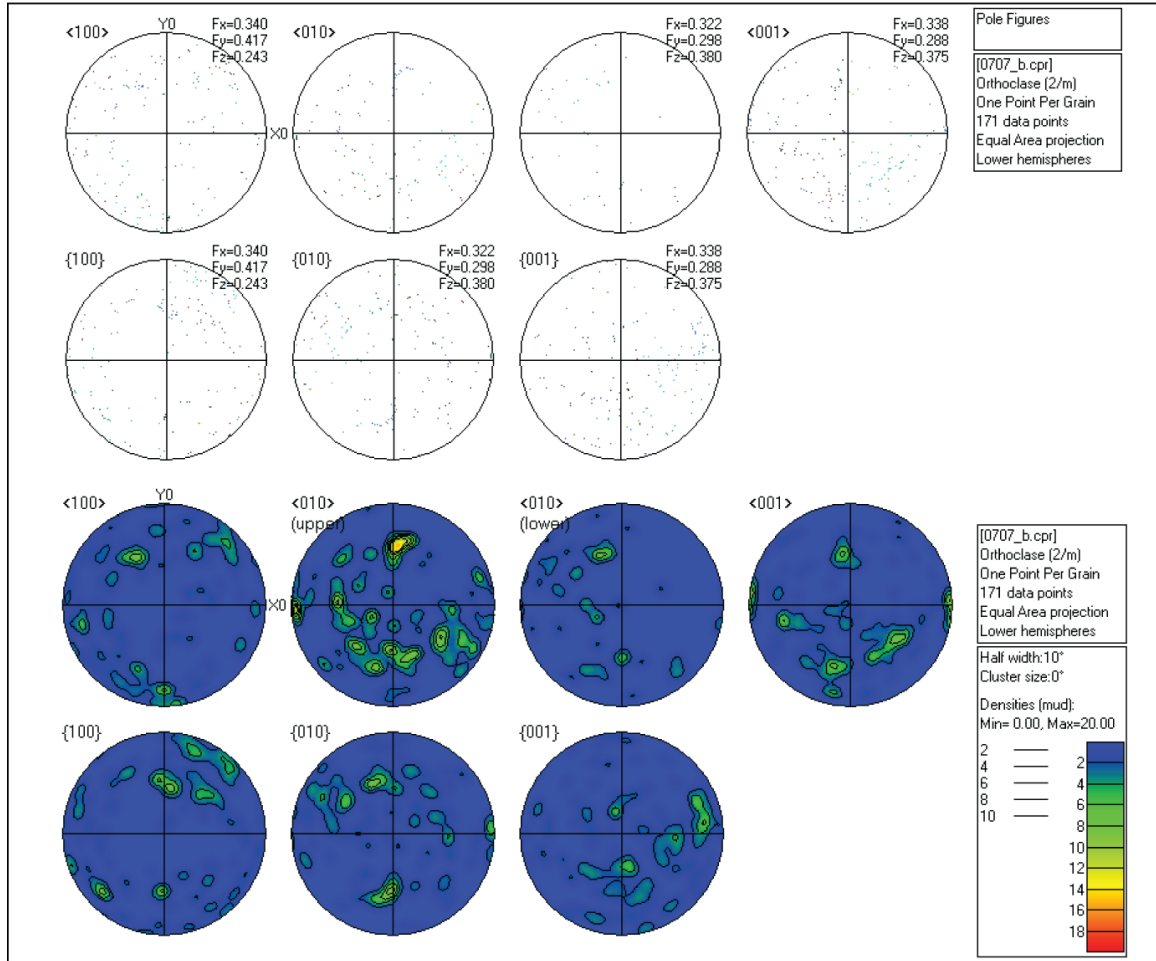


**Figure C.8** Orthoclase pole figures for sample SM-07-07, study region B<sub>2</sub>. Pole figures are constructed such that the macroscopic foliation is parallel to X0 and the stretching lineation is contained within the foliation and intersects the primitive circle.

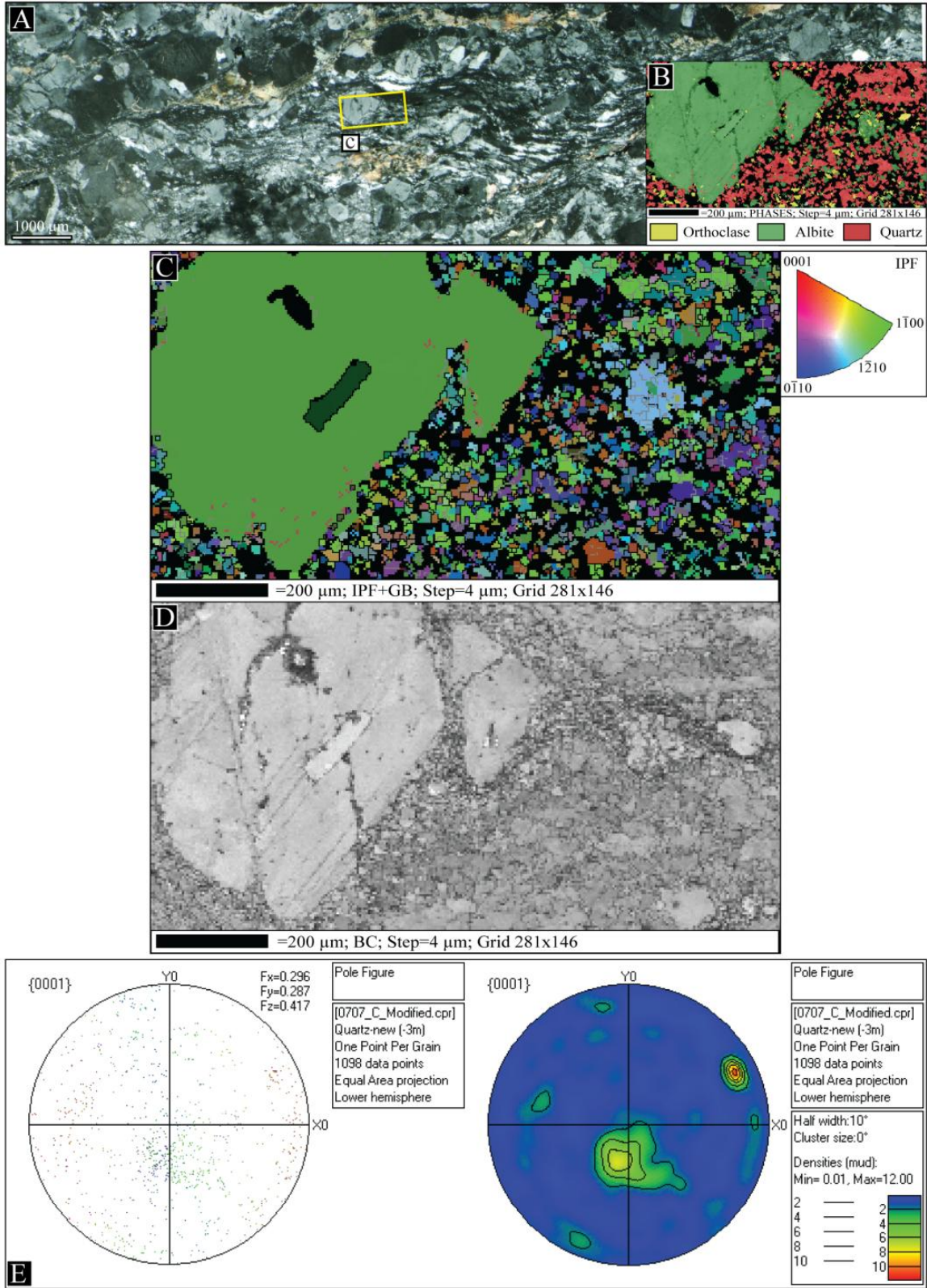


**Figure C.9** Location of EBSD beam map and EBSD results for sample SM-07-07, study region C.

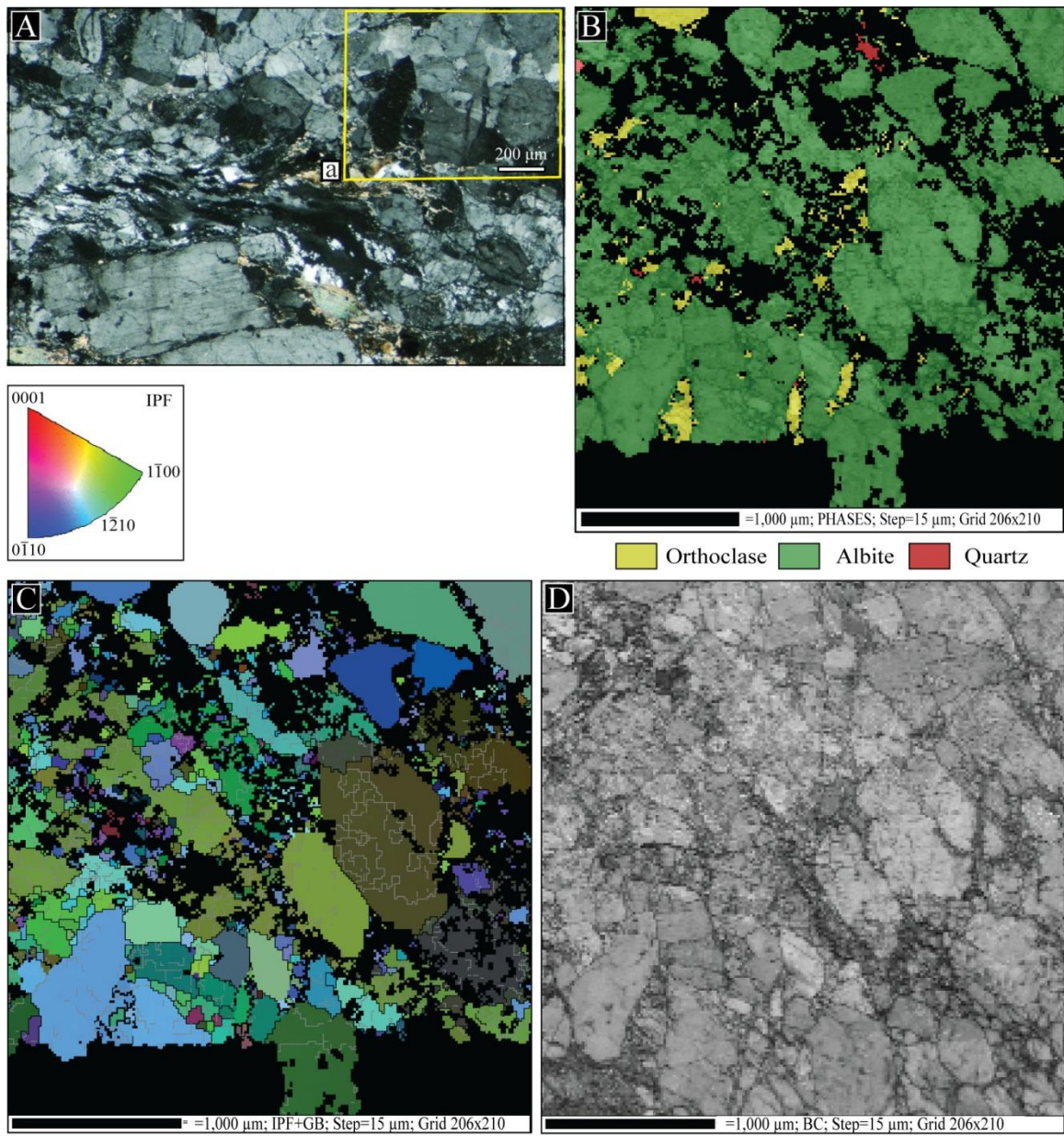


**Figure C.10** Location of EBSD beam map and EBSD results for sample SM-07-08-02, study region A.

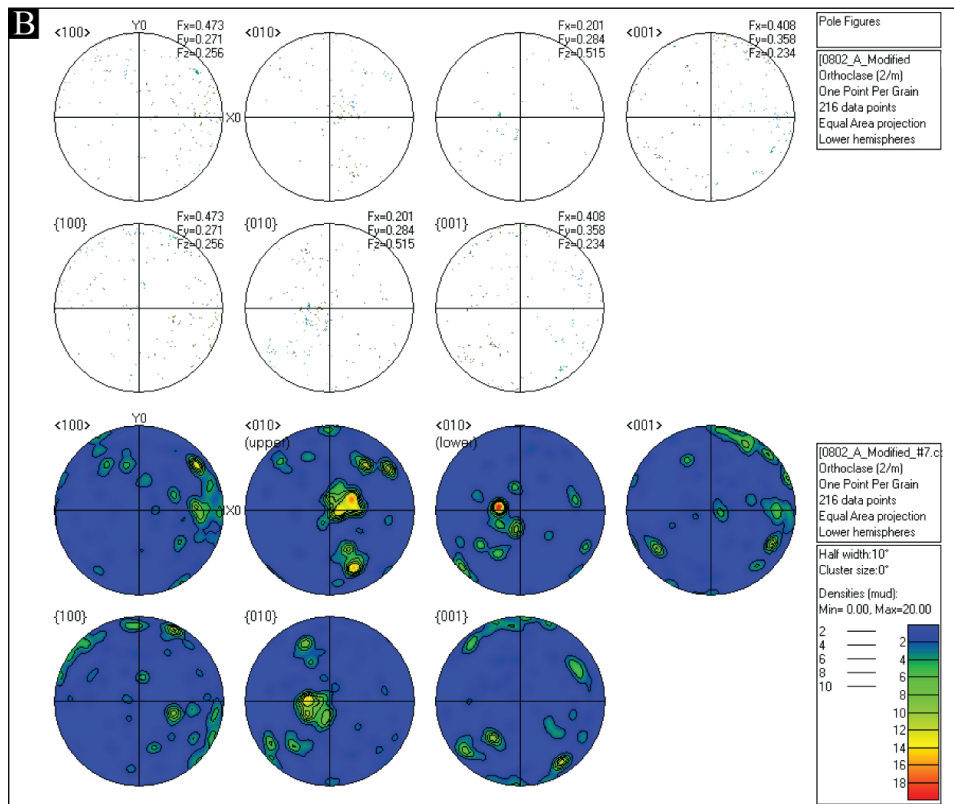
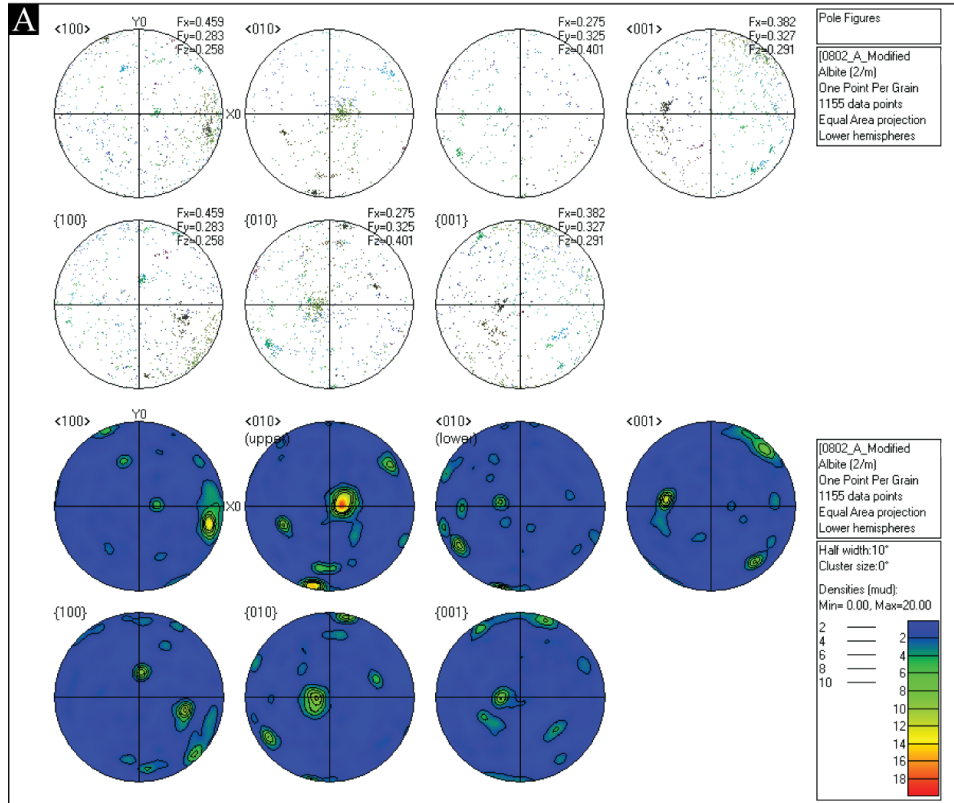


**Figure C.11** Feldspar pole figures for sample SM-07-08-02, study region A. Pole figures are constructed such that the macroscopic foliation is parallel to X0 and the stretching lineation is contained within the foliation and intersects the primitive circle. **A.** Albite pole figures. **B.** Orthoclase pole figures.

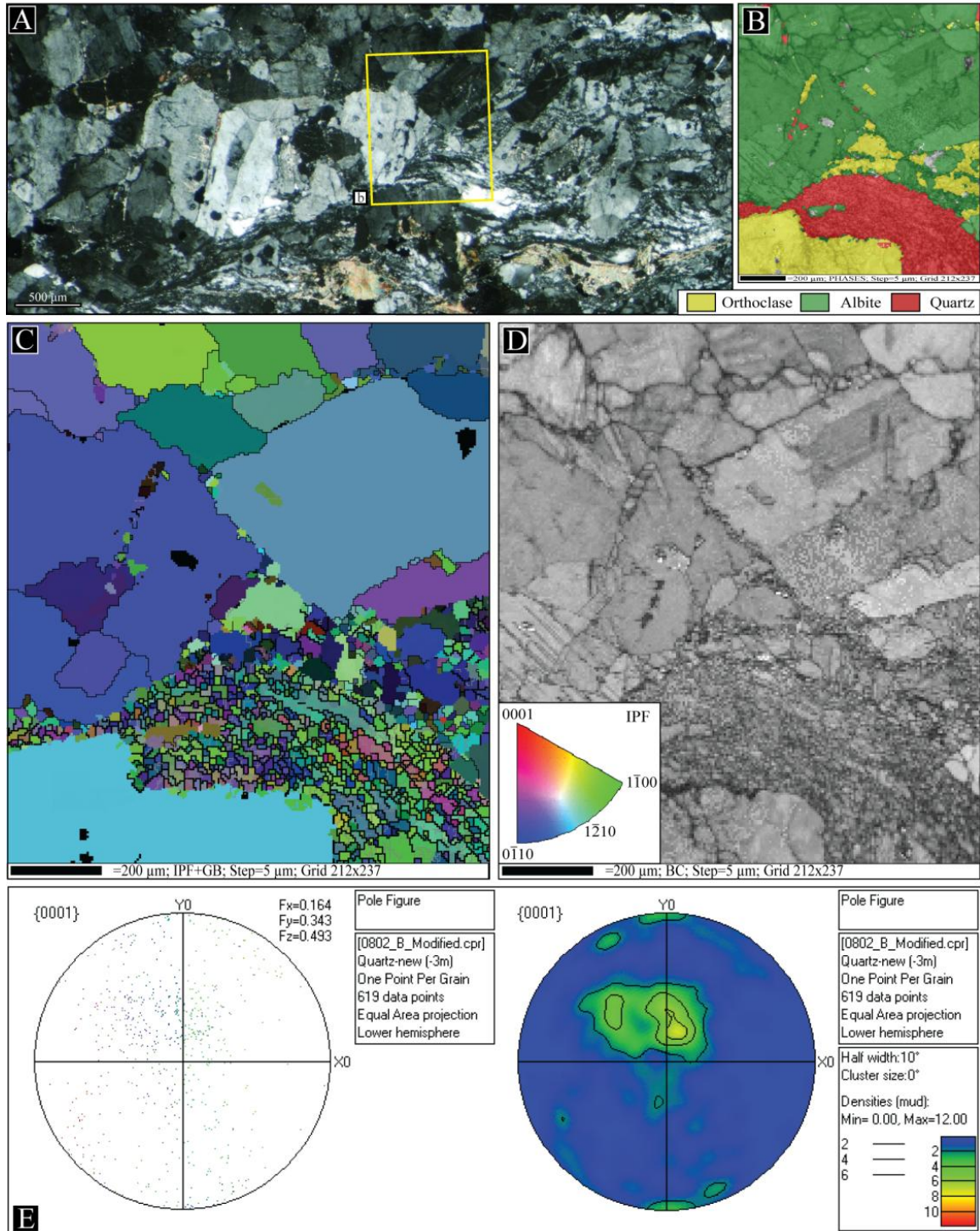


**Figure C.12** Location of EBSD beam map and EBSD results for sample SM-07-08-02, study region B.

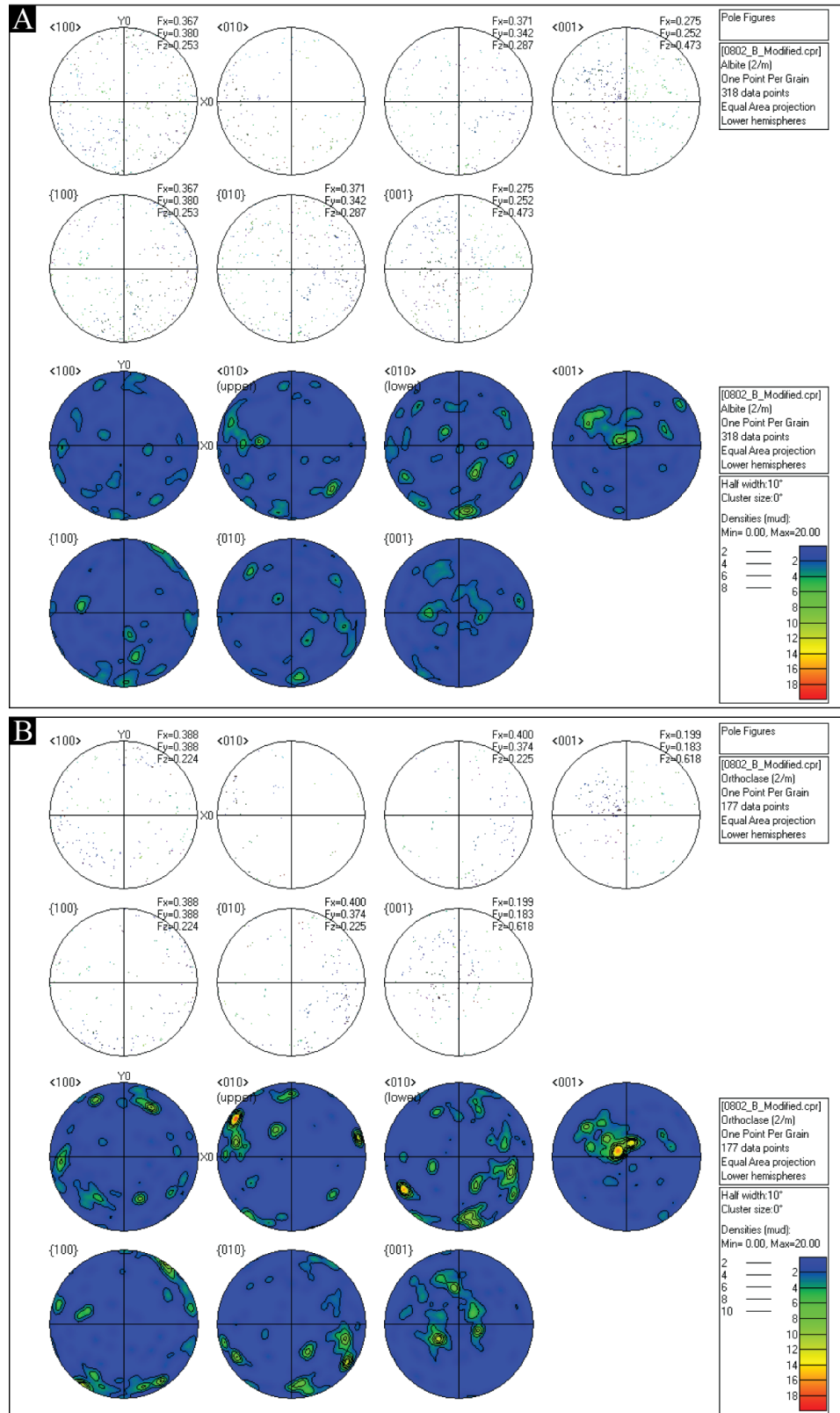


**Figure C.13** Feldspar pole figures for sample SM-07-08-02, study region B. Pole figures are constructed such that the macroscopic foliation is parallel to X0 and the stretching lineation is contained within the foliation and intersects the primitive circle. **A.** Albite pole figures. **B.** Orthoclase pole figures.

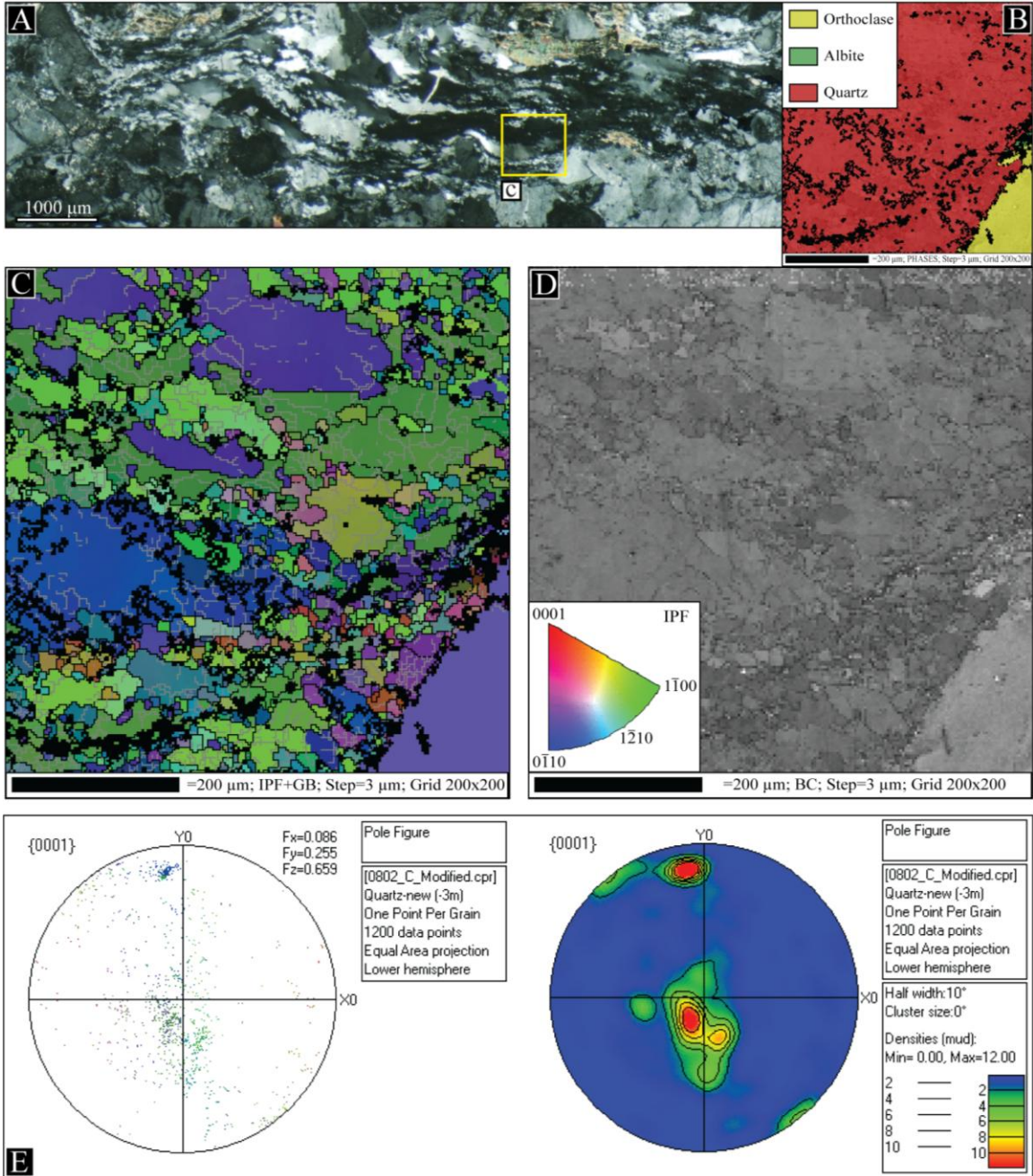


**Figure C.14** Location of EBSD beam map and EBSD results for sample SM-07-08-02, study region C.

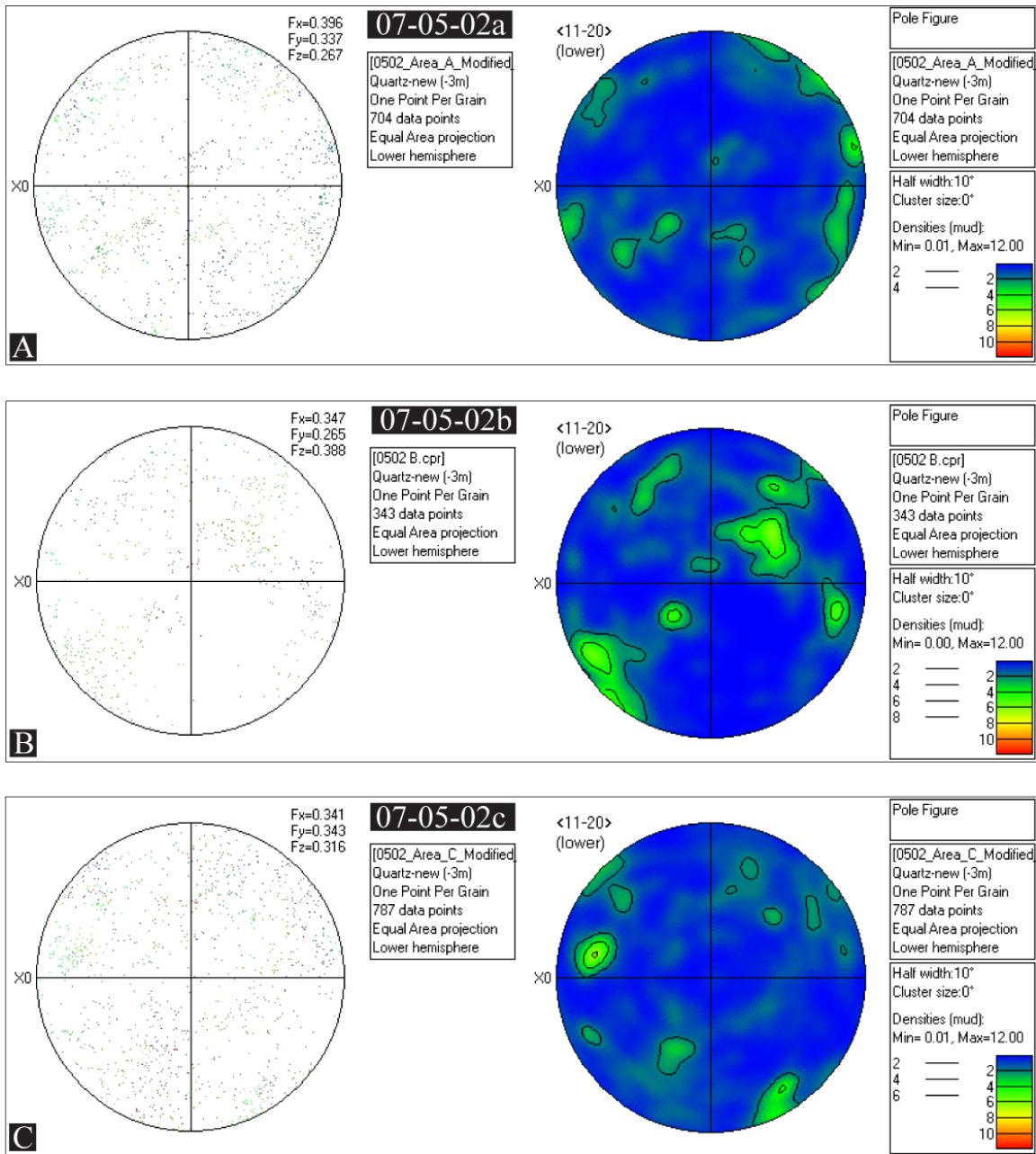


**Figure C.15** Quartz *a*-axis pole figures for sample SM-7-05-02. Pole figures are lower hemisphere equal area plots where the macroscopic foliation is parallel to the X direction and the stretching lineation is contained within the foliation and intersects the primitive circle. The X0 direction and the Y0 direction represent the finite strain axes of lengthening (X) and shortening (Z), respectively. **A.** Study region A. **B.** Study region B. **C.** Study region C.

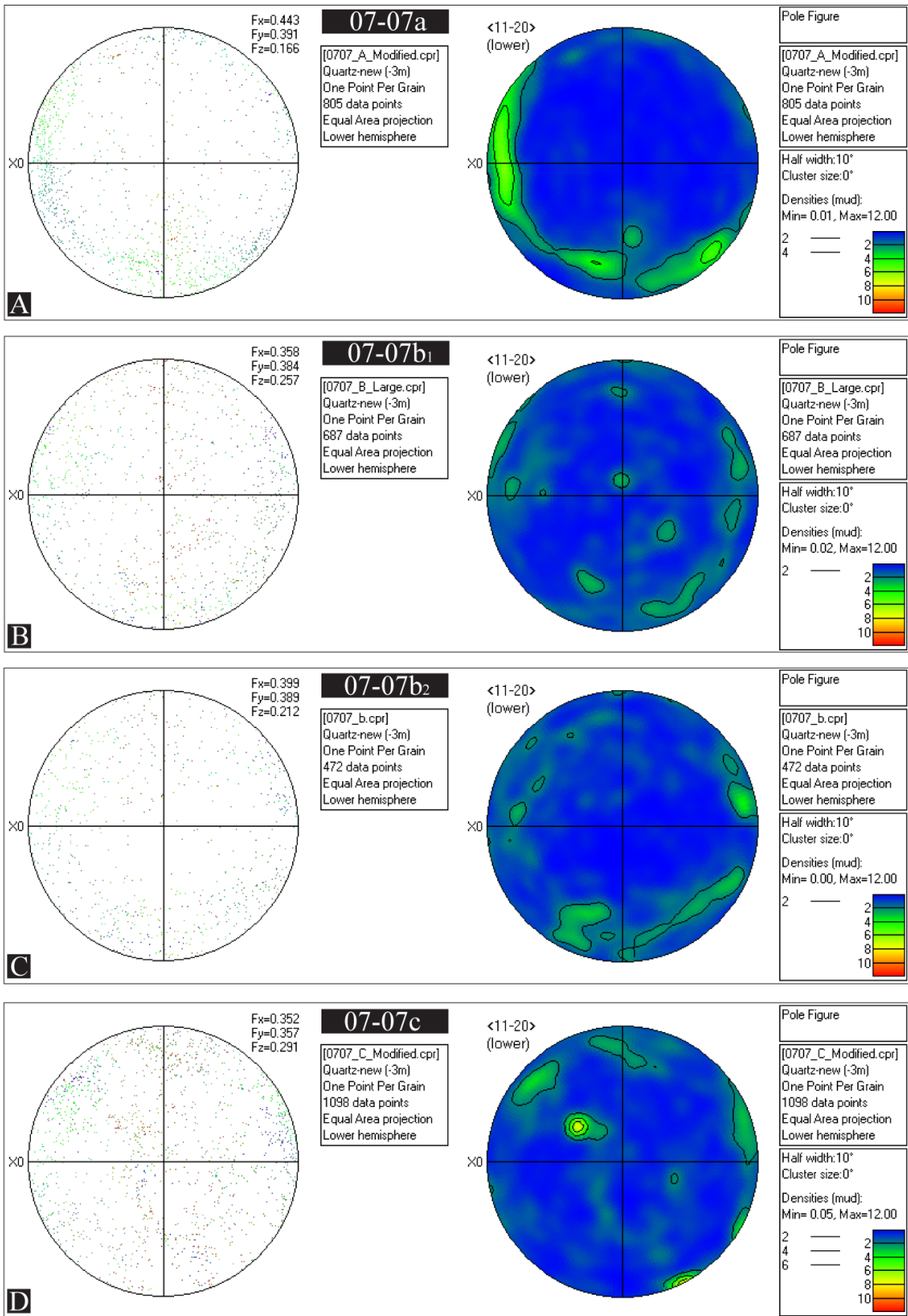


**Figure C.16** Quartz *a*-axis pole figures for sample SM-07-07. Pole figures are lower hemisphere equal area plots where the macroscopic foliation is parallel to the X direction and the stretching lineation is contained within the foliation and intersects the primitive circle. The X0 direction and the Y0 direction represent the finite strain axes of lengthening (X) and shortening (Z), respectively. **A.** Study region A. **B.** Study region B<sub>1</sub>. **C.** Study region B<sub>2</sub>. **D.** Study region C.

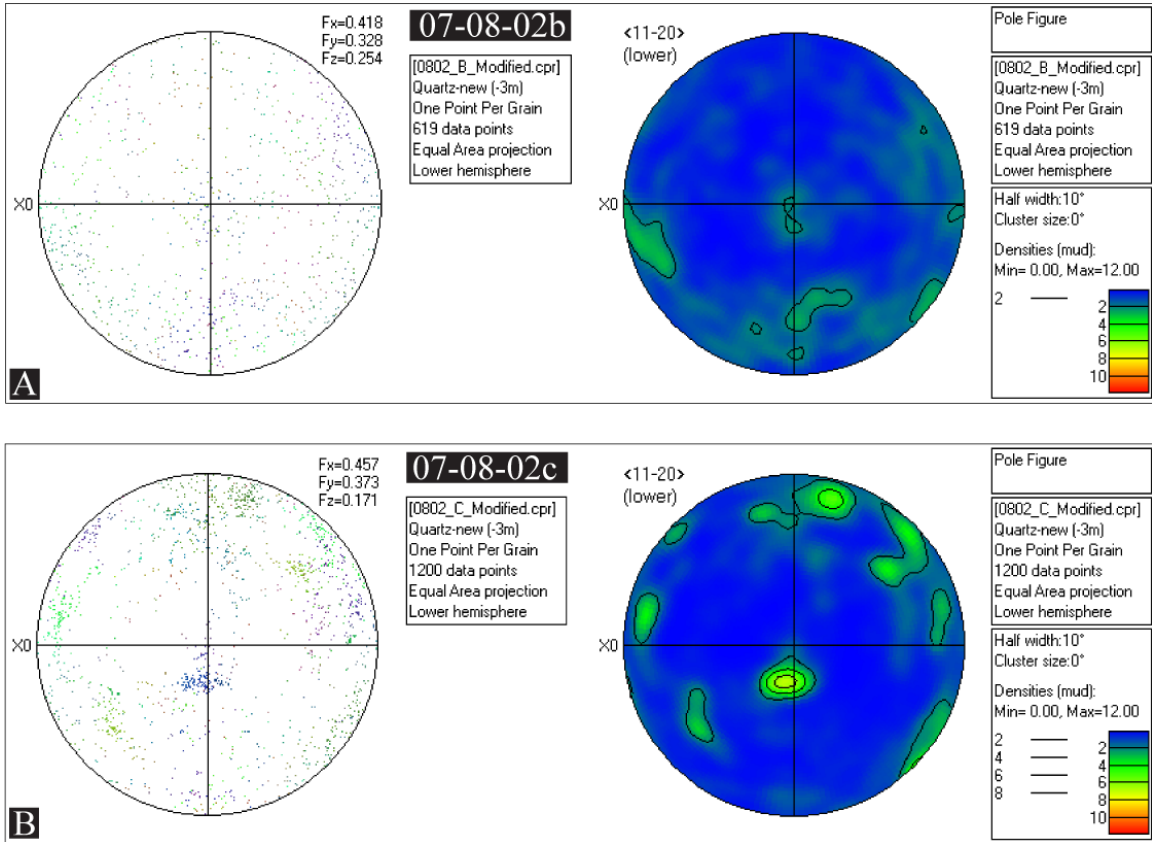


**Figure C.17** Quartz *a*-axis pole figures for sample SM-07-08-02. Pole figures are lower hemisphere equal area plots where the macroscopic foliation is parallel to the X direction and the stretching lineation is contained within the foliation and intersects the primitive circle. The X0 direction and the Y0 direction represent the finite strain axes of lengthening (X) and shortening (Z), respectively. **A.** Study region B. **B.** Study region C.

## APPENDIX D : EDS CHEMISTRY FIGURES

EDS figures include subfigures that correspond to the following elements: silica (Si), aluminum (Al), potassium (K), sodium (Na), and calcium (Ca). Areas with high and low chemical concentrations correspond to the darkest and lightest colors, respectively.

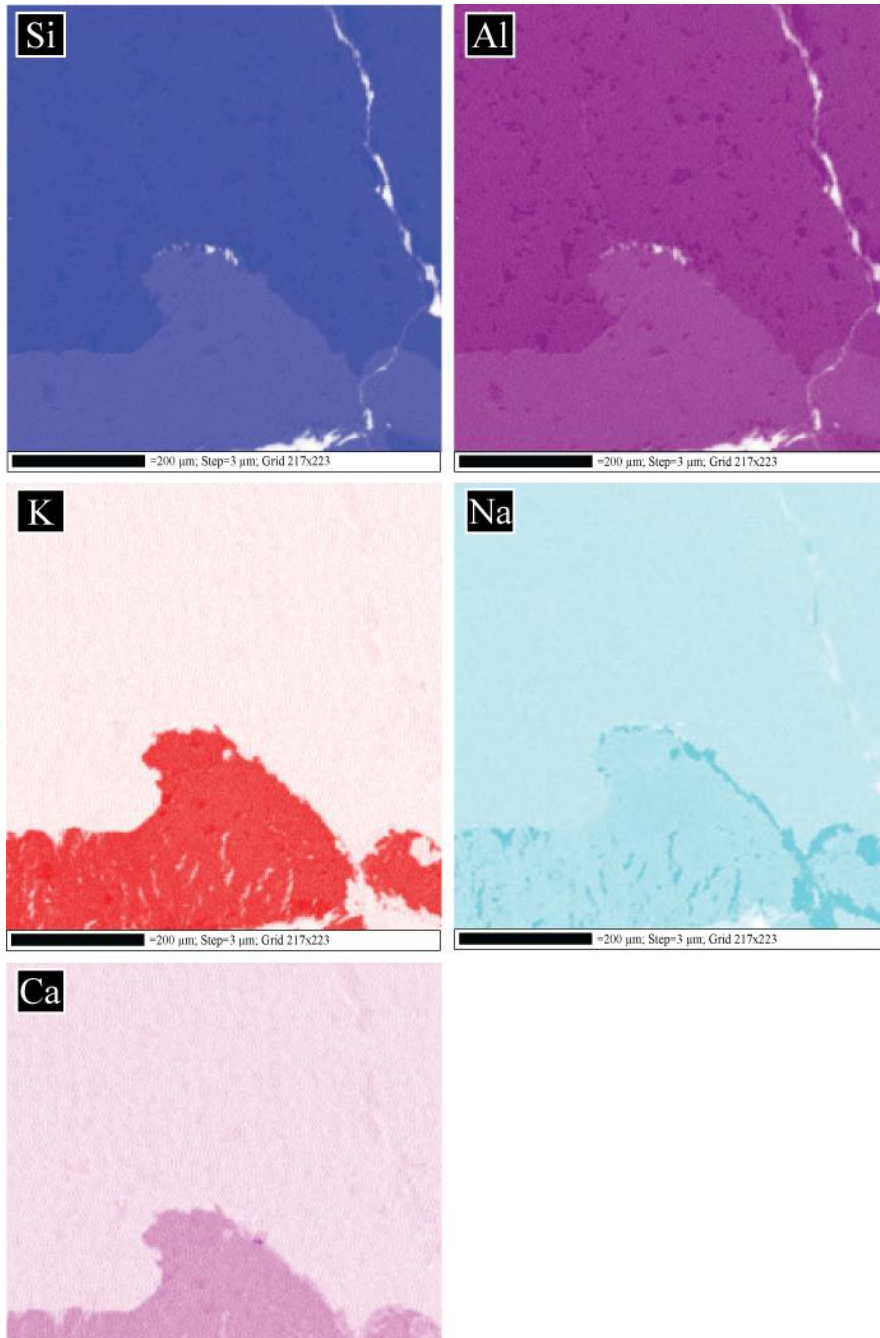


**Figure D.1** EDS data for sample SM-07-05-02, study region A.



**Figure D.2** EDS data for sample SM-07-05-02, study region B.

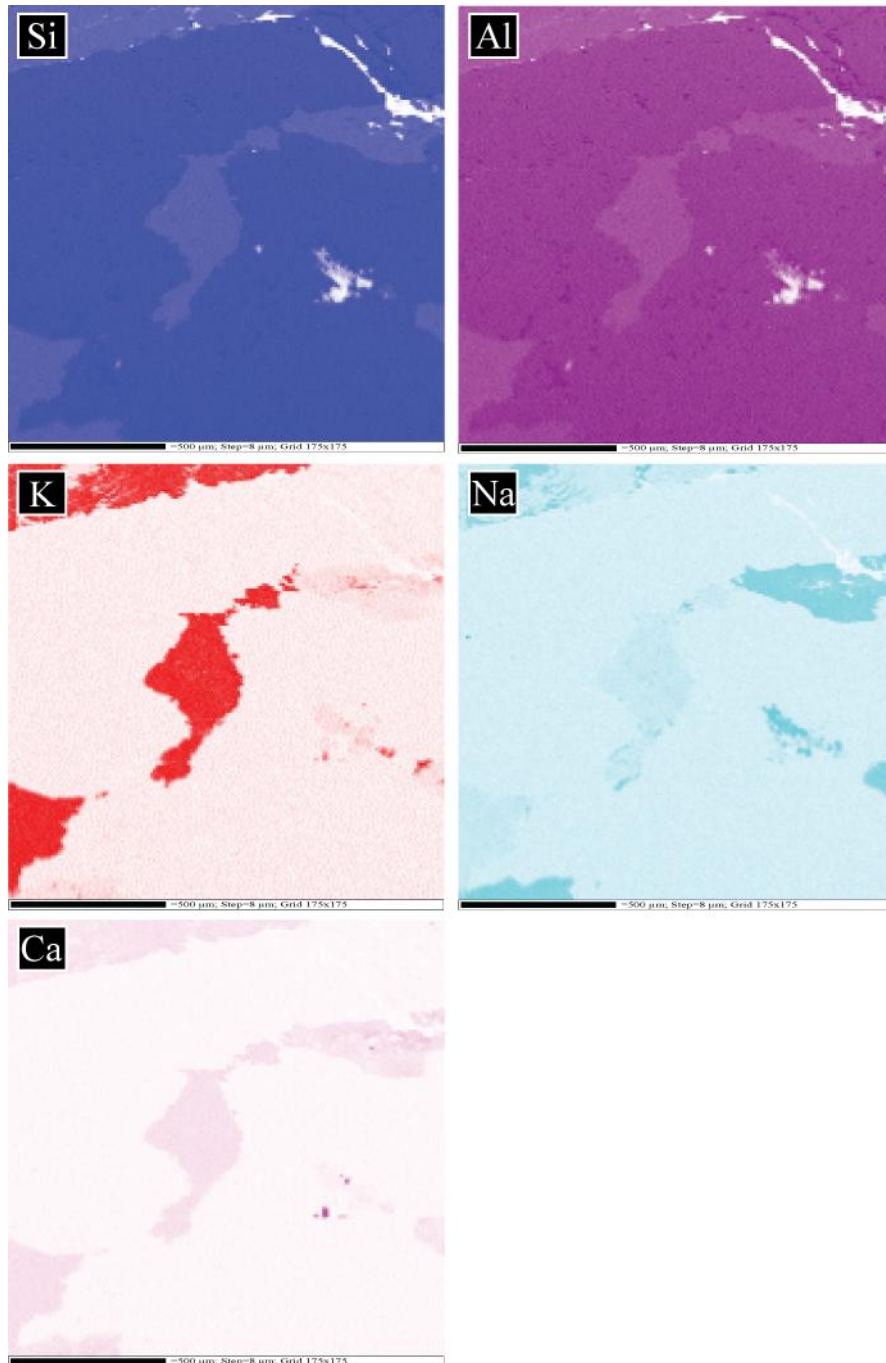


**Figure D.3** EDS data for sample SM-07-05-02, study region C.

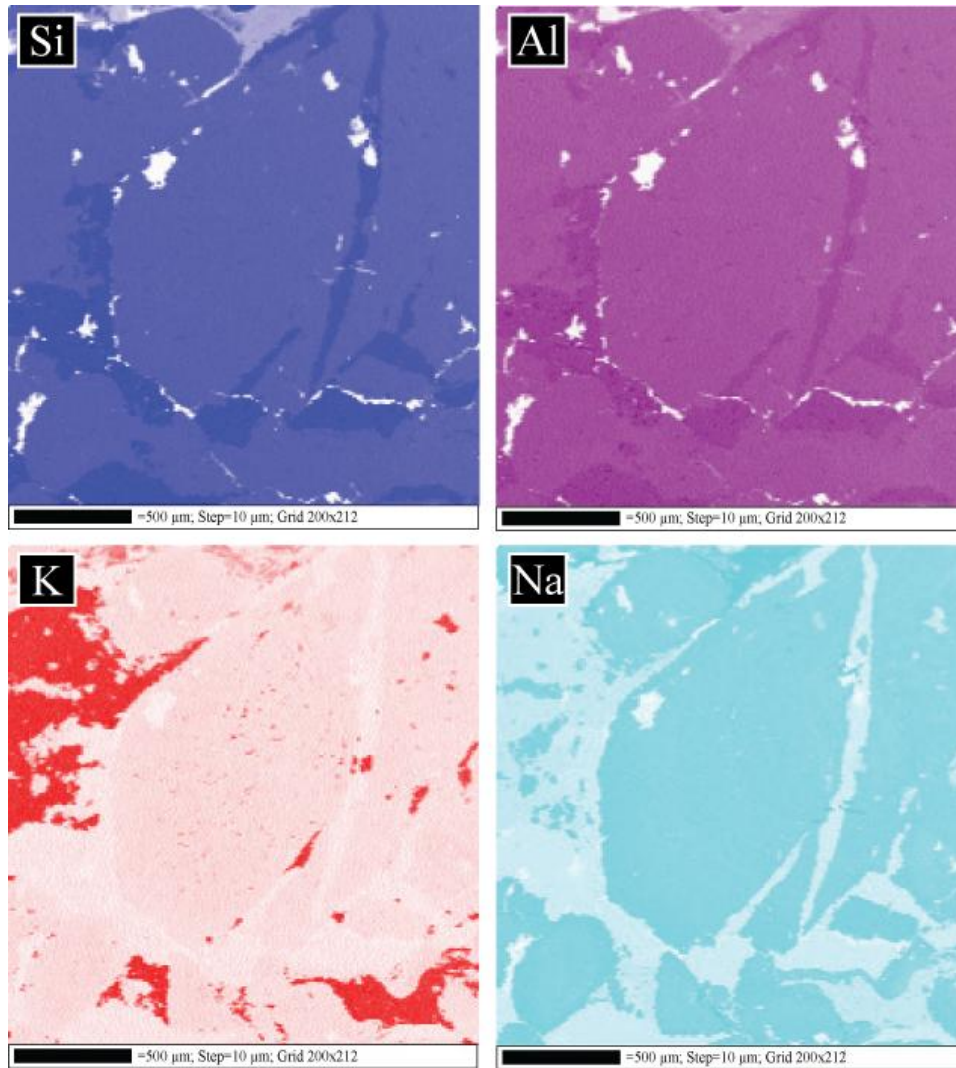


**Figure D.4** EDS data for sample SM-07-07, study region B<sub>1</sub>.

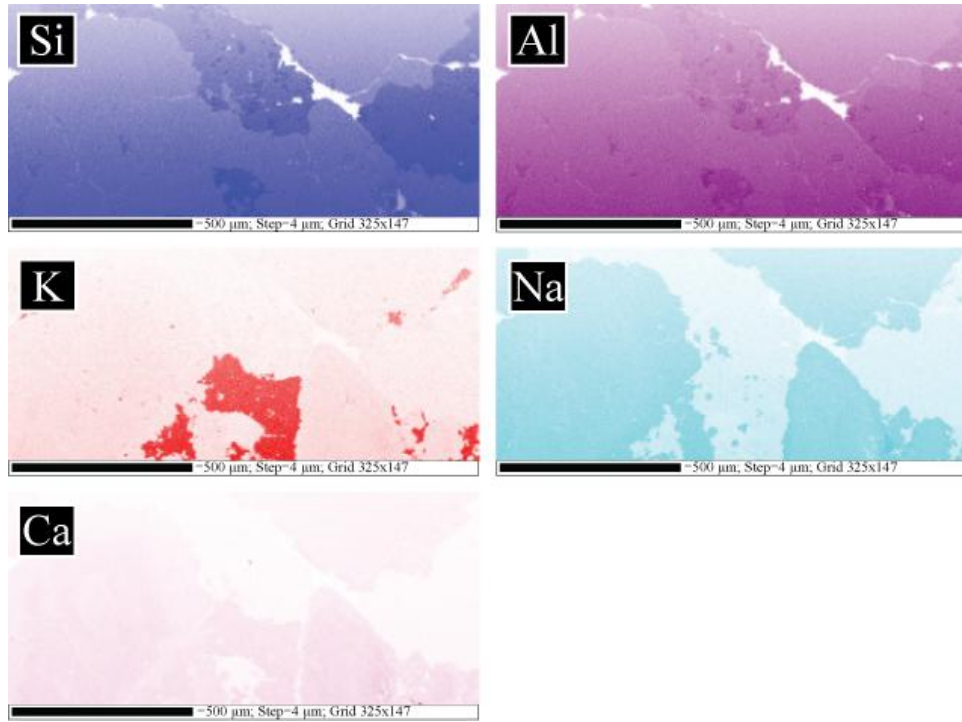


**Figure D.5** EDS data for sample SM-07-07, study region B<sub>2</sub>.

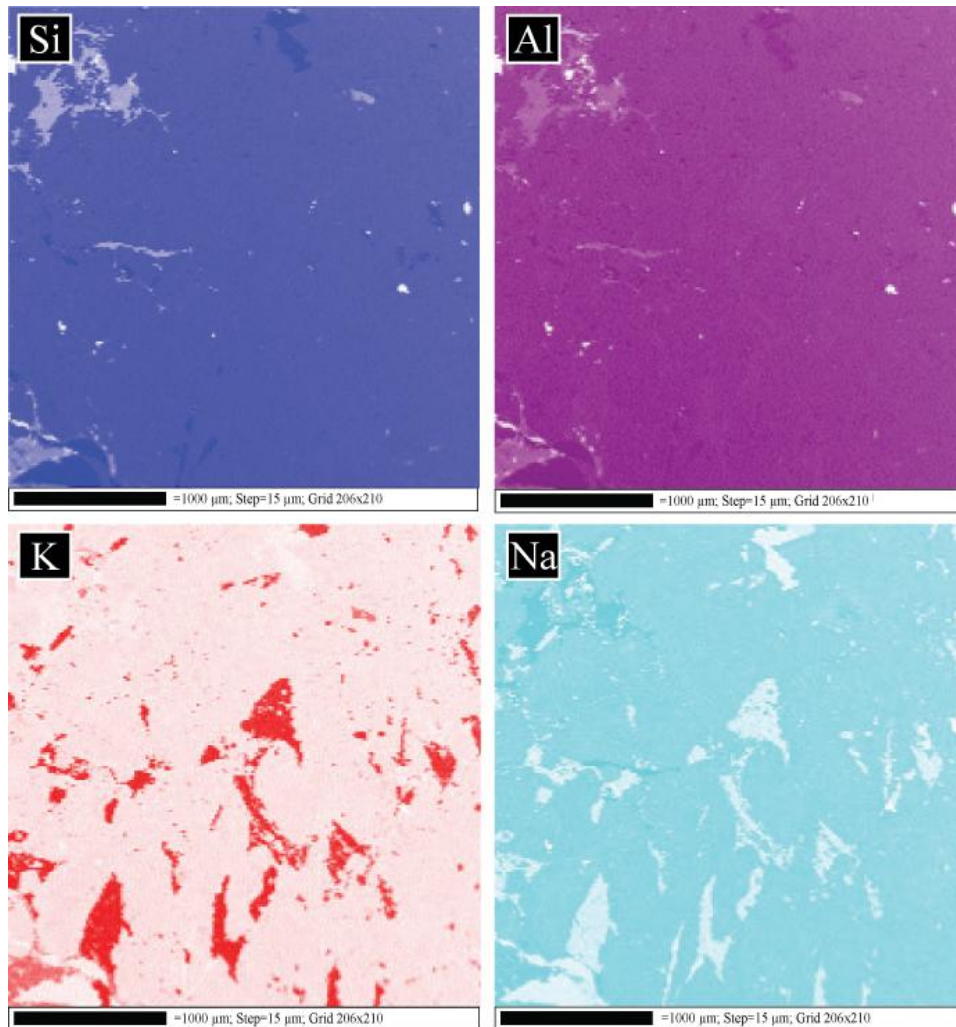


**Figure D.6** EDS data for sample SM-07-08-02, study region A.



**Figure D.7** EDS data for sample SM-07-08-02, study region B.

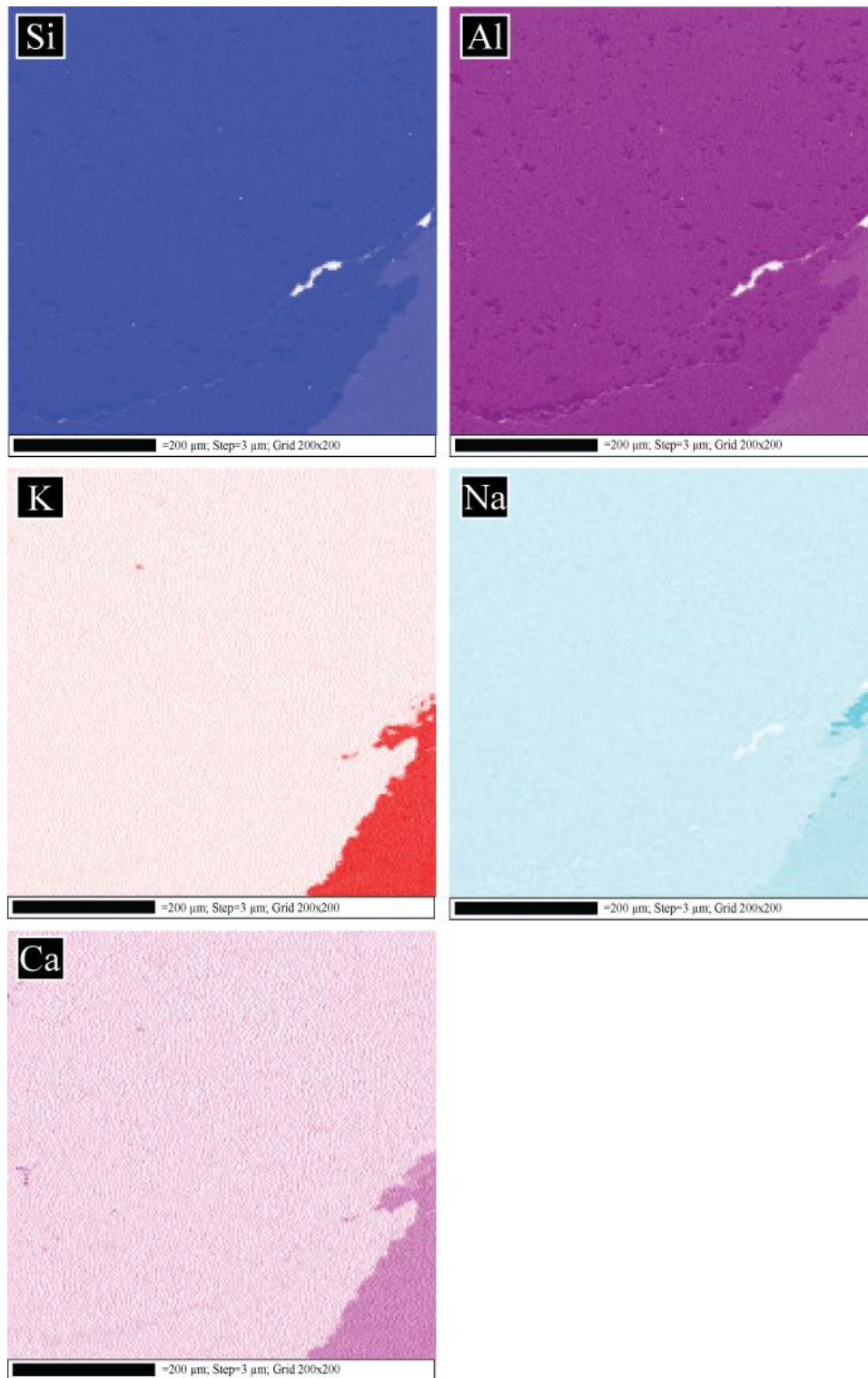


**Figure D.8** EDS data for sample SM-07-08-02, study region C.